Investigations on the Roles of Surface States on $BiVO_4$ Photoanodes and $CuBi_2O_4$ Photocathodes for Photoelectrochemical Water Splitting

by

Emre Usman

A Dissertation Submitted to the
Graduate School of Sciences and Engineering
in Partial Fulfillment of the Requirements for
the Degree of

Master of Science

in

Materials Science and Engineering

KOÇ
ÜNİVERSİTESİ

July 20, 2022

Investigations on the Roles of Surface States on $BiVO_4$ Photoanodes and $CuBi_2O_4$ Photocathodes for Photoelectrochemical Water Splitting

Koç University

Graduate School of Sciences and Engineering

This is to certify that I have examined this copy of a master's thesis by

Emre Usman

and have found that it is complete and satisfactory in all respects,
and that any and all revisions required by the final
examining committee have been made.

Committee Members:

_____

Assoc. Prof. Sarp Kaya (Advisor)

_____

Prof. Alphan Sennaroğlu

_____

Assoc. Prof. Ferdi Karadaş

Date: July 20, 2022

Dedicated to Müjde, Murat, and Zeynep

ABSTRACT

Investigations of the Roles of Surface States on $BiVO_4$ Photoanodes and $CuBi_2O_4$ Photocathodes for Photoelectrochemical Water Splitting

Emre Usman

Master of Science in Materials Science and Engineering

July, 2022

Climate change is an alarming issue, which has a devastating impact on our planet. Especially CO_2 gas emissions due to the wide-spread utilization of fossil fuels play a major role in global warming. To remove fossil fuels from our lives, alternative energy sources are needed to satisfy the ever-increasing energy demand. Hydrogen is a one of the most promising green energy carriers due to its zero-carbon emission upon utilization, and its extremely high gravimetric energy density.

Photoelectrochemical water splitting is a promising route to obtain green hydrogen directly from water and sunlight. Oxide semiconductors utilized as photoelectrodes offer significant potential in terms of light absorption and stability in aqueous electrolytes however their poor surface activities and ineffective charge carrier utilization properties hamper their widespread use. Understanding the origin of these poor activities is crucial to de-bottleneck the performance of photoelectrodes.

$BiVO_4$ photoanodes, one of the most promising materials for water oxidation reaction, suffer from overwhelming surface recombination of charge carriers which limit their activity. However, the recombination dynamics are complex and the detailed mechanisms of the recombination taking place in the bulk and the surface regions are typically not addressed. In the first part of this study, $BiVO_4$ photoanodes with high surface area were synthesized using electrodeposition method. We show that the water oxidation activity of $BiVO_4$ photoanode is significantly boosted by the TiO_2 overlayer prepared by atomic layer deposition (ALD). With a TiO_2 overlayer of an optimized thickness, the photocurrent at 1.23 V_{RHE} increased from 0.64 to 1.1 $mA.cm^{-2}$ under front illumination, corresponding to 72% enhancement. We attribute this substantial improvement to enhanced charge separation and suppression of surface recombination due to surface state passivation. We provide direct evidence via

transient photocurrent (TPC) measurements that TiO_2 overlayer significantly decreases the photogenerated electron-trapping process at the $BiVO_4$ surface. Electron-trapping passivation leads to enhanced electron photoconductivity, which results in higher photocurrent enhancement under front illumination, rather than back illumination. Even though the electron trapping process is eliminated completely at higher TiO_2 overlayer thicknesses, the charge transfer resistance at the surface also increases significantly, resulting in a diminished photocurrent. We demonstrate that ultrathin TiO_2 overlayer can be used to fine-tune the surface properties of $BiVO_4$.

$CuBi_2O_4$ is one of the most promising photocathodes for HER due to its low band gap and high flat-band potential. However, compared to $BiVO_4$, it is a lot less studied, so the roles of the charge carrier dynamics are not yet fully understood. In the second part of this study, we synthesized $CuBi_2O_4$ photocathodes via electrodeposition method. The synthesized photocathode films were characterized by XPS, XRD, FESEM, UV-vis-NIR absorption, and Raman spectroscopy. Using electrochemical impedance spectroscopy (EIS) and TPC measurements, we have identified the presence of surface-states, and photogenerated electron trapping process at these states. The results indicate that surface-states near the flat-band potential act as photogenerated electron traps, which results in a delay in the photocurrent onset to 0.9 V_{RHE} -1.0 V_{RHE} even though photocurrent is observed as early as 1.4 V_{RHE}. The TiO_2 overlayer was grown on $CuBi_2O_4$ surface via ALD with different thicknesses to tune the charge carrier dynamics at the surface and inhibit the electron trapping process. However, even with low coverage of TiO_2 overlayer, $CuBi_2O_4$ activity significantly decreased. Furthermore, we have identified significant photocorrosion, which is detrimental for the stability of the photocathode. These results suggest that interfacial dynamics are important for the $CuBi_2O_4$ photocathode activity and stability. Thus, the surface charge carrier dynamics need to be tuned by other materials than TiO_2 to passivate the electron trapping process to improve the performance of $CuBi_2O_4$.

ÖZETÇE

Fotoelektrokimyasal Su Ayrımı için $BiVO_4$ Fotoanot ve $CuBi_2O_4$ Fotokatotları Üzerinde Yüzey Durumlarının Rollerinin İncelenmesi

Emre Usman

Malzeme Bilimi ve Mühendisliği, Yüksek Lisans

Temmuz 2022

İklim değişikliği, gezegenimiz üzerinde yıkıcı bir etkisi olan endişe verici bir konudur. Özellikle fosil yakıtların kullanımının yaygınlaşmasından kaynaklanan CO_2 gazı emisyonları küresel ısınmada büyük rol oynamaktadır. Fosil yakıtları hayatımızdan çıkarmak için sürekli artan enerji talebini karşılamak için alternatif enerji kaynaklarına ihtiyaç vardır. Hidrojen, kullanım üzerine sıfır karbon emisyonu ve son derece yüksek gravimetrik enerji yoğunluğu nedeniyle en umut verici yeşil enerji taşıyıcılarından biridir.

Fotoelektrokimyasal su ayırma, doğrudan su ve güneş ışığından yeşil hidrojen elde etmek için umut verici bir yoldur. Fotoelektrot olarak kullanılan oksit yarı iletkenleri, sulu elektrolitlerde ışık absorpsiyonu ve stabilitesi açısından önemli bir potansiyel sunar, ancak zayıf yüzey aktiviteleri ve etkisiz yük taşıyıcı kullanım özellikleri, yaygın kullanımlarını engellemektedir. Bu zayıf faaliyetlerin kökenini anlamak, fotoelektrotların performansındaki darboğazı ortadan kaldırmak için çok önemlidir.

Su oksidasyon reaksiyonu için en umut verici malzemelerden biri olan $BiVO_4$ fotoanotları, aktivitelerini sınırlayan yük taşıyıcıların yoğun yüzey rekombinasyonundan muzdariptir. Bununla birlikte, rekombinasyon dinamikleri karmaşıktır ve yığın ve yüzey bölgelerinde meydana gelen rekombinasyonun ayrıntılı mekanizmaları tipik olarak ele alınmaz. Bu çalışmanın ilk bölümünde, elektrokimyasal depozisyon yöntemi kullanılarak yüksek yüzey alanına sahip $BiVO_4$ fotoanotları sentezlenmiştir. $BiVO_4$ fotoanotunun su oksidasyon aktivitesinin, atomik katman biriktirme (ALD) ile hazırlanan TiO_2 üst katmanı tarafından önemli ölçüde artırıldığını gösterdik. Optimize edilmiş bir kalınlığa sahip bir TiO_2 üst katmanı ile 1,23 VR_{HE}'deki fotoakım, ön aydınlatma altında 0,64'ten 1,1 $mA.cm^{-2}$'ye yükselerek %72'lik bir iyileştirmeye karşılık gelir. Bu önemli gelişmeyi, gelişmiş yük

ayrımına ve yüzey durumu pasivasyonu nedeniyle yüzey rekombinasyonunun bastırılmasına bağlıyoruz. TiO_2 üst katmanının $BiVO_4$ yüzeyinde fotojenere elektron yakalama sürecini önemli ölçüde azalttığına dair geçici fotoakım (GFA) ölçümleri yoluyla doğrudan kanıt sağlıyoruz. Elektron yakalama pasifleştirme, arka aydınlatmadan ziyade ön aydınlatma altında daha yüksek fotoakım geliştirme ile sonuçlanan gelişmiş elektron fotoiletkenliğine yol açar. Elektron yakalama işlemi, daha yüksek TiO_2 üst katman kalınlıklarında tamamen ortadan kaldırılsa da, yüzeydeki yük transfer direnci de önemli ölçüde artar, bu da foto akımın azalmasına neden olur. Ultra ince TiO_2 üst tabakasının $BiVO_4$'ün yüzey özelliklerine ince ayar yapabiliyor olduğunu gösteriyoruz.

$CuBi_2O_4$, düşük bant aralığı ve yüksek düz bant potansiyeli nedeniyle suyun indirgenme reaksiyonu için en umut verici fotokatotlardan biridir. Bununla birlikte, $BiVO_4$ ile karşılaştırıldığında, çok daha az çalışılmıştır, bu nedenle yük taşıyıcı dinamiklerinin rolleri henüz tam olarak anlaşılmamıştır. Bu çalışmanın ikinci bölümünde, elektrokimyasal depozisyon yöntemi ile $CuBi_2O_4$ fotokatotları sentezledik. Sentezlenen fotokatot filmler XPS, XRD, FESEM, UV-NIR absorpsiyonu ve Raman spektroskopisi ile karakterize edildi. Elektrokimyasal empedans spektroskopisi (EIS) ve TPC ölçümlerini kullanarak, yüzey durumlarının varlığını ve bu durumlarda fotojenere elektron yakalama sürecini belirledik. Sonuçlar, düz bant potansiyeline yakın yüzey durumlarının, fotoakım 1,4 V_{RHE} kadar erken gözlemlenmesine rağmen, fotoakım başlangıcında 0,9 V_{RHE} -1,0 V_{RHE}'ye gecikmeyle sonuçlanan, fotojenere elektron tuzakları gibi davrandığını göstermektedir. TiO_2 üst tabakası, yüzeydeki yük taşıyıcı dinamiklerini ayarlamak ve elektron yakalama sürecini engellemek için farklı kalınlıklarda ALD aracılığıyla $CuBi_2O_4$ yüzeyinde büyütüldü. Bununla birlikte, düşük TiO_2 üst tabakası kaplaması ile bile, $CuBi_2O_4$ aktivitesi önemli ölçüde azaldı. Ayrıca, fotokatodun stabilitesi için zararlı olan önemli fotokorozyon tespit ettik. Bu sonuçlar, arayüzey dinamiklerinin $CuBi_2O_4$ foto katot aktivitesi ve stabilitesi için önemli olduğunu göstermektedir. Bu nedenle, $CuBi_2O_4$'ün performansını iyileştirmek için elektron yakalama sürecini pasifleştirmek için yüzey yükü taşıyıcı dinamiklerinin ayarlanması gerekir.

Acknowledgements

After spending 4.5 years in this lab, it feels strange to having to say goodbye. There are so many memories, so many things to be thankful for throughout my journey. I really enjoyed the time that I've spent here, and I will remember these years cheerfully.

Firstly, I would like to thank my advisor, Dr. Sarp Kaya. I started to work with him when I was 20 years old, as an undergrad. Since then, he truly influenced me with his deep enthusiasm and excitement for research, from start to finish. I am grateful for his guidance during my studies. He always had time to answer my questions but for also leaving me space to pursue my own questions. He treated me as a colleague rather than a boss, which made it really easy to find motivation even in the times where the project didn't seem to be going too well. It was a privilege to have him as my advisor.

I would like to thank my committee members Dr. Alphan Sennaroglu and Dr. Ferdi Karadas, for their valuable feedback and interesting questions.

I would also like to acknowledge Koc University for providing financial support throughout my Master's studies.

I would like to thank Dr. Mahsa Barzgarvishlaghi and Dr. Abdullah Kahraman, for teaching me various aspects of photoelectrochemistry. I've learnt a great deal from them in both experimental, and theoretical aspects. I am grateful for the good times that we spent in and outside of the lab with Amin Mohammadpour and Oyku Alagoz. The tennis games that we had with Amin were truly joyful (and competitive!). Having Ozce Durak, a long-time friend in the same office was truly a bliss. I would like to thank Dr. Navid Solati and Dr. Timucin Balkan for the enlightening discussions about electrochemistry. Sharing the lab with them was truly amazing, as they can make one burst in tears from laughter all of a sudden.

I would also like to thank my family, Mujde, Murat, and Zeynep, whom I dedicated this work to. They encouraged me to do whatever I was passionate about and supported me all the way, with endless love and compassion. Lastly, I would like to thank the latest member of our family, Erik. Even though he has a rather unpleasant breath odor, spending just a few moments with him could make my day.

TABLE OF CONTENTS

List of Figures

Chapter 1. Introduction

1.1.Solar Light as a Sustainable Energy Source

Climate change and global warming is an alarming issue, which has a devastating impact on our planet. Especially CO_2 gas emissions as a result of industrial processes and fossil fuel utilization play a major role in global warming. Thus, its emission must be limited[10]. In order to remove fossil fuels from our lives, alternative energy sources are needed to satisfy the ever-increasing energy demand. Hydrogen is a one of the most promising green energy carriers due to its zero-carbon emission upon utilization, and its extremely high gravimetric energy density[11]. However, currently more than 90% of the hydrogen production is done via steam reforming, coal gasification, and methane partial oxidation, which all are fossil fuel based processes[12]. In order to reduce the CO_2 emissions and utilize hydrogen energy in a sustainable manner, alternative ways of producing hydrogen without using fossil fuels must be entertained.

Solar energy utilization is an attractive solution to the CO_2 emission problem since it is a sustainable and abundant energy resource. The solar energy can be converted to a form of energy that the society can utilize, such as electricity or hydrogen gas, in a sustainable manner. The devices that convert solar light into electricity are called solar cells. However, the produced electricity from a solar cell needs to be utilized directly, or converted to another form of energy that can be stored[13]. In another approach, the solar light can be directly converted to a chemical feedstock that can be used as an energy carrier, such as hydrogen[14].

Solar-to-hydrogen conversion utilizes sunlight and water as feedstock, making it fossil fuel free and sustainable. Another important fact is that only abundant feedstocks are needed for the overall process. It is also referred as solar water splitting. There are different device configurations to achieve such conversion, which are photocatalytic water splitting, photovoltaic-electrochemical water splitting, solar thermochemical water splitting, photobiological hydrogen production, and photoelectrochemical water splitting[15–17]. This work focuses on the latter approach.

1.2.Photoelectrochemical (PEC) Water Splitting

Photoelectrochemical water splitting is an approach to drive the electrochemical reaction of water splitting, using both electrical energy and solar energy. It is demonstrated for the first time in 1972 by Fujishima and Honda, using TiO_2 photoanodes[18]. The water splitting half reactions are carried out at two electrode surfaces, in which the oxidation reaction is referred to as oxygen evolution reaction (OER), and the reduction reaction is referred to as hydrogen evolution reaction (HER).

$H_2O(l) + 4h^+ \rightarrow 4H^+(aq) + O_2(g)$ (OER, E°= 1.23 V_{RHE})

$4H^+(aq) + 4e^- \rightarrow 2H_2(g)$ (HER, E°= 0 V_{RHE})

$2H_2O(l) \rightarrow 2H_2(g) + O_2(g)$ (Overall, E°=1.23 V_{RHE})

A graphical representation of a PEC cell for water splitting is given in Figure 1.1 below. As the semiconductor materials have a band gap, upon excitation with incident light, they can generate electron-hole pairs. The photogenerated holes then migrate to the surface to react with water molecules and generate O_2 and H^+. The photogenerated electrons migrate to the back-contact and flow through the external connection to close the circuit. In the counter electrode, a p-type semiconductor is used to drive HER. Analogous to the photoanode, photogenerated electrons are migrated towards the surface to react with H^+ ions to generate H_2. The photogenerated holes are migrated towards the current collector to recombine with the electrons coming from the external wire in a tandem configuration[19].

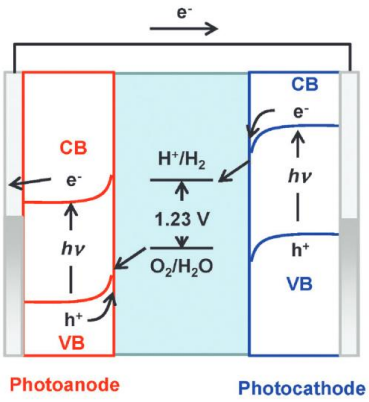

Figure 1.1. Schematic representation of PEC water splitting with photoanode and photocathode[1].

1.3.n-type and p-type Photoelectrode Properties for Water Splitting

For photoelectrochemical cells, semiconductor materials are used as photoelectrocatalysts as they can absorb incident light and generate electron-hole pairs. However, there are certain set of conditions for a semiconductor to be used in a PEC cell, which are summarized below:

Doping type: Photoelectrodes are doped semiconductors, which can be either n-type, or p-type. Depending on the type of doping either a depletion layer or an accumulation layer can be formed at the near surface region of the semiconductor, which is commonly referred to as the space-charge region, as shown in Figure 1.2. When the photoelectrode is immersed in the electrolyte, the Fermi level of the electrode and the electrochemical potential of the electrolyte equilibrate. Since the number of redox couple molecules in the electrolyte are much higher than the dopant or acceptor density in the electrode, only electrode Fermi level significantly shifts. For an n-type electrode, the Fermi level is close to the conduction band and at higher energy than $E(H_2O/O_2)$. Thus, upon equilibration, the electrons are donated from the near surface region to the electrolyte, and a depletion layer forms. This depletion layer or the space charge region results in a built-in potential which is used to separate the photogenerated charge carriers. Due to the nature of the band bending, positively charged holes migrate towards the surface, and can be utilized for water oxidation reaction. In a similar manner, a p-type semiconductor Fermi level is close to its valence band. Thus, upon equilibration, the electrons flow from the electrolyte to the semiconductor, and a p-type depletion (or accumulation) can form. The resulting band bending separates the electron hole pairs, where electrons migrate towards the surface to drive water reduction reaction[2].

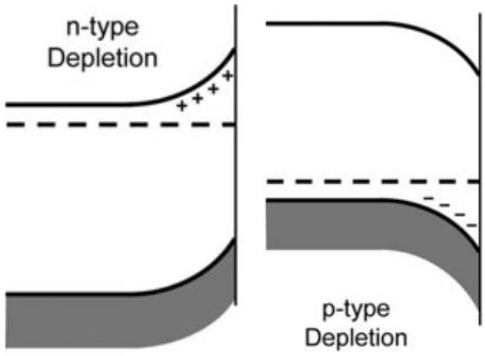

Figure 1.2. Simple schematic for n-type and p-type depletion and formation of band bending[2].

Band gap: Band gap of a semiconductor is referred to as a forbidden region where ideally no chemical states are present to accommodate charge carriers. Photons only at higher or equal energy to the band gap can be absorbed by the material, to generate electron-hole pairs. These charge carriers in turn can be used to drive the reaction of interest, HER or OER.

For semiconductors, the band gap can be either direct or indirect, which can be determined from the E-k diagram of the material. If the highest energy point in the valence band is located in the same k-vector with the lowest energy point in the conduction band, the electron excitation does not require a shift in momentum. Such behavior is called as direct band gap, as shown in Figure 1.3. If the valence band maximum and conduction band minimum are in a different k-vector, such transition is called indirect. The indirect transitions require an absorption or emission of a phonon, to account for the shift in momentum. Therefore the absorption coefficient for such materials are smaller with respect to direct band gap semiconductors[2].

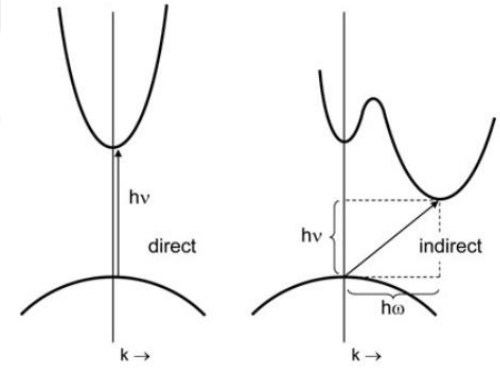

Figure 1.3. Representative E-k diagram for a direct and indirect band gap semiconductor[2].

Another important parameter is the energy of the band gap. Since the photons that are only at higher energy than the band gap can be absorbed and utilized, the band gap energy directly affects the total number of photons that can be absorbed, therefore gives an upper bound to the maximum photocurrent density that can be obtained from a photoelectrode. Theoretical relation between the maximum photocurrent density with the material band gap is demonstrated in Figure 1.4 below. The solar spectrum is mostly comprised of visible region of the electromagnetic spectrum[1], thus the theoretical current density shows a take-off in the UV-visible region.

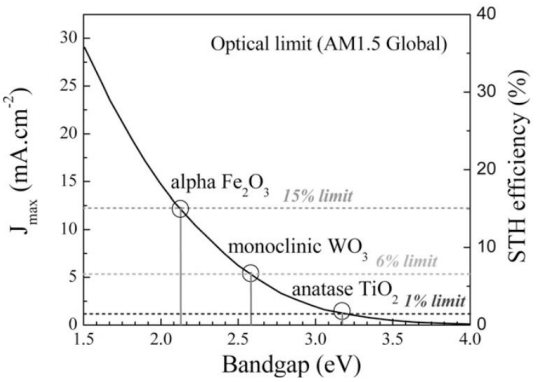

Figure 1.4. Theoretical maximum photocurrent and solar to hydrogen efficiency with respect to the material band gap, assuming 100% incident photon-to-current efficiency above band gap with AM 1.5 G solar spectra as incident light[3].

Band positions: The positions of the valence band maximum (VBM) and conduction band minimum (CBM) dictate the thermodynamical feasibility of a photoelectrode to drive certain chemical conversions. If the CBM is in the higher energy than the HER energy level (0 V_{RHE}), the photogenerated electrons can drive HER. Similarly, if the VBM is in lower energy than the OER energy level (1.23 V_{RHE}), the photogenerated holes can drive the OER[19]. Band edge values for various photoelectrodes are shown in Figure 1.5 below.

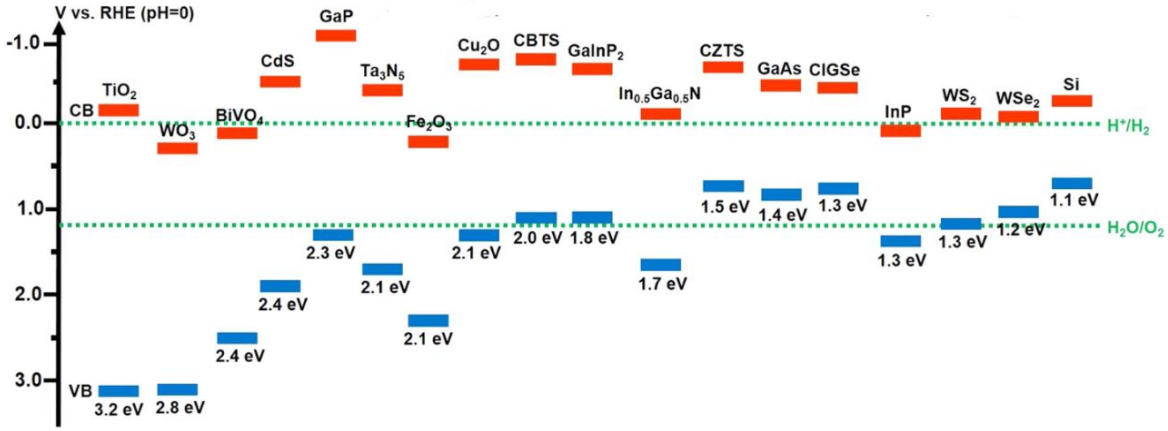

Figure 1.5. Band edge positions and band gaps of various semiconductors used for water splitting reactions[4].

1.4.$BiVO_4$-based Photoanodes for Oxygen Evolution Reaction

1.4.1. Why $BiVO_4$?

Among different photoanode candidates for OER, $BiVO_4$, an n-type semiconductor, is identified as one of the most promising materials. It can be synthesized from inexpensive precursors, and has a band gap of 2.4-2.5 eV, providing sufficient light absorption in the visible region[20].

1.4.2. Electronic and Crystal Structure

$BiVO_4$ has three different crystal structures, which are tetragonal scheelite, monoclinic scheelite, and tetragonal zircon. Monoclinic scheelite phase is identified as the most photoactive phase. In this structure, V atoms are coordinated by four O atoms in a tetrahedral site, and a Bi atom is coordinated by eight O atoms from eight different VO_4 units[21]. When compared with another phase, for instance tetragonal scheelite, monoclinic scheelite has a high degree of asymmetry, with different V-O and Bi-O bond distances. This factor results in high degree of anisotropic electronic structure due to this asymmetry[22]. The crystal structure of monoclinic $BiVO_4$ is shown in Figure 1.6.

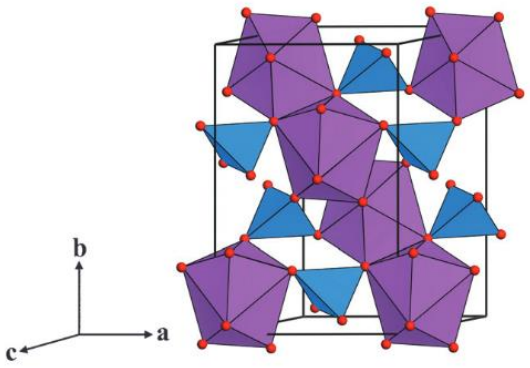

Figure 1.6. Crystal structure of monoclinic $BiVO_4$[5].

The n-type conductivity of $BiVO_4$ is suggested to result from oxygen vacancies which act as shallow donors[23,24]. The electronic structure of $BiVO_4$ valence and conduction bands is subjected to multiple experimental and theoretical studies. It is suggested that the valence band is comprised of O 2p and Bi 6s, orbitals, whereas the conduction band is mostly comprised of V 3d orbitals[5,25].

1.4.3. Routes to Improve $BiVO_4$ Water Oxidation Activity

Doping: In order to improve $BiVO_4$ water oxidation activity, n-type doping is one of the strategies to enhance the n-type conductivity of $BiVO_4$. To that end, substitutional doping of W^{6+} or Mo^{6+} with V^{5+}, or inducing oxygen vacancies or interstitial hydrogen are the common strategies[26–29]. Such defects can act as shallow donors for $BiVO_4$. The donor density can be quantified from Mott-Schottky analysis, as described in the experimental methods section.

Cocatalyst and overlayer deposition: The surface overlayer modifications typically aim to tune the surface properties of $BiVO_4$, such as OER catalysis, or surface recombination. Variety of modifications were performed in the literature, such as Co-Pi, FeOOH, NiOOH, NiOOH-FeOOH, $NiFeO_x$, NiFe layered double hydroxide, $CoFeO_x$, CoO_x, Co hexacyanoferrate, PdO_x, IrO_x, and Pt[30–37].

Other types of overlayers which do not necessarily have a catalytic contribution towards OER. Such modifications typically are utilized as passivation layers which may inhibit surface recombination, or protection layers which are utilized to inhibit photocorrosion and/or dissolution of the active material. To that end, TiO_2, Al_2O_3, and $ZnFe_2O_4$ were reported previously in the literature[38–40].

Heterojunction formation: Heterojunction formation refers to the coupling of $BiVO_4$ with another semiconductor, particularly at the FTO/$BiVO_4$ interface. In order to have an efficient heterojunction by adding a new material as an electron transport layer, it should have good electron mobility and diffusion length compared to $BiVO_4$, type II band alignment in which being electron conductive and hole mirroring, and high porosity to allow high $BiVO_4$ loading. The commonly utilized materials for this end are WO_3, SnO_2, TiO_2, Al-ZnO, and $CuWO_4$[40–45].

1.5. $CuBi_2O_4$-based Photocathodes for Hydrogen Evolution Reaction

1.5.1. Why $CuBi_2O_4$?

$CuBi_2O_4$ was first identified as a potential photocathode candidate to drive HER from a high-throughput experimental semiconductor screening study in 2007[46]. Since then, it is found that $CuBi_2O_4$ has a narrow band gap of 1.5-1.8 eV[47,48], has a CBM higher energy than the HER energy[49], and has a very positive flat-band potential which is >1.0 V_{RHE}[50,51]. All of

these features make $CuBi_2O_4$ a very attractive photocathode candidate for photoelectrocatalytic HER.

1.5.2. Electronic and Crystal Structure

The $CuBi_2O_4$ crystal structure was reported to be tetragonal, with P4/ncc space group[52]. The schematic for the crystal structure is given in Figure 1.7. In the schematic representation, the blue spheres represent Bi, orange spheres represent Cu, and the red spheres represent O atoms. The structure contains CuO_4 square planar complexes stacked in a staggered manner along the c-axis. Between the CuO_4 groups, each Bi atom is connected to six O atoms with three different bond lengths[52].

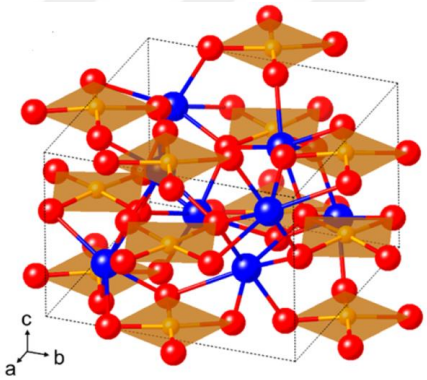

Figure 1.7. Schematic representation for the $CuBi_2O_4$ crystal structure[6].

It is found that the p-type conductivity of $CuBi_2O_4$ arises from the Cu vacancy states near the valence band edge[53]. The characteristics of the valence band and the conduction band, however, are a matter of some debate in the literature. Sharma et. al. suggested that VB and the CB edges arise from the combination of O 2p and Cu 3d orbitals in light of their DFT analysis[53]. Oropeza et. al. suggested from their combined experimental and DFT studies that CBM and VBM composed of Cu 3d and O 2p orbitals[54], similar to before mentioned study. Cooper et. al. proposed that VBM and CBM are comprised of Cu 3d states without any significant contribution from other orbitals[55].

1.5.3. Routes to Improve $CuBi_2O_4$ Water Reduction Activity

Doping: Doping $CuBi_2O_4$ to enhance its p-type conductivity is one of the strategies to enhance its water reduction activity. Kang et. al. demonstrated substitutionally doping Bi^{3+} with Ag^+ can enhance the majority carrier concentration[56]. In another study, Wang et. al. suggested a forward gradient self-doping route to induce a gradient of Cu vacancies to enhance the charge separation[57]. Cu vacancies introduced by annealing in O_2 environment is also suggested to enhance charge separation and $CuBi_2O_4$ activity[58,59]. In a different work, Co-doping into $CuBi_2O_4$ was suggested to enhance the interfacial charge resistance and reduce the charge carrier recombination, without changing the acceptor density[60].

Cocatalyst deposition: Cocatalyst deposition is a route to enhance the charge transfer kinetics of $CuBi_2O_4$ towards HER. Cocatalyst modifications of RuO_x, Pt, and MoS_2 were previously demonstrated in the literature to enhance the catalytic activity of $CuBi_2O_4$ surface[57,61–63].

Heterojunction formation: Heterojunction formation can be used to enhance the hole collection efficiency at the FTO/$CuBi_2O_4$ interface. Song et. al. suggested that a p-type Cu doped NiO ultrathin layer can be used to enhance the hole collection efficiency at the FTO interface[64]. Similarly in another work Fe doped NiO_x at the FTO interface suggested to enhance the hole collection properties of the device[58]. CuO phase segregation from $CuBi_2O_4$ near to the FTO interface is also suggested to act in a similar manner to improve the $CuBi_2O_4$ activity.

1.6. Charge Carrier Dynamics in Photoelectrodes

When describing the working principle of a photoelectrocatalyst, it is said that electron hole pairs are generated as a result of photoexcitation, and the charge carriers migrate to the surface to drive the respective reaction, OER or HER. However, end-to-end conversion is kinetically challenging, as there are series of steps that charge carriers have to go through which are on different time scales[65]. These processes are summarized in Figure 1.8. given below. In the semiconductor, photoexcitation leads to generation of electron-hole pairs, which enables the transport of charges. The transport of the charges occurs via drift in the space-charge region due to the potential gradient, whereas in the bulk, the charge carriers separate via diffusion. However, because of the strong ionic character of the metal oxide

photoelectrodes, the excited charge carriers can interact with the lattice to form polarons. Formation of polarons, or self-trapped charge carriers, result in conduction via thermally activated hopping mechanism, as opposed to conduction of delocalized charge carriers in the valence or the conduction band, which limits the mobility[66,67]. Charge carrier trapping in the defect sites in the bulk, and in the space-charge region are also considered as loss mechanisms, as these are said to be too unreactive to contribute to the energy conversion[68].

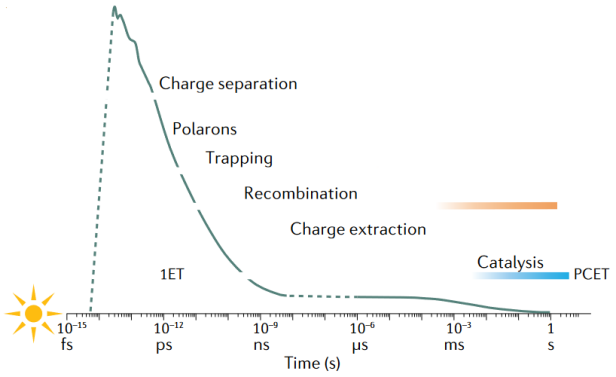

Figure 1.8. The charge carrier dynamics timescale in photoelectrodes[65].

At the photoelectrode surface, due to the termination of the crystal lattice structure of the metal oxide, chemical defects, or surface-states, can be formed. These surface-states can act as charge carrier traps, resulting in localization[69,70]. However, determining the role of the surface-state, whether it is to mediate recombination loss, or to drive charge separation and/or water oxidation/reduction catalysis is non-trivial.

The surface localized charge carriers are known to react in the time scale of millisecond to second[71]. This suggests that the charge carrier dynamics at the surface-states can occur in this time regime as well. Even though this feature makes it challenging for charge carriers to react at the photoelectrode surface without going through recombination, it makes it easier to study such dynamics with less sophisticated instrumentation.

1.7.About this study

This study aims to understand how different modifications at the photoanode and photocathode surfaces can alter their performance. More importantly, what are the roles of these modifications in the context of charge carrier trapping and/or recombination at the semiconductor surface. Such processes are crucial to understand how does a photoelectode

work and how can one design and tune surface properties to achieve maximum charge carrier utilization. To that end, we have studied $BiVO_4$ based photoanodes, and $CuBi_2O_4$ based photocathodes, which are very promising materials to achieve high efficiency PEC water splitting. $BiVO_4$ and $CuBi_2O_4$ with optimized surface properties may be used in tandem in the future, to produce H_2 and O_2 from water without any external bias.

In this study, we have modified $BiVO_4$ surface with TiO_2 overlayer using atomic layer deposition (ALD). We have shown that such modification can significantly enhance the water oxidation activity, by only modifying the surface. Passivation of the photogenerated electron trapping process at the surface states and enhancement of charge separation efficiency were suggested to be the rationale behind the activity increase. We have also investigated the effect of the surface composition of the $CuBi_2O_4$. We have shown that varying Cu amount can significantly change the charge carrier trapping process, and the water reduction activity.

In Chapter 2, the experimental procedures for the material synthesis, photoelectrochemical and structural characterizations were explained.

In Chapter 3, the effect of ultrathin TiO_2 overlayer on $BiVO_4$-based photoanodes was investigated.

In Chapter 4, charge carrier dynamics at the surface of $CuBi_2O_4$-based photocathodes was investigated. The effect of TiO_2 overlayer on these dynamics was explored.

Chapter 2. Experimental Methods

2.1.Synthesis Procedures

2.1.1. Electrodeposition

Electrodeposition is a solution-based synthesis method that utilizes a conductive substrate as a working electrode, a counter electrode and a reference electrode, and a plating solution. The applied potential in between the electrodes can drive the deposition reaction on the conductive substrate, and result in amorphous or polycrystalline materials[72]. It has many advantages as opposed to other chemical synthesis routes[73,74]. The plating solution composition, pH, temperature, additives, and the used solvent can be manipulated which can affect the morphology and crystal growth. The applied potential can be tuned to thermodynamically and kinetically control the reaction and the deposition time or charge passed through can be altered to vary the sample thickness. It allows conformal deposition which makes it easier to grow different materials as under/overlayer, which is a common strategy for device fabrication in the field of photoelectrochemical energy conversion. Also, it is a scalable method, which makes it a robust synthesis route for both small- and large-scale operations.

2.1.1.1. Electrochemical Synthesis of Nanoporous $BiVO_4$

The synthesis of $BiVO_4$ was performed with the method reported by Kim et. al[37]. The 3-electrode set-up consists of FTO (fluorinated-tin oxide, 6-9 $\Omega.square^{-1}$) on glass as the working electrode, a Pt coiled wire as a counter electrode, and a Ag/AgCl (sat'd KCl) as a reference electrode. The FTO substrates prior to deposition were cleaned in acetone, ethanol, and ultrapure water for 10 minutes each, in a sonicator. Then they were masked with a non-conductive PTFE (polytetrafluoroethylene) tape with a 6 mm diameter circular hole which exposes the substrate to obtain a homogeneous coating. To prepare the plating solution, first 1.66 g potassium iodide (0.4 M) was dissolved in 25 mL ultrapure water. The pH of the solution was adjusted to 1.7 with diluted nitric acid solution. Then 485 mg bismuth nitrate pentahydrate (0.04 M) was added to the solution and stirred until complete dissolution. A separate solution was prepared by dissolving 249 mg p-benzoquinone (0.23 M) in 10 mL ethanol. Then these solutions were mixed to obtain the final solution. The I^- ions facilitate

the formation of BiI_4^- complex in the solution. The p-benzoquinone was utilized to impede the deposition of metallic Bi, as opposed to BiOI[74]. The FTO-coated glass was faced towards the counter electrode whereas the reference electrode was placed to the side of the working electrode. A Biologic VSP-300 potentiostat was used for the electrodeposition, which was done under -0.1 V bias vs Ag/AgCl reference electrode for 2 minutes to obtain BiOI film. After electrodeposition, the electrodes were rinsed with ultrapure water and dried in air at room temperature. Then 530 mg vanadyl acetyl acetonate (0.4 M) was dissolved in 5 mL DMSO. This solution was dripped on the BiOI surface until complete coverage. The samples were annealed in a muffle furnace in air at 450 °C for 2 hours, with a 2 °C.min^{-1} temperature ramping rate. Then, the photoanodes were soaked in 1 M sodium hydroxide solution for 30 minutes to remove the excess V_2O_5 at the surface. Figure 2.1 shows the images of the photoelectrodes at various synthesis stages. Finally, the photoanodes were further annealed at 200 °C with flowing O_2 gas in a tubular furnace[75].

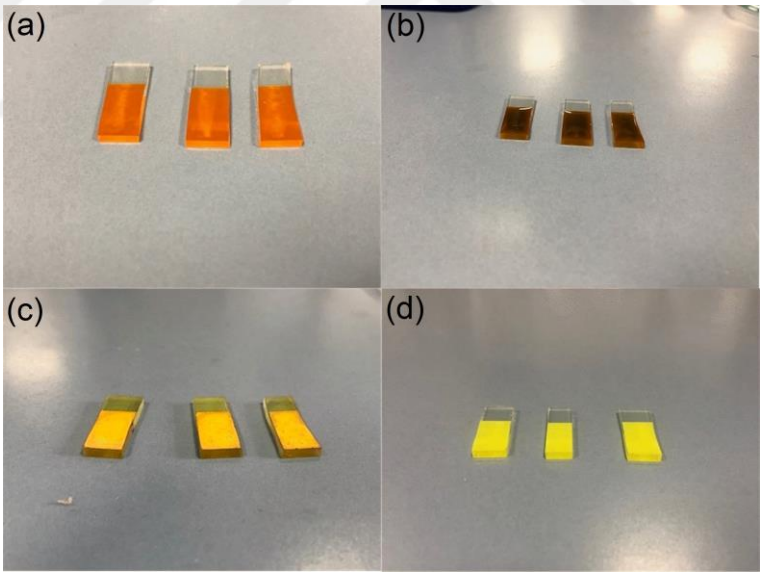

Figure 2.1. (a) Electrodeposited BiOI film, (b) BiOI film after drop casting $VO(acac)_2$ solution, (c) $BiVO_4$ photoanode after calcination with V_2O_5 impurity, (d) $BiVO_4$ photoanode after washing with 1 M NaOH.

2.1.1.2.Electrochemical Synthesis of Nanoporous $CuBi_2O_4$

The synthesis of the $CuBi_2O_4$ photocathodes were performed using an electrodeposition route reported previously in the literature[56]. Same 3-electrode configuration and FTO cleaning procedure was used, as described in the nanoporous $BiVO_4$ synthesis. Prior to deposition, the FTO substrates were masked using a PTFE tape with a 6 mm diameter

circular hole in the middle, to ensure homogeneous deposition. The non-aqueous electroplating solution was prepared using ethylene glycol as a solvent. 1.70 g of bismuth nitrate pentahydrate (0.1 M), and 0.244 g of copper nitrate hemi(pentahydrate) (0.03 M) were added to the solution, and the solution was stirred until complete dissolution. The substrate was faced towards the counter electrode, and the reference electrode was placed near to the working electrode. The electrodeposition was carried out at -1.8 V vs Ag/AgCl, until the charge passed through the cell became 0.8 $C.cm^{-2}$. The resulting Cu-Bi film was then annealed in a muffle furnace in air at 450 °C for 3 hours, with a 3.5 $°C.min^{-1}$ temperature ramping rate. Figure 2.2 given below shows the photoelectrode images after electrodeposition and after calcination.

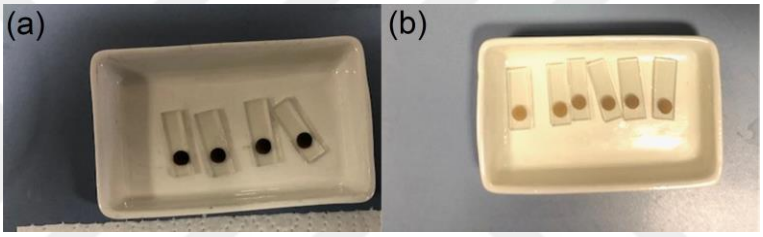

Figure 2.2. (a) Cu-Bi film after electrodeposition, and (b) $CuBi_2O_4$ after calcination.

2.1.2. Atomic Layer Deposition (ALD)

Atomic layer deposition is a technique that allows thin film coating with excellent thickness control and high uniformity. Successive cycles during the ALD allow for uniform film growth even in high-aspect-ratio substrates due to the self-limiting nature of the process[76]. It is a vapor phase deposition method, which consists of typically two reaction steps for each cycle. Before the start of the ALD, the chamber is vacuumed with a pump. For the first step of the cycle, the surface is oxidized by an oxidizing agent, together with a carrier gas, to facilitate the growth of the oxide material. Oxidizing agents such as, H_2O, O_2, O_3, or H_2O_2 can be used to this end. After this step, the chamber is swept by an inert gas, which can be N_2 or Ar, to remove the unreacted moieties. Then, the precursor gas is dosed to the chamber with a carrier gas, to react at the oxidized substrate surface[77]. The precursor may be heated to a certain temperature to increase its vapor pressure. After sweeping the unreacted species in the chamber with N_2, 1 ALD cycle would be completed. In order to grow oxide material and increase its thickness, same cycle is repeated.

For the ALD of TiO_2, titaniumisopropoxide (TTIP) is utilized as a precursor, and water is used as an oxidizing agent. N_2 gas was used both as a carrier gas, and to sweep the chamber. In the first step of the cycle, the surface of $BiVO_4$ is hydroxylated with H_2O vapor to ensure TiO_2 growth. The pulse duration of H_2O was 0.15 s with 15 s of N_2 flow. Then TTIP is dosed for 1 s with 15 s of N_2 flow to react at the surface to form to oxidize the TTIP bound on the surface, releasing isopropyl groups. The last H_2O pulse fully converts the layer to TiO_2. This process is repeated multiple times to increase the overlayer thickness on $BiVO_4$. The schematic representation of TiO_2 growth using ALD is given below as Figure 2.3.

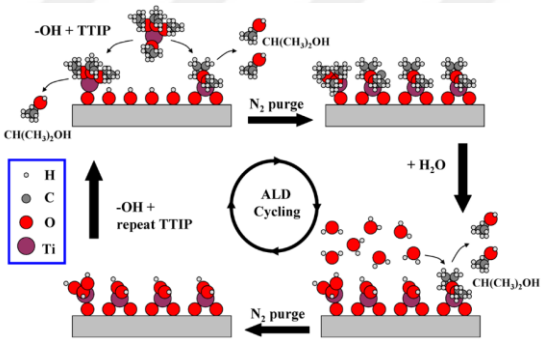

Figure 2.3. Schematic representation of the TiO_2 growth via ALD[7].

2.2.Photoelectrochemical (PEC) Characterizations

2.2.1. PEC Set-up

All of the photoelectrochemical characterizations were performed in a 3-electrode configuration, using a working electrode, a counter electrode which is a coiled Pt wire, and a Ag/AgCl(sat'd KCl) reference electrode. A commercial electrochemical cell made of quartz was utilized for the measurements, for full UV-visible light transmission through the cell towards the sample. For the light source, a 100 W Xe lamp which is coupled to a AM1.5G filter and a collimator, unless otherwise is stated. The power of the incident light was set to 100 $mW.cm^{-2}$, by calibrating with a thermal power sensor. A Biologic VSP-300 potentiostat was utilized to carry out the photoelectrochemical measurements.

The measured potential scale was converted to vs Reversible Hydrogen Electrode (scale) in order to be able to compare photocurrent onset values of electrodes at different pH values. Nernst equation given below was utilized to do the potential conversion:

$$V_{RHE} = V_{Ag/AgCl} + 0.059 \times pH + V^{\circ}_{Ag/AgCl} \qquad \text{Equation 2.1}$$

in which V_{RHE} is the applied potential with respect to the RHE; $V_{Ag/AgCl}$ is the applied potential with respect to the Ag/AgCl reference electrode; pH is the pH of the electrolyte solution; $V°_{Ag/AgCl}$ is the standard potential of the reference electrode (0.197 V_{RHE}).

2.2.2. Linear Sweep Voltammetry (LSV)

LSV is an electrochemical method, where the potential between the reference and the working electrode is swept with time between two values, and the current is recorded[78]. For PEC experiments, it can be done either under front illumination, back illumination, or in the absence of illumination. It is the most basic method to screen the activity of a given photoelectrode.

2.2.3. Cyclic Voltammetry (CV)

Like LSV, CV is also a potential sweep method. However, the potential modulation between the electrodes is cycled, as one cycle consists of sweeping from V_1 to V_2, then V_2 back to V_1. The number of cycles can be set as an experimental parameter. CV can be utilized to understand the redox processes happening on the electrode surface, their reversibility, and the stability of the electrode[78].

2.2.4. Chronoamperometry (CA)

Chronoamperometry is a method in which the applied potential between the reference electrode and the working electrode is fixed. The current response is measured as a function of time, after a potential step[78]. Such experiments in the context of PEC systems can be done for transient photocurrent measurements, and stability assessments.

2.2.5. Transient Photocurrent (TPC)

Transient photocurrent is a technique where a constant applied potential is applied between the electrodes like CA, and a light pulse is given to the sample for a certain duration. The current response in the photoelectrode in dark, under illumination, and again in dark is recorded, as a function of time. Such experiment can be carried out at various applied potentials, pulse durations, and illumination intensities, and are useful for understanding the charge accumulation/transfer behavior at the photoelectrode surface[79]. TPC measurements done in this study were performed at various applied potentials, using either 50 W power LED, or 100 W Xe lamp as light source, with 50 ms, 500 ms, or 5 sec pulse widths.

2.2.6. Incident Photon-to-Current Efficiency (IPCE)

IPCE is a method to assess the quantum efficiency of the photoelectrode. It is the fraction of the incident photons that are converted to a current flow in the cell. It is typically done at various wavelengths of incident light.

In this study, IPCE measurements were done in the same 3-electrode set-up, using a Newport IPCE set-up, consisting of a 300 W Xe lamp, and a monochromator. IPCE values were calculated using the equation below:

$$IPCE = \frac{[j\ (mA.cm^{-2}) \times 1240\ (V.nm)]}{[P_{\lambda}(mW.cm^{-2}) \times \lambda\ (nm)]} \qquad \text{Equation 2.2}$$

where j is the photocurrent density, λ is the wavelength of the incident light, and P_{λ} is the power of incident light at wavelength λ.

2.2.7. Open-Circuit Potential (OCP)

Open-circuit potential is defined as the potential difference between the reference electrode and the working electrode, in the absence of any current flow through the cell. For photoelectrode systems, OCP can be measured in dark and under illumination. The difference between the dark and light OCP is the Fermi level difference of the majority carrier under such conditions. This value can be interpreted as thermodynamical driving force of the photoelectrode[6].

2.2.8. Electrochemical Impedance Spectroscopy (EIS)

Electrochemical impedance spectroscopy is an AC (alternating current) based technique, which measures the current response to an AC potential signal input, at various frequencies. Depending on the current response, a given electrochemical system can be studied and modeled, using circuit elements such as resistors and capacitors. EIS is typically done at a single applied potential, however it can be done in a potential window, to study the capacitance and resistance development of a photoelectrode as a function of potential. Imaginary part of the impedance vs the real part of the impedance can be plotted, which is referred to as Nyquist plot. Randle's circuit is a commonly utilized model for fitting the EIS data, which is given as Figure 2.4. The model consists of R_s which refers to the ohmic resistance in the cell resulting from the electrolyte, electrical contacts, and wires, R_{ct} corresponding to the charge transfer resistance across the photoelectrode/electrolyte interface, and constant phase element (CPE) which stands for the capacitance at the photoanode/electrolyte interface. CPE is generally used instead of an ideal capacitor because of the inhomogeneity at the metal oxide photoelectrode surface, as well as the roughness, porosity, and complexity of the Helmholtz layer[80].

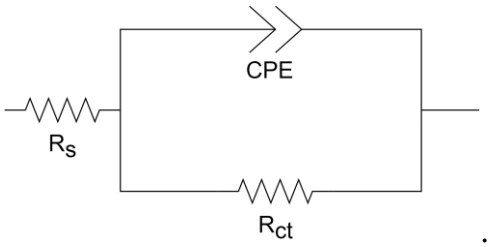

Figure 2.4. Randles circuit model.

2.2.9. Mott-Schottky Analysis (MS)

Mott-Schottky analysis is a method to assign the flat-band potential and the donor (acceptor) density of a given n-type (p-type) photoelectrode. Flat band potential can be defined as the applied potential in which the conduction and valence bands become flat, and the donor density (N_d) can be defined as the concentration of the donor ions in the space-charge region. It is an EIS based technique, in which impedance of the photoelectrode in dark is measured in a given potential window. The reciprocal of the second power of the

measured space-charge capacitance (C_{SC}^{-2}) is plotted with respect to the applied potential. For the calculation of N_d or N_a, the linearly increasing or decreasing region is fitted with a linear curve. The intersection with the potential axis is said to be the flat band potential. The slope of the curve can be used to calculate the N_d or N_a, using the Mott-Schottky equation given below:

$$C_{SC}^{-2} = \frac{2}{\varepsilon_0 \varepsilon_r A^2 e N_D}\left(V - V_{FB} - \frac{k_B T}{e}\right) \qquad \text{Equation 2.3}$$

where C_{sc} is the capacitance at the space-charge layer, ε_0 is vacuum permittivity, ε_r is the relative permittivity of the material, A is the surface area, e is the charge of an electron, N_D is the dopant density, V is the applied potential, V_{FB} is the flat-band potential, k_B is the Boltzmann constant, and T is the absolute temperature.

The type of the conductivity of the photoelectrode can be determined with the Mott-Schottky analysis as well. If the linear slope is positive, the photoelectrode is said to be n-type, and the N_d can be calculated. If it is negative, photoelectrode is said to be p-type, and the N_a can be calculated from the slope[81].

The Mott-Schottky analysis performed in this study were done in the absence of illumination, with the potential range of 100.0 kHz-100 mHz with 10.0 mV voltage signal amplitude.

2.2.10. Electrochemically Active Surface Area (ECSA)

Electrochemically active surface area (ECSA) measurements are used to assess the surface area of the photoelectrode. In this measurement, the surface area is determined indirectly by measuring the double layer capacitance (C_{DL}). The surface area is said to be proportional to the measured C_{DL}. In order to determine the capacitance, CV is carried out in a non-faradaic region (in dark for photoelectrodes), at various potential scan rates. Then, the $(j_{anodic}-j_{cathodic})/2$ is plotted with respect to the scan rate. The slope of the linear fit of these data points is said to be the C_{DL}[82].

2.2.11. Charge Injection and Separation Efficiency

In order to assess and de-couple the charge separation and catalytic performance of the photoelectrode, charge injection and separation efficiency can be calculated. Theoretically,

under any given potential, the measured photocurrent can be calculated by the equation given below:

$$j_{PEC} = j_{absolute}\eta_{separation}\eta_{injection} \quad \text{Equation 2.4}$$

j_{PEC} is the photocurrent density, $j_{absolute}$ is the maximum photocurrent density of the photoelectrode based on its absorption coefficient (α), and assuming 100% absorbed light-to-current efficiency, $\eta_{separation}$ is the charge separation efficiency, and the $\eta_{injection}$ is the charge injection efficiency from the photoelectrode surface to the electrolyte. $\eta_{separation}$ is usually <1, typically because of the poor electron-hole diffusion lengths, poor material conductivity, or overwhelming bulk recombination. $\eta_{injection}$ is also <1 in the absence of a scavenger for the minority charge carriers, due to the kinetic limitations at the photoelectrode surface. $\eta_{separation}$ and $\eta_{injection}$ can be calculated from the equations given below:

$$\eta_{separation} = \frac{j_{scavenger}}{j_{abs}} \quad \text{Equation 2.5}$$

$$\eta_{injection} = \frac{j_{OER/HER}}{j_{scavenger}} \quad \text{Equation 2.6}$$

Where $j_{scavenger}$ is the measured photocurrent density at a given potential in the presence of an electron or hole scavenger, $j_{OER/HER}$ is the photocurrent density due to the reaction of interest, such as oxygen evolution or hydrogen evolution reaction. In the presence of a scavenger, due to superior charge transfer kinetics, $\eta_{injection}$ is assumed to be unity. Thus, under such conditions, equation 2.4 becomes equation 2.5, and the separation efficiency can be calculated, at a given potential. j_{abs} is a quantity which depends on the band gap of the photoelectrode, as well as the absorption coefficient.

2.3.Structural Characterizations

2.3.1. X-ray Photoelectron and Auger Electron Spectroscopy (XPS, AES)

XPS is an X-ray based structural characterization technique, which is surface sensitive. It is based on photoelectric effect in which an electron is ejected from a surface as a result of incident photons towards the surface of a material. The kinetic energy of the ejected photoelectron is detected by the instrument, and the binding energy can be calculated from the formula given below:

$$BE = h\nu - KE - \Phi_{XPS}$$ Equation 2.7

Where BE is the binding energy of the electron, $h\nu$ is the incident photon energy, KE is the kinetic energy of the photoelectron, and Φ_{XPS} is the work function of the instrument.

The binding energy of the electrons is element and valency specific. This makes XPS is a useful technique to determine the elemental composition, and oxidation states of the atoms at the surface. XPS is used to acquire information within the outer most 10 nm of the material, but not from the bulk of the material. However, the incident X-rays may penetrate up to μm scale into the material. The photoelectron inelastic mean free path (IMFP) determines the surface sensitivity of the technique. IMFP is a function of electron kinetic energy, and the universal curve which gives such relation is given below:

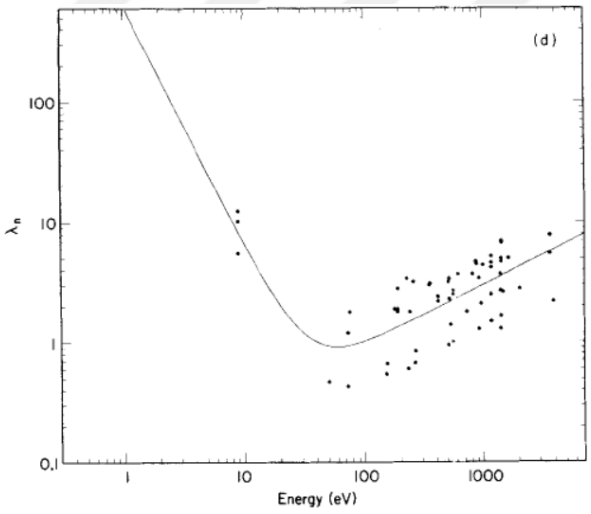

Figure 2.5. The universal curve of inelastic mean free path of an electron as a function of its kinetic energy[8].

Since the generated photoelectron kinetic energies are in the order of 1000 eV, the mean free path of the ejected electrons, and thus the surface sensitivity of the technique becomes 1-10 nm[9].

In the obtained XPS spectras, the signals coming from Auger electrons are also present. After the photoelectron is ejected from the atom, a deexcitation from the outer shell electron to the core hole may occur. As a result, Auger electron is ejected, in which their kinetic energy does not depend on the incident photon energy, but the energy difference between the inner and outer shell electrons. A representative figure for XPS and AES process is given below:

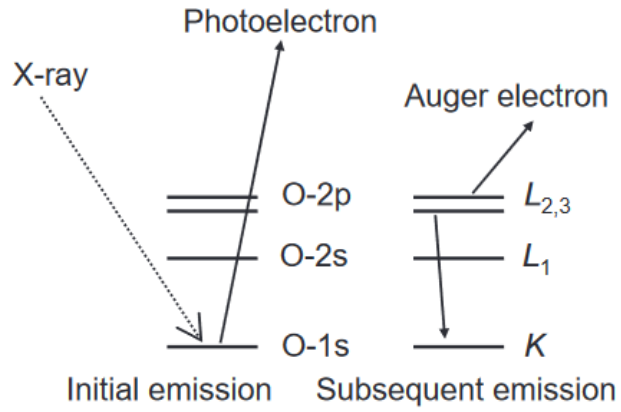

Figure 2.6. Schematic representation of XPS and AES processes[9].

For this study, XPS analysis was carried out by using a commercial Thermo Kα laboratory XPS system, which uses a monochromatized Al Kα as the X-ray source. The quantification of the TiO_2 overlayer thickness on $BiVO_4$ photoanodes were performed as described in the Appendix section.

2.3.2. Raman Spectroscopy

Raman spectroscopy is a technique which is used to assign molecular vibrational modes of a given material. It can help to identify the phase of the material. It is an inelastic scattering-based method, rather than light absorption/transmission. The monochromatic high intensity light beam, typically generated by a laser, is sent to this sample surface. The molecule is excited to a higher vibrational "virtual" state. Since this state is a short-lived state, system goes back to the initial state and a photon is irradiated. In Raman scattering, the incident light interacts with the molecule and polarizes the electron cloud in the molecule. Then, energy from photon to molecule or molecule to photon will be transferred, so that the energy of the scattered photon is different from the energy of the incident photon, by one vibrational energy unit. Raman scattering is inherently a weak process, such that only one in every 10^6-10^8 photon will be scattered, which makes it necessary to use a strong light beam as the incident light[83].

2.3.3. X-ray Diffraction (XRD)

XRD is an X-ray based technique, which is utilized to assign the phases of a single crystal or polycrystalline material, atomic planes of these phases, their crystal structures and their crystallinities. In this technique, incident X-rays are sent to the material with a certain angle with respect to sample plane, θ. The scattered electrons from the atomic planes of the sample, either constructively or destructively interfere. Depending on the signal coming from the constructive interference as a function of the 2θ angle is called the XRD spectra. The diffraction of X-rays from the atomic planes of the material interferes constructively, following the Bragg's law given below:

$$n\lambda = 2dsin\theta \qquad \text{Equation 2.8}$$

where n is the order of reflection, λ is the wavelength of the incident beam, d is the spacing between the atomic planes, and θ is the angle of reflection[84].

The XRD spectras for this study was obtained from Bruker D2 Phaser diffractometer.

2.3.4. UV-visible Absorbance and Tauc Analysis

UV-visible absorption spectroscopy is a tool to assess the photon absorption properties of a material over the UV and the visible spectrum range. It gives information on the electronic transitions of the material. The fraction of transmitted light follows the Beer's law given as:

$$-\log_{10}\frac{I}{I_0} = \varepsilon cl = A \qquad \text{Equation 2.9}$$

in which A is the absorbance, ε is the molar absorptivity coefficient, c is the concentration of the absorbing species, and l is the path length of the light through the sample. For semiconductor photoelectrode, UV-vis can be used to assign the optical band gap, since it gives information about the electronic transitions between the valence band and the conduction band. By generating a Tauc plot, the value of the optical band gap, and the type of the band gap, whether it is direct or indirect can be determined. The equation for the Tauc analysis is given below[81]:

$$(\alpha hv)^{\frac{1}{n}} = A(hv) - E_g \qquad \text{Equation 2.10}$$

Where E_g is the band gap energy, and the value of n depends on the nature of the electronic transition. For an allowed direct transition n=1/2 whereas for allowed indirect transition n=2.

The UV-vis analysis performed in this study was performed using Shimadzu UV-3600 UV-VIS-NIR Spectrometer, in the diffuse reflectance mode. The reflectance data is then converted to absorbance with the Kubelka-Munk transformation given below:

$$\frac{k}{s} = \frac{(1-R_\infty)^2}{2R_\infty}$$ Equation 2.11

In which k is the absorption coefficient, s is the scattering coefficient, R_∞ is the diffuse reflectance[85].

2.3.5. Field Emission Scanning Electron Microscopy (FESEM)

Field emission scanning electron microscopy (FESEM) is a method for obtaining topographical images from a given sample at magnifications from 10x to 300000x. The difference between FESEM and scanning electron microscopy (SEM) is using an electron beam produced by a field emission source which provides images with higher clarity and less distortion with 3 to 6 times better resolution. In principle, a focused electron beam scans the surface of the sample and generates secondary electrons. These electrons are collected by detectors to create an image from the surface[86].

FESEM images in this thesis were obtained via Zeiss Ultra Plus Field Emission Scanning Microscope at different magnifications.

Chapter 3. Modifying the Electron-Trapping Process at the $BiVO_4$ Surface States via the TiO_2 Overlayer for Enhanced Water Oxidation

3.1.Introduction

One of the important bottlenecks for $BiVO_4$ photoelectrochemical (PEC) activity is its slow kinetics for oxygen evolution reaction (OER) and charge transfer across semiconductor photoelectrode/electrolyte interface[87,88]. It is known that OECs can improve $BiVO_4$ performance either by improving the OER kinetics and increasing the charge transfer rates at the photoanode/electrolyte interface or by passivating the surface states. Surface states are mid-band energy states which can act as recombination centers for the charge carriers[89]. In fact, various overlayers such as NiO_x and CoPi have been utilized for surface state passivation on $BiVO_4$, without any catalytic improvement towards OER[90–93]. However, it is reported that the deposition of OECs (oxygen evolution catalysts) on $BiVO_4$ could deteriorate the performance of $BiVO_4$ due to increased recombination at the interface of $BiVO_4$/OEC[93]. These studies indicate that optimizing the $BiVO_4$ surface in regard to minimal surface recombination is of utmost importance in improving the water oxidation activity of the photoanode.

Deposition of other oxides such as TiO_2 which are not considered as an OEC has been reported to improve the water oxidation activity of hematite photoanodes. Feng et al. reported that decorating the grain boundaries of hematite with TiO_2 by a chemical bath deposition method boosted the PEC performance due to enhanced charge separation efficiency and improved charge transfer to the electrolyte[94]. In a similar hierarchical structure, it was shown that the modification of the hematite surface by deposition of TiO_2 overlayer led to the passivation of the surface states and reduction in the surface recombination, which resulted in increasing the photovoltage and enlarged band bending[95]. Hence, utilizing other overlayers, not necessarily the OECs, which could make a proper interface with $BiVO_4$ could also improve the water oxidation activity of $BiVO_4$ photoanodes.

The deposition of TiO_2 on $BiVO_4$ as a protective layer has been depicted by several groups. Kim et al. demonstrated that deposition of ZnO and TiO_2 on $BiVO_4$ nanopillars by atomic layer deposition (ALD) enhanced the PEC performance[96]. They showed that the

heterojunction between ZnO and $BiVO_4$ improved charge separation and the TiO_2 layer inhibited the photoanode degradation. TiO_2 deposition on $BiVO_4$ had a negligible effect on increasing the photocurrent. McDowell et al. used ALD for coating TiO_2 on $BiVO_4$ [97]. They loaded Ni and Co on $BiVO_4/TiO_2$ film and showed that the TiO_2 layer acted as a protective layer in an alkaline environment and increased the lifetime of photoanode. Activity increment was supposed to be due to Ni and Co catalysts on top of the TiO_2 layer. However, they did not study the effect of TiO_2 alone on the performance of $BiVO_4$. Hwang and coworkers fabricated 3 layered $SnO_2/BiVO_4/TiO_2$ photoanode which show photoactivity higher than bare $BiVO_4$[98]. They attribute the improvement to enhanced charge separation due to type-II heterojunction formation between $SnO_2/BiVO_4$. The TiO_2 overlayer was utilized to protect the underlying photoanode from photocorrossion.

The OER activities enhanced by deposition of titanium oxides on $BiVO_4$ have also been demonstrated. Tian and coworkers fabricated a core-shell structure of $BiVO_4/TiO_{2-x}$ by coating TiO_2 on nanoporous $BiVO_4$ using ALD, followed by hydrogen plasma treatment at room temperature[99]. Amorphous TiO_{2-x}, composed of Ti_2O_3 and Ti_4O_7, showed catalytic activity for the OER and also suppressed the photocorrosion of black $BiVO_4$. Their X-ray photoelectron spectroscopy (XPS) and electron energy loss spectroscopy (EELS) investigations showed the Ti^{3+} rich phase was present at the top surface for the active phase. However, TiO_2 did not show any OER activity. In another work, $BiVO_4/TiO_2$ heterojunction was studied, where hydrogen treatment for the top TiO_2 layer was utulized[100]. They claim to alter the band alignment from type-I to type-II with this method, thus they achieved higher water oxidation activity due to the enhanced photoabsorption and hole transport. Monfort et. al. demonstrated that TiO_2 overlayers could improve the photocurrent and the hydrogen production rate of bare $BiVO_4$ photoanode[101]. Still, the origin of this improvement -whether TiO_2 layers enhanced the catalytic activity, suppressed the surface recombination, or enhanced charge separation- was not elucidated. In another study, it was suggested that the TiO_2 overlayer on $BiVO_4$ might passivate the electron-hole recombination and the back-reduction of the oxidized species at the interface[102]. Chen and coworkers investigated the effect of surface states on oxygen-vacancy-rich reduced $TiO_2/BiVO_4$ photoanode. They have demonstrated that the reduced TiO_2 overlayer could passivate surface states with slow water oxidation kinetics whereas it increased the density of holes that were related to oxygen

vacancies. Moreover, they claimed that reduced TiO_2 passivated the irreversible electron trapping process of VO_2^+ to VO^{2+} at the surface[103].

Herein, we demonstrated that the deposition of an ultrathin layer of TiO_2 on nanoporous $BiVO_4$ by ALD enhanced the water oxidation activity of $BiVO_4$ significantly. Our results showed that the thickness of TiO_2 was critical in the PEC performance of $BiVO_4$. We emphasized that the photogenerated electron trapping mechanism at the surface states was suppressed via TiO_2 deposition for the first time, facilitating higher electronic photoconductivity. Furthermore, the passivation of surface states via ultrathin TiO_2 overlayer resulted in enhanced band bending and charge separation to increase the water oxidation performance of $BiVO_4$. Thicker TiO_2 overlayer also passivated surface states but deteriorated the PEC activity simultaneously due to increased charge transfer resistance.

3.2.Experimental Procedure

The $BiVO_4$ photoanodes were synthesized, and the ALD of the TiO_2 overlayer was carried out as described in Section 2.1. The PEC set-up used to carry out the experiments was also explained in Section 2.2.1. The structural characterizations such as XPS and FESEM were also described in Section 2.3.

3.3.Results and Discussion

LSV results presented in Figure 3.1a show the water oxidation activity of $BiVO_4$ modified by TiO_2 overlayers of varying thicknesses. Bi 4f, V 2p, Ti 2p, and O 1s XPS spectra given in Figure A1.1 summarize TiO_2 thickness-dependent spectral changes. Bi 4f and V 2p peak intensities decrease, whereas Ti 2p signal increases with increasing ALD cycles. This is a clear indication of overlayer growth on the $BiVO_4$ surface. Since the amount of TiO_2 deposited per cycle may vary between ALD systems, precursor types, precursor pulse lengths, reactor temperatures, and oxidizing agents, we quantify the overlayer thickness by analyzing the changes in the Ti 2p and Bi 4d XPS peak intensities. The fittings are presented in Figure A1.2 and the details of the analysis are given in Appendix A. The calculated TiO_2 overlayer thickness with respect to the number of ALD cycles is given as an inset of Figure 3.1a. ALD is a technique that allows thin film coating with excellent thickness control and

high uniformity. Successive cycles during the ALD allow for uniform film growth even in high aspect ratio substrates, due to the self-limiting nature of the process[76]. In fact, ALD studies done on ultrathin TiO_2 layers with titanium isopropoxide as the titanium precursor and H_2O as oxidant, confirm that the growth is self-limited[104]. The growth of TiO_2 thin films occurs with two half-reactions. Initially, titanium isopropoxide dissociatively chemisorbs on the hydroxylated oxide surface and subsequent desorption of produced isopropanol occurs. Then, H_2O fully oxidizes the titanium surface species to produce an atomic layer of TiO_2[105,106]. Considering the self-limiting nature of both half-reactions, it can be expected to obtain uniform growth of ultrathin TiO_2 on $BiVO_4$. High binding energy shoulder at 531 eV in O 1s XPS spectrum (Figure A1.1d) confirms that bare $BiVO_4$ surface is hydroxylated and suitable for uniform TiO_2. This was partially confirmed by FESEM presented in Figure A1.3 within its image resolution, the deposition of ultrathin TiO_2 on $BiVO_4$ does not cause any change in the overall surface morphology. Raman spectras shown in Figure A1.4 only shows the spectral features of $BiVO_4$[107], due to TiO_2 being an ultrathin layer, rather than in bulk. XRD analysis did not show any peaks (not shown) that could be attributed to the reflections from TiO_2 planes, even for the thickest layer. The lack of long-range order might be expected due to the low-temperature ALD of TiO_2, however, we note that the ultrathin layers could make XRD measurements challenging.

LSV curves presented in Figure 3.1 demonstrate that the optimum TiO_2 thickness for the superior water oxidation activity is determined to be 1.3 nm. When the thickness of the TiO_2 overlayer is thinner than 1.3 nm the improvement in the water oxidation activity of $BiVO_4$ is less profound. This can be attributed to the partial TiO_2 coverage on the surface. At higher thicknesses, the photocurrent starts to decrease due to the increased charge transfer resistance at the photoanode surface. The onset potential also shifts cathodically from ~0.2 to ~0.1 V_{RHE} with the TiO_2 deposition. The EIS measurements were also done for photoanodes with different TiO_2 overlayer thicknesses. The data is fitted using Randle's model with a constant phase element, which is shown in Figure 3.1b as an inset. The model consists of R_s which refers to the ohmic resistance in the cell resulting from the electrolyte, electrical contacts, and wires, R_{ct} corresponding to the charge transfer resistance across the photoelectrode/electrolyte interface, and constant phase element (CPE) which stands for the capacitance at the photoanode/electrolyte interface. CPE is generally used instead of an ideal

capacitor because of the inhomogeneity at the metal oxide photoelectrode surface, as well as the roughness, porosity, and complexity of the Helmholtz layer[80]. The Nyquist plots for the EIS measurements are given in Figure 3.1b. For bare $BiVO_4$, the R_{ct} is equal to 736 Ω. Ultrathin TiO_2 overlayer results in a decrease in the R_{ct} values, in which for the optimum TiO_2 thickness, it decreases to 391 Ω. At higher thicknesses, the R_{ct} value starts to increase to 408 Ω at 1.4 nm, and 3500 Ω at 5.8 nm. The EIS measurement results are consistent with the LSV scans, as the obtained photocurrent is highest for $BiVO_4$/1.3 nm TiO_2 compared to other TiO_2 thicknesses and bare $BiVO_4$. For $BiVO_4$/OEC photoanodes, similar improvements in the R_{ct}s were reported: from 601.9 Ω to 257.3 Ω for α-FeOOH[108], and from 791.2 Ω to 239.6 Ω for $FeCoO_x$[109] cocatalysts. Although the improvement in the R_{ct} values is more profound with the deposition of cocatalysts, it can be said that enhancement resulting from TiO_2 overlayer is similar in terms of order of magnitude.

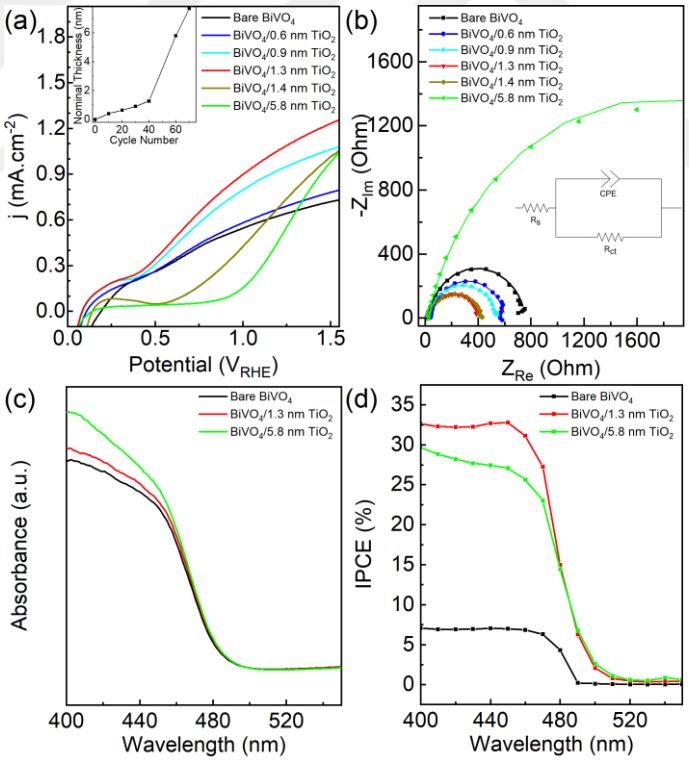

Figure 3.1. (a) LSV measurements under front illumination in 0.1 M KPi buffer with pH=7.4 (calculated nominal TiO_2 thickness with increasing ALD cycle number as an inset). (b) EIS measurement at 0.6 V_{RHE} in 0.1 M KPi with 0.5 M Na_2SO_3 with pH=7.8 (Randle's model as an inset). (c) UV-visible absorbance spectra. (d) IPCE measurement at 1.23 V_{RHE} in 0.1 M KPi buffer.

The optical properties of the photoanodes were investigated using UV-vis absorbance spectroscopy. As shown in Figure 3.1c, the absorbance of the photoanode increases slightly with the TiO_2 overlayer. This can be expected as TiO_2 can be utilized as anti-reflection coatings for solar devices[110]. However, the improvement in the UV-vis absorbance is insignificant in comparison with the photocurrent enhancement, therefore it has only a minor contribution to the overall photoanode performance. Tauc analysis given in Figure A1.5 shows that the band gap of $BiVO_4$ is 2.55 eV, which is consistent with the literature[111,112] and does not change with the TiO_2 overlayer. IPCE measurements were also carried out for bare $BiVO_4$, $BiVO_4$/1.3 nm TiO_2, and $BiVO_4$/5.8 nm TiO_2 photoanodes at 1.23 V_{RHE} applied potential in buffer solution as shown in Figure 3.1d. The IPCE value increased significantly from 7% to 33% at 400 nm with a 1.3 nm TiO_2 overlayer. However, with an increased overlayer thickness of 5.8 nm, IPCE drops to 29%, which is also consistent with the LSV results. In order to confirm that the origin of this improvement is not related to the change in porosity or the hydrophilicity of the $BiVO_4$ surface, we measured the electrochemically active surface areas (ECSA) of the photoanodes. As shown in Figure A1.6 the ECSA does not increase, in fact, it decreases with the increasing thickness of the TiO_2 overlayer, indicating that the improvement in the photocurrent is related to the enhanced OER kinetics, suppression of carrier recombination in the photoanodes, or enhanced charge separation. TiO_2 was deposited on FTO to test its catalytic effect on the water oxidation reaction. The cyclic voltammetry results in dark and under illumination are given in Figure A1.7 As can be seen from the graph, water oxidation onset potential is at around 1.9 V_{RHE} for FTO. After 1.3 nm thickness TiO_2 deposition the onset potential shifts anodically in dark and under illumination. This result indicates that ultrathin TiO_2 does not act as a cocatalyst, but as an extra layer that further impedes charge transfer in dark. Under illumination, no photocurrent was obtained from 1.3 nm TiO_2 indicating insignificant light absorption property for ultrathin TiO_2 itself. It is reported that TiO_{x-2} composed of Ti_2O_3 and Ti_4O_7 can act as a catalyst towards OER, while no such behavior was observed for TiO_2 with Ti^{4+} phase[99].

These results imply that the improvement of $BiVO_4$ activity with TiO_2 overlayer is not a result of enhancement of oxygen evolution kinetics, heterojunction formation, or improvement in light absorption. We propose that the ultrathin TiO_2 overlayer acts as an interfacial layer on the $BiVO_4$ surface, which passivates the $BiVO_4$ surface states and inhibits

surface recombination. The LSV measurement under front illumination shows that the photocurrent is enhanced by 72% at 1.23 V_{RHE} bias, from 0.64 $mA.cm^{-2}$ to 1.1 $mA.cm^{-2}$. Interestingly, the photocurrent improvement under back illumination was only 25% as shown in Figure A1.8. This issue will be addressed later in the text.

Figure A1.9 shows the transient photocurrent behavior of bare $BiVO_4$ and $BiVO_4/TiO_2$ photoanodes with various overlayer thicknesses. When the light is turned on, an anodic spike appears for all photoanodes. This behavior is a result of the charge separation and hole accumulation in the space-charge layer[113]. Then, the photocurrent density decays to a steady-state as the rate of generation of the charge carriers, recombination in the bulk and at the surface, and the charge transfer across the semiconductor/electrolyte interface equilibrates. For $BiVO_4$/ 1.3 nm TiO_2 photoanode, when the light is turned on, the anodic spike is higher than of bare $BiVO_4$, indicating enhanced charge separation. Also, the steady-state photocurrent density is higher for these photoanodes which means that the water oxidation performance is enhanced with TiO_2. Both charge separation and water oxidation performance are optimum for $BiVO_4$/1.3 nm TiO_2, however, at 5.8 nm TiO_2 overlayer thickness, the charge separation and the water oxidation activity decrease significantly, due to the increased charge transfer resistance at the photoanode surface. These findings are consistent with the LSV, EIS, and IPCE results presented in Figure 3.1a, b, and d.

In order to investigate the effect of TiO_2 on surface states and charge carrier recombination in greater detail, we performed TPC measurements using short white light LED pulses. The TPC results of $BiVO_4$, $BiVO_4$/1.3 nm TiO_2, and $BiVO_4$/5.8 nm TiO_2 are given in Figure 3.2a, 2b, and 2c, respectively. At the moment the light is turned on, it is expected to obtain an anodic spike, similar to the case with the TPC measurement done with 1.0 Sun AM1.5G light source, resulting from the charge separation and hole accumulation at the space-charge layer[113]. However, for bare $BiVO_4$ we observe a surprising cathodic peak (at >0.6 V_{RHE}) when the light is turned on. The anodic peak and decay to a steady-state value come later than this cathodic peak. For bare $BiVO_4$, when the applied potential increases from 0.45 to 0.60 V_{RHE}, we observe a decrease in the anodic spike at the light-on moment. However, after 0.60 V_{RHE} a discrete cathodic peak forms and maximizes at 0.80 V_{RHE} as demonstrated clearly in the inset of Figure 3.2a. At higher potentials, the intensity of the cathodic peak decreases. In our previous study, we attributed this feature to electron trapping

at the surface, due to the reversible redox couple V^{5+}/V^{4+}[114]. As the applied potential increases from 0.45 V_{RHE} to 0.80 V_{RHE}, the concentration of V^{5+} surface states increases as a result of electrochemical oxidation. These surface states act as trap states for the photogenerated electrons and can get reduced to V^{4+}. As the concentration of V^{5+} surface states increases and maximizes at 0.80 V_{RHE}, the extent of electron trapping also increases, simply due to the increasing amount of the reactants. At higher applied potentials, the amount of electron trapping decreases because of enhanced band bending[114]. As the built-in potential within the semiconductor increases it gets energetically less feasible for the photogenerated electrons to get trapped at the surface. Electron trapping at the surface states is a spontaneous process, as the electrons decay from the higher energy conduction band towards the surface states at the mid-band energy levels. This phenomenon at the $BiVO_4$ surface was also confirmed by Trzesniewski et al. as they observe an increase in the composition of the V^{4+} species at the surface with photocharging process without any external bias[115]

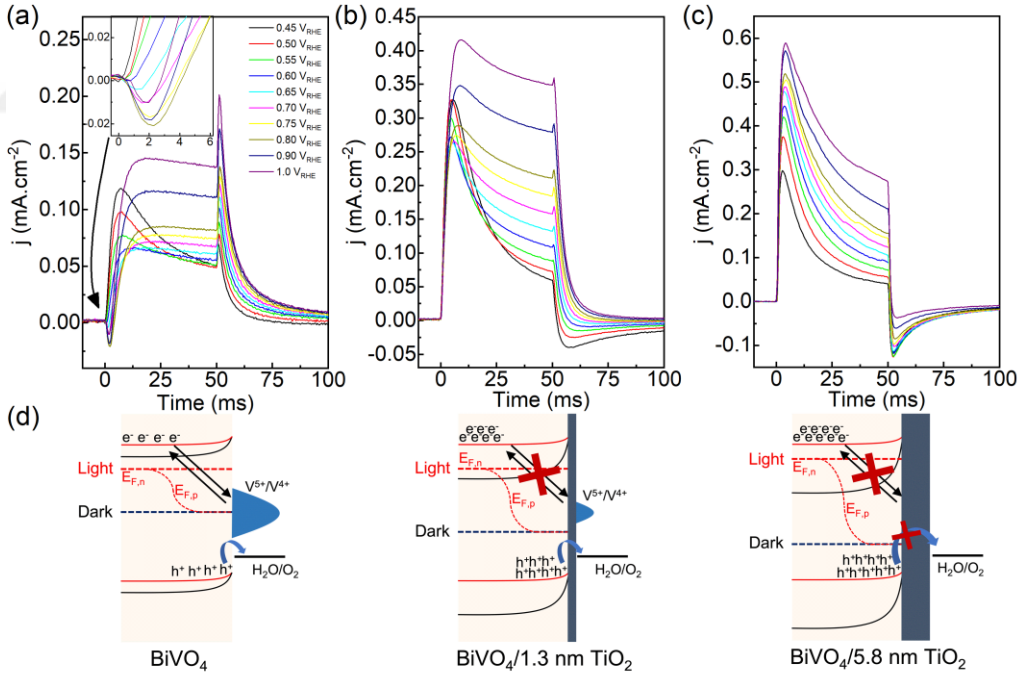

Figure 3.2. TPC measurements done with 50.0 ms white light LED pulse in 0.1 M KPi buffer solution for (a) bare $BiVO_4$ (inset shows the zoomed-in TPC when the light is turned on), (b) $BiVO_4$/1.3 nm TiO_2, (c) $BiVO_4$/5.8 nm TiO_2, and (d) simple schematic for electron trapping/de-trapping process on $BiVO_4$ surface and the effect of TiO_2 overlayer where red traces are the dark conditions, black traces are the illuminated conditions for band bending and Fermi levels, $E_{F,n}$ and $E_{F,p}$ are the quasi-Fermi levels for electrons and holes, respectively.

For $BiVO_4$/1.3 nm TiO_2 photoanode in the light-on moment, we do not observe a cathodic peak at any applied potential. However, in the applied potentials between 0.45 and 0.60 V_{RHE}, the anodic peak intensity decreases with potential. This indicates that the photogenerated electron trapping process is still present in these photoanodes but severely suppressed with the TiO_2 overlayer. After the trapping event, the photocurrent density reaches an anodic maximum. For $BiVO_4$/5.8 nm TiO_2 photoanode, we do not observe any cathodic peak at the moment when the light is turned on. Moreover, the anodic peak intensity increases monotonously with the increased potential, indicating that the electron trapping process at the surface is eliminated completely. For bare $BiVO_4$ at potentials higher than 0.60 V_{RHE}, the anodic maxima increase with potential, due to the increased band bending. For $BiVO_4$/1.3 nm TiO_2 and $BiVO_4$/5.8 nm TiO_2 photoanodes, the anodic maxima also increase with potential. Moreover, the anodic maxima that are achieved with this photoanode are much higher than of bare $BiVO_4$. We observe that the extent of the anodic pulse in the TPC measurement enhances with 1.3 nm TiO_2 overlayer, from 0.14 to 0.41 $mA.cm^{-2}$ suggesting that the amount of hole accumulation at the surface increases almost 3-fold. This is a result of enhanced charge separation and band bending in the semiconductor due to the TiO_2 overlayer. We propose that TiO_2 passivates the surface states, and therefore facilitates band bending by unpinning the Fermi level. Surface state passivation can also be evidenced by the reduced photogenerated electron trapping process at the surface. The anodic pulse increases further to 0.59 $mA.cm^{-2}$ with the 5.8 nm TiO_2 overlayer. This increase is a result of a completely diminishing photogenerated electron trapping process with a thicker TiO_2 overlayer.

After the trapping event, photocurrent density decays to a steady-state value. For all three photoanodes, the steady-state photocurrent increases with increased potential due to enhanced charge transfer kinetics with applied potential. The photocurrent decay from the anodic spike to the steady-state value is much more significant for $BiVO_4$/1.3 nm TiO_2. This is a result of enhanced charge separation, in the absence of any catalytic improvement towards OER. The hole accumulation in the space-charge layer of $BiVO_4$/1.3 nm TiO_2 photoanode is much more significant than of bare $BiVO_4$. However, TiO_2 overlayer suppresses electron trapping and charge recombination at the semiconductor surface, thus a

higher steady-state photocurrent is achieved for this photoanode. For a thicker TiO_2 overlayer of 5.8 nm, the decay to a steady-state photocurrent is much faster. This is a direct result of the increased charge transfer resistance at the surface due to the insulating effect of the thick TiO_2. Thus, the photogenerated holes can not react with water molecules and accumulate at the photoanode surface.

At the moment the light is turned off, we observe the anodic spike for bare $BiVO_4$ at each applied potential, which corresponds to the electron de-trapping process at the surface. Previously trapped photogenerated electrons de-trap when the light is off. Thus, the extent of electron trapping and de-trapping is correlated. The intensity of the anodic peak maximizes at 0.80 V_{RHE}, which is expected since at that potential the trapping intensity is maximized. For $BiVO_4$/1.3 nm TiO_2, the intensity of the anodic peak is less than that of bare $BiVO_4$ at each applied potential. This is consistent with our hypothesis that TiO_2 overlayer passivates the photogenerated electron trapping process. As the intensity of trapped electrons is decreased with the passivation layer, the intensity attributed to the electron de-trapping process should also decrease significantly. For $BiVO_4$/5.8 nm TiO_2, we do not observe an anodic peak when the light is turned off. Since the trapping event is eliminated in this photoanode, we do not observe any de-trapping as well. We also observe a cathodic overshoot when we turn the light off for $BiVO_4$/1.3 nm TiO_2, which is the evidence for the recombination of the electrons with the surface accumulated holes[116]. The cathodic overshoot is even more profound for $BiVO_4$/5.8 nm TiO_2. As thicker TiO_2 impedes the transfer of holes to the electrolyte radically, there is a significant amount of hole accumulation at the surface. Thus, when we turn off the light source, electrons recombine with these holes, leading to a substantial cathodic overshoot. It can be said that there is a trade-off between decreasing the electron trapping event and increasing the charge transfer resistance with the TiO_2 overlayer. Thus, the thickness of the passivation layer needs to be carefully optimized.

For the TPC measurement done in buffer with 0.5 M Na_2SO_3 as hole scavenger, we do not observe the cathodic/anodic peaks corresponding to the electron trapping/de-trapping as shown in Figure A1.10. Also, the anodic photocurrent jumps when the light is turned on is higher for $BiVO_4$/1.3 nm TiO_2 than for bare $BiVO_4$ photoanode. This further confirms that the charge separation, thus the band bending is enhanced with the TiO_2 overlayer. However,

for $BiVO_4$/5.8 nm TiO_2 photoanode, the photocurrent does not saturate at a steady-state value, instead, after reaching a maximum, it decays to lower values at each applied potential. Thick TiO_2 acts as an insulating layer, impeding the transfer of holes to the electrolyte, independent of the superior kinetics of sulfite oxidation. Therefore, the holes accumulate at the surface and the photocurrent can not saturate. Also, we observe a cathodic overshoot when the light is turned off, which is also evidence for hole accumulation at the surface.

We also carried out LSV measurements in the scavenger solution to assess the activity of the photoanodes in the absence of any kinetic limitation at the surface (Figure A1.11). With the deposition of 1.3 nm TiO_2, the photocurrent density increased while it decreased dramatically for $BiVO_4$/5.8 nm TiO_2, demonstrating a similar trend with the water oxidation activity. To assess the origin of the effect of TiO_2 overlayer on $BiVO_4$ activity, we calculated the charge injection (η_{inj}) and charge separation (η_{sep}) efficiencies for the photoanodes. The details for the calculations can be found in the Supporting Information. As shown in Figure 3.3, the η_{inj} decreases for both $BiVO_4$/1.3 nm TiO_2 and $BiVO_4$/5.8 nm TiO_2 within the whole potential regime. As this parameter is related to the water oxidation kinetics at the surface, 1.3 nm TiO_2 overlayer does not improve this efficiency since it does not act as a cocatalyst. The efficiency decreases even further with 5.8 nm TiO_2 as the charge transfer resistance is extensively increased with this modification. However, a significant increase in η_{sep} is observed for $BiVO_4$/1.3 nm TiO_2. This result confirms that the optimum thickness of TiO_2 increases band bending by passivating V^{5+}/V^{4+} surface states thus improving charge separation. Even though charge separation increases for $BiVO_4$/5.8 nm TiO_2 photoanode, according to TPC measurements given in Figure 3.2, we observe that the charge separation efficiency decreases in Figure 3.3. Since 5.8 nm TiO_2 decreases the photocurrent in scavenger solution by increasing the charge transfer resistance at the surface, we observe a decrease in η_{sep} values.

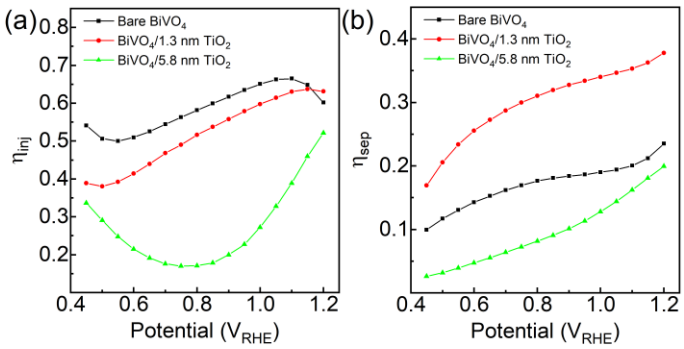

Figure 3.3. (a) Charge injection and (b) charge separation efficiencies for bare $BiVO_4$, $BiVO_4$/1.3 nm TiO_2, and $BiVO_4$/5.8 nm TiO_2.

The difference in the photocurrent of $BiVO_4$ under back and front illumination is generally attributed to the poor electron transport of the semiconductor. It is demonstrated that electron transport can be improved as a result of enhanced electronic conductivity by the incorporation of an n-type dopant, such as Mo or W[117,118]. Similarly, we propose that the passivation of the electron trapping process at the $BiVO_4$ surface enhances the electronic photoconductivity in the space-charge region. The electrons that are trapped at bare $BiVO_4$ surface can be utilized and contribute to the n-type conductivity of the material in $BiVO_4$/1.3 nm TiO_2 photoanodes. Therefore, the photocurrent increase with the TiO_2 deposition under front illumination is higher than of back illumination.

We have also conducted transient photovoltage measurements using short-light pulses to determine the effect of the electron trapping/de-trapping process at the surface on the Fermi level of the photoanodes. For a typical photovoltage measurement, as the photoanode is illuminated, the electrons are photoexcited to the conduction band of the semiconductor, generating electron-hole pairs. The accumulation of the majority carriers results in a decrease in the open-circuit potential (OCP). When the light source is turned off the electrons recombine with the photogenerated holes in the valence band and the holes that are accumulated at the $BiVO_4$ surface, thus the open-circuit potential increases[119]. Interestingly, for bare $BiVO_4$ we observe that the OCP momentarily goes to more positive values as the light is turned on, as shown in Figure 3.4a inset and when the light is turned off, OCP builds up. This process is attributed to the electron trapping/de-trapping phenomenon at the $BiVO_4$ surface[114]. When the light is turned on, the photogenerated electrons get trapped at the

surface states. As these electrons are now lost from the bulk, we observe an infinitesimal decay in the OCP. Similarly, as we turn the light off the surface trapped electrons de-trap and move towards the bulk. These electrons increase the Fermi level of $BiVO_4$, as we observe that OCP decreases[120]. This result also supports our hypothesis that photogenerated electron trapping at the $BiVO_4$ surface is a spontaneous process, which is independent of the applied potential.

3.

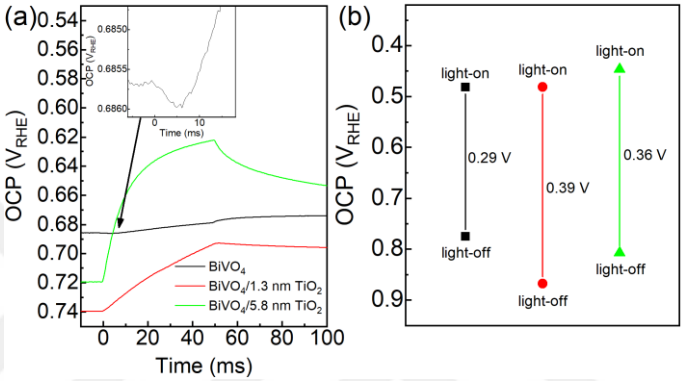

Figure 3.4. (a) TPV measurements done with 50.0 ms white light LED pulse (inset shows zoomed-in OCP change for bare $BiVO_4$ when the light is turned on). (b) The OCP measurement under dark and illumination with 1.0 Sun AM1.5G in 0.1 M KPi solution.

For the $BiVO_4$/1.3 nm TiO_2 photoanode, we do not observe these features, as the OCP decreases when the light is turned on and it increases when the light is turned off. This is consistent with the TPC results since TiO_2 overlayer passivates the surface states thus we do not observe the trapping/de-trapping behavior. Also, the OCP build-up occurs much faster for this photoanode. This can be related to a decrease in electron trapping and charge recombination at the surface. As the light is turned on, the electrons are excited to the conduction band. However, simultaneously charge recombination occurs which impedes the OCP build-up. Since TiO_2 at the surface decreases this recombination factor, OCP can decrease under illumination much faster. This effect is more apparent for the 5.8 nm TiO_2 overlayer as the surface recombination is suppressed even more. Furthermore, we performed the OCP measurements under steady-state conditions to investigate the role of the surface states on the photovoltage values of the photoanodes. As shown in Figure 3.4b, the photovoltage for bare $BiVO_4$ is 0.29 V_{RHE} whereas it is 0.39 V_{RHE} for $BiVO_4$/1.3 nm TiO_2.

Notice that the OCP values are the same for both photoanodes under illumination, and the deviation in the photovoltage results from the different Fermi levels in the absence of illumination. When the photoanode is immersed in the electrolyte the Fermi level of the semiconductor equilibrates with the potential of the redox couple present in the electrolyte[121]. Ideally, the OCP in the absence of illumination should be equal to 1.23 V_{RHE}, as the redox couple in the electrolyte is O_2/H_2O[19]. For bare $BiVO_4$ the OCP value is at around 0.8 V_{RHE} whereas it is closer to 1.23 V_{RHE} for $BiVO_4$/1.3 nm TiO_2. We attribute this feature to the high concentration of surface states present in the bare $BiVO_4$, as these surface states may result in Fermi level pinning resulting in an offset between the Fermi level of the photoanode and the electrochemical potential of the redox couple in the electrolyte[122]. Moreover, the pinned position of the Fermi level coincides with the maximum electron-trapping potential, which is 0.8 V_{RHE} as shown in Figure 3.2a. Thus, it can be suggested that both of these observations are related to the same surface state, namely V^{5+}/V^{4+}. It is also shown that the presence of surface states and Fermi level pinning can result in an anodic shift in the onset potential[123]. Thus, the 0.1 V_{RHE} cathodic shift observed with the TiO_2 overlayer shown in Figure 3.1a can be also attributed to the surface state passivation. The Fermi level unpinning can facilitate band bending at more cathodic potentials, hence the onset potential can also shift cathodically. For $BiVO_4$/5.8 nm TiO_2, the OCP at dark does not reach the same value as $BiVO_4$/1.3 nm. The surface state is diminished in this photoanode, however, the increased charge transfer resistance at the surface hinders the electron flow from $BiVO_4$ to the electrolyte, thus the dark OCP does not become closer to 1.23 V_{RHE}. Under illumination, the OCP reaches higher values than the other photoanodes because of the decreased surface recombination. As a result, the photovoltage achieved for this photoanode is 0.36 V, however, it is not utilized efficiently because of the insulating effect of 5.8 nm TiO_2.

To elucidate the effect of the TiO_2 overlayer on the charge transfer at the semiconductor/electrolyte interface, we performed EIS measurements in the potential range of 0.45-1.00 V_{RHE}. Figure 3.5 demonstrates the variation of the charge transfer resistance (R_{ct}) and capacitance (C_{int}) at the interface as a function of applied potential to the photoanode. The details of the calculation and the Nyquist plot fittings are given in Figure A1.12. For all of the photoanodes, the R_{ct} decreases with the applied potential. The R_{ct} values

for bare $BiVO_4$ and $BiVO_4$/1.3 nm TiO_2 are very similar at potentials between 0.45 and 0.55 V_{RHE}. Only at potentials higher than 0.60 V_{RHE} the charge transfer resistance significantly decreases with TiO_2 overlayer. Such behavior is correlated with the passivation of surface states. At potentials higher than 0.60 V_{RHE} the extent of electron trapping is much more significant than that at lower potentials, as shown in the TPC measurements in Figure 3.2. Since TiO_2 passivates the electron trapping/de-trapping process, the improvement in the charge transfer resistance due to the overlayer is more profound in this potential regime. For $BiVO_4$/5.8 nm TiO_2 the charge transfer resistance is higher than the other photoanodes, since thick TiO_2 acts as an insulating material and confirming the hindrance of the transfer of charges for water oxidation. Figure 3.5b shows the capacitance development at the semiconductor/electrolyte interface with applied potential. For bare $BiVO_4$, the capacitive build-up is present at between 0.7-0.8 V_{RHE} whereas this feature is not present for $BiVO_4$/1.3 nm TiO_2 photoanode as C_{int} vs. V_{RHE} at this regime is almost linear. The increase in the capacitance is related to the electrochemical conversion of V^{4+} to V^{5+} surface states. The capacitive build-up is smoothened via TiO_2 overlayer as a result of the passivation of the surface states. This effect is even more apparent for the 5.8 nm TiO_2 overlayer, as the capacitance with respect to potential seems nearly flat. However, overall the capacitance values do not change significantly with the TiO_2 overlayer. Thus, the agreement with the ECSA measurements based on capacitive buildup is profound.

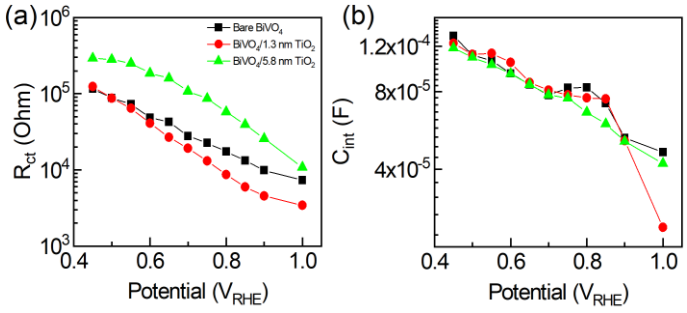

4.

Figure 3.5. Fitting parameters for EIS measurement as a function of applied potential in 0.1 M KPi buffer. (a) R_{ct} and (b) C_{int}.

Mott-Schottky plots for the photoanodes are presented in Figure 3.6. The Mott-Schottky technique can be utilized to estimate the dopant density and the flat-band potential of the

photoanode. As shown in Figure 3.6a, the C_s^{-2} vs potential plot has a positive slope, which confirms the n-type behavior of $BiVO_4$. The Mott-Schottky equation is given below[124]:

$$C_S^{-2} = \frac{2}{\varepsilon_0 \varepsilon_r A^2 e N_D}\left(V - V_{FB} - \frac{k_B T}{e}\right) \qquad \text{Equation 3.1}$$

where C_s is the capacitance at the space-charge layer, ε_0 is vacuum permittivity, ε_r is the relative permittivity of the material, A is the surface area, e is the charge of an electron, N_D is the dopant density, V is the applied potential, V_{FB} is the flat-band potential, k_B is the Boltzmann constant, and T is the absolute temperature. The slope of the plot decreases with the deposition of the 1.3 nm TiO_2 overlayer. This indicates that an increase in N_D for this photoanode, relative to the bare $BiVO_4$. Usually, this type of effect is observed when the photoanode is n-doped with an atom with a higher number of valence electrons, such as W or Mo for $BiVO_4$[125,126]. However[64], the TiO_2 overlayer is not expected to act as an electron donor. It is known that the Mott-Schottky equation makes assumptions that do not necessarily hold for nanostructured photoanode materials for water oxidation, such as ignoring the presence of surface states[127]. Surface states can impede the band bending due to Fermi level pinning. Thus, the dopant atoms can not fully ionize, and the capacitance in the space charge layer can not reach its actual value. By modifying the surface with the TiO_2 overlayer, we can diminish this surface state which inhibits the electron flow from the donor atoms to the electrolyte. Therefore, the band bending for this photoanode increases. The extent of band bending does not change much for the higher TiO_2 thickness.

5.

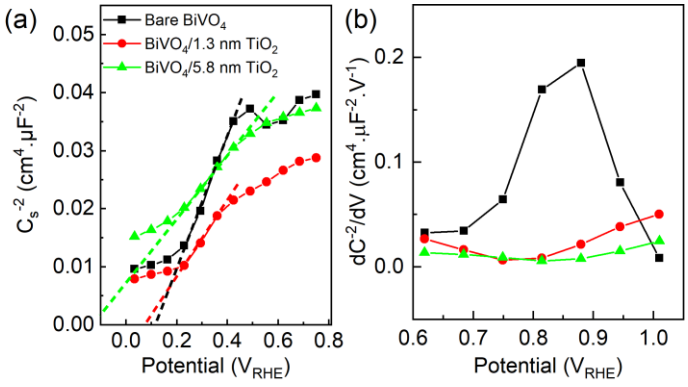

Figure 3.6. (a) Mott-Schottky plots for bare $BiVO_4$, $BiVO_4$/1.3 nm TiO_2, and $BiVO_4$/5.8 nm TiO_2 at 1 kHz in 0.1 M KPi buffer. (b) Derivative of Mott-Schottky plots within the potential range between 0.6 and 1.0 V_{RHE}.

Derivative of the Mott-Schottky plots within between 0.6 and 1.0 V_{RHE} presented in Figure 3.6b further justifies that the TiO_2 overlayer eliminates the trapping at V^{5+}/V^{4+} surface states. The broad peak present in this potential regime for bare $BiVO_4$ arises due to the presence of the surface states and its magnitude is proportional to the density of the surface states and also correlates with the degree of Fermi level pinning. For the 1.3 nm TiO_2 overlayer, elimination of the surface states is apparent, almost no surface state is evidenced for the 5.8 nm TiO_2 overlayer, which are all in full agreement with the TPC and EIS findings.

3.4.Conclusions

In this work, we showed that deposition of an ultrathin layer of TiO_2 on nanoporous $BiVO_4$ by ALD can enhance the water oxidation activity of $BiVO_4$ significantly. EIS results show that charge transfer resistance decreases when the optimum amount of TiO_2 is deposited on $BiVO_4$. Transient photocurrent and transient photovoltage results demonstrate that ultrathin TiO_2 overlayer suppresses photogenerated electron trapping at the surface states. The improvement of the water oxidation photocurrent is attributed to the enhancement of band bending, and the passivation of surface states. At higher TiO_2 overlayer thickness photogenerated electron trapping process is completely diminished, however the charge transfer resistance at the photoanode surface increases too much, which leads to diminished photocurrent for water oxidation. This trade-off dictates that the thickness of the overlayer needs to be optimized for the best photoactivity. These findings show that the limiting factor in the $BiVO_4$ activity is mainly the charge recombination at the surface and it can be overcome by modification with ultrathin TiO_2 overlayer to improve the charge carrier utilization, rather than the surface catalysis.

Chapter 4. Understanding the Role of Surface States in the $CuBi_2O_4$ Photocathodes

4.1 Introduction

PEC water splitting cells require photoelectrodes which can drive HER and OER in an efficient manner. Metal oxide based photoelectrodes were extensively studied which can drive OER, since it is suggested that 4 electron transfer in OER is the limiting factor for water splitting[128]. Even though that is the case, highly efficient and stable photocathodes must be designed to maximize the STH (solar-to-hydrogen) efficiency of the overall process.

$CuBi_2O_4$ is a p-type semiconductor, which is among the materials that can drive HER. It is considered as one of the most promising candidates, because its intrinsic properties which were listed in Section 1.5.1. It has a maximum theoretical photocurrent density of ~13 $mA.cm^{-2}$ [129]. However, the obtained photocurrent densities for this material are nowhere near this value, even when using electron scavengers. Berglund et. al. suggested that the limitation factors for the activity of $CuBi_2O_4$ are poor hole transport[6].

It is also known that $CuBi_2O_4$ suffers significantly from photocorrosion, particularly photogenerated electrons reducing the surface Cu^{2+} species into Cu^{1+} and Cu[130–132]. Such reduction mechanisms are suggested to deactivate the material, resulting in a decay of photocurrent under static potential and illumination conditions. However, Oropeza et. al. suggested that reduced Cu species as a result of irradiation can act as a homojunction, enhancing the charge separation properties[133]. Zhang and co-workers previously suggested $CuBi_2O_4$ suffers from Fermi level pinning due to high number of surface-states near the flat-band potential, which were attributed to surface defects[134]. Therefore, it can be said that there may be multiple effects of photogenerated electrons on the $CuBi_2O_4$ activity.

In this study, we study the role of photogenerated electron trapping at the $CuBi_2O_4$ in a systematic manner, as a function of applied potential. We show that near the flat-band potential, $CuBi_2O_4$ suffers from extensive electron trapping, which inhibits the charge transfer. We aimed to passivate this process by utilizing an ultrathin TiO_2 overlayer, similar to the strategy in the previous chapter.

4.2 Experimental Procedure

The $CuBi_2O_4$ photocathodes were synthesized as described in Section 2.1.1.2. The PEC set-up used to carry out the experiments was also explained in Section 2.2.1. The used electrolyte was 0.1 M NaOH (pH= 12.8) which was purged with either N_2 or O_2 for 30 minutes. N_2 was used to degas the electrolyte, whereas O_2 was used as an electron scavenger. Electrolyte was purged during the LSV measurements while stirring, in order to remove the produced O_2 at the counter electrode (N_2-purge), or to maintain the dissolved O_2 in the electrolyte (O_2-purge). The sweep rate for the LSV measurements was 10 $mV.s^{-1}$, and the mechanical chopper frequency was set as 0.2 Hz. The EIS measurements were carried out in the range of 1.4 V_{RHE}-0.4 V_{RHE}, with frequencies between 100 kHz to 100 mHz, with a 10 mV potential signal amplitude. The structural characterizations such as XPS, Raman, XRD, UV-vis-NIR, and FESEM were also described in Section 2.3.

4.3 Results and Discussion

Figure 4.1. below shows the XPS spectra of Bi 4f, Cu 2p, O 1s, and Cu LMM Auger spectra for the $CuBi_2O_4$ photocathode. Bi $4f_{7/2}$ peak located at 159.0 eV indicates presence of Bi^{3+} state, and the Cu 2p spectra shows 2+ valency for Cu, judging from the strong shake-up satellite peak[135], which are consistent with the previous studies on $CuBi_2O_4$[55,136]. O 1s spectra shows multiple features, which are a peak at 529.9 eV, which can be attributed to lattice O^{2-}, and a strong high binding energy shoulder at 531.4 eV due to surface -OH species. Cu LMM Auger spectra shows a peak at 917.4 eV, which can be attributed to Cu^{2+}, consistent with the Cu 2p XPS spectra[137,138].

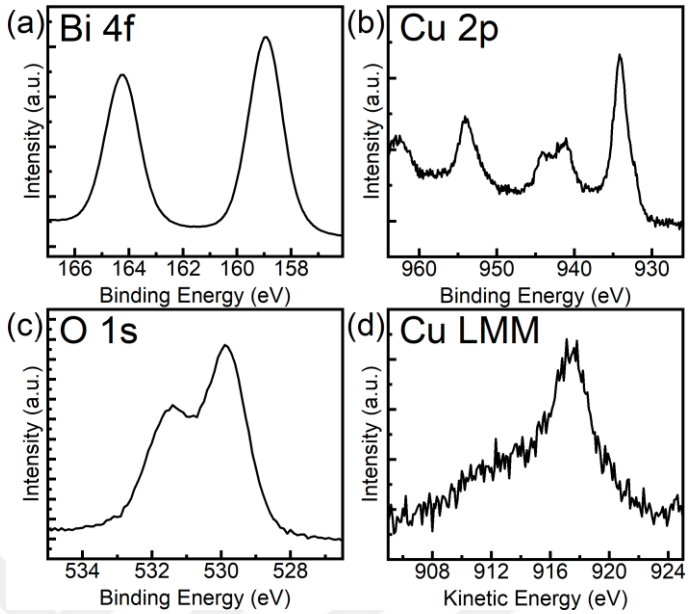

Figure 4.1. X-ray photoelectron spectras of (a) Bi 4f, (b) Cu 2p, (c) O 1s, and Auger spectra of Cu LMM for $CuBi_2O_4$.

Raman spectroscopy was utilized to confirm the phase of $CuBi_2O_4$ as shown in Figure 4.2. below. The high intensity peak located at 129 cm^{-1} corresponds to the translational vibration of CuO_4 plane along the c axis with A_{1g} mode. The small peak at 188 cm^{-1} corresponds to E_g mode of Cu-Cu vibration. The feature at 259 cm^{-1} was assigned to rotational vibrational mode of CuO_4 planes in the opposite direction with A_{1g} mode, and the peak at 583 cm^{-1} was assigned to the A_{1g} mode of in-plane breathing of the CuO_4 planes. The peak at 400 cm^{-1} corresponds to the A_{1g} mode of Bi-O bond stretching[139,140]. No additional peaks were observed for phases other than $CuBi_2O_4$.

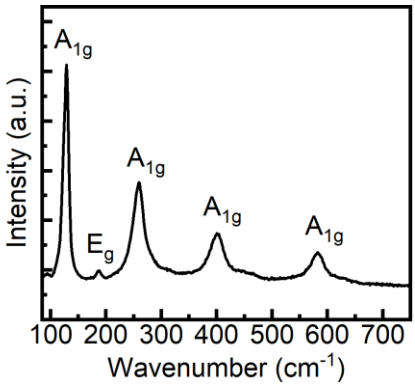

Figure 4.2. Raman spectra of $CuBi_2O_4$.

X-ray diffraction pattern is given in Figure 4.3. below. The assigned crystal planes for $CuBi_2O_4$ are also indicated in the figure, which confirms the $CuBi_2O_4$ phase. However, we observe a peak corresponding to Bi_2O_3 phase at 31.76°, suggesting that the $CuBi_2O_4$ films are not phase pure. The inconsistency with the Raman spectra may be due to the small spot size of the laser used in Raman (40 μm) and slightly inhomogeneous sample. While achieving pure phase is important to evaluate the materials photoelectrochemical properties, given that the small amount of Bi_2O_3 phase, and the fact that Bi_2O_3 does not exhibit HER activity, we do not expect to observe a significant effect.

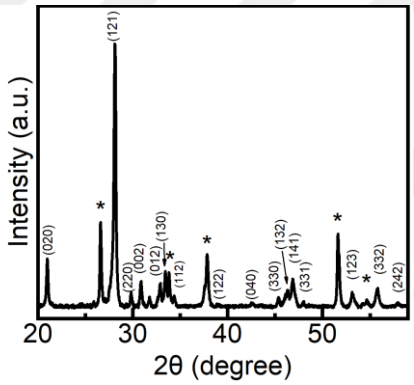

Figure 4.3. Powder XRD pattern of $CuBi_2O_4$. The diffraction peaks from the FTO substrate are indicated with an asterisk (*) sign. The signals from $CuBi_2O_4$ crystal planes are referenced to COD 1539608.

In order to evaluate the optical properties of $CuBi_2O_4$ films, UV-vis-NIR and Tauc analysis were performed, which are given in Figure 4.4. below. Figure 4.4.(a) shows the absorbance, which shows a slow increase in the absorbance with decreasing wavelength, as a result of its indirect band gap and low absorption coefficient[55]. The Tauc analysis in Figure 4.4.(b) indicates an indirect band gap of 1.8 eV, consistent with the previous reports for this material[141,142].

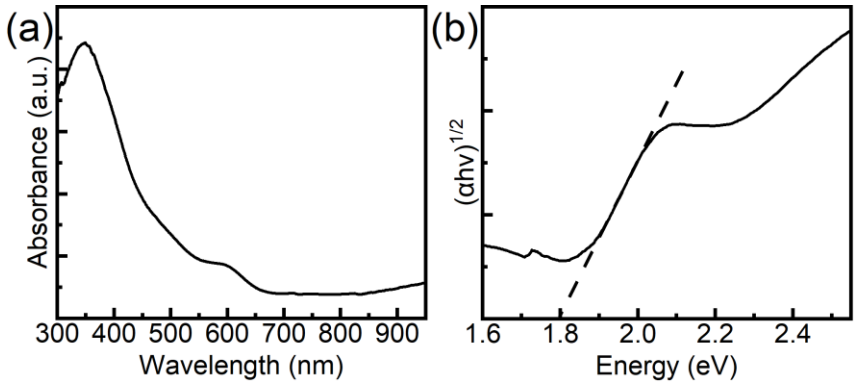

Figure 4.4. (a)UV-vis-NIR absorbance spectra, and (b) Tauc analysis for $CuBi_2O_4$ films.

FESEM images shown in Figure 4.5. exhibits highly nanoporous morphology. This feature of the electrodeposited $CuBi_2O_4$ enables high surface area for charge transfer to occur, while also enhancing charge transport[143].

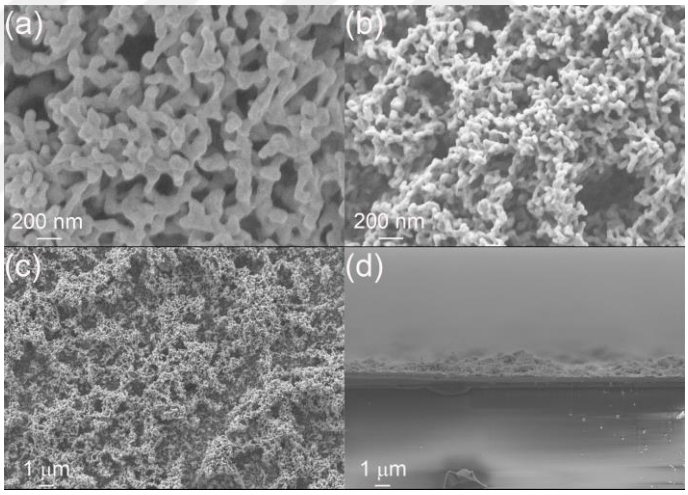

Figure 4.5. FESEM images for $CuBi_2O_4$ with different magnifications, (a), (b), (c) from on top, and (d) from cross-section.

In order to evaluate the PEC activity of $CuBi_2O_4$ photocathodes, we performed LSV measurements with chopped illumination in the presence of O_2 gas in the electrolyte, as shown in Figure 4.6. below. Photocurrent under back illumination shows ~-0.4 $mA.cm^{-2}$, whereas under front illumination it is ~-0.2 $mA.cm^{-2}$ at 0.5 V_{RHE}. Such significant difference in front and back illumination in photocurrent is common in photoelectrodes, which is indicative of poor charge transport properties. $CuBi_2O_4$ is known to suffer from poor hole transport properties, which is consistent with our LSV results[6]. The potential regime of 1.4 V_{RHE}-1.0 V_{RHE} the observed photocurrent is very low (around -0.01 $mA.cm^{-2}$). Interestingly,

in this potential regime the photocurrent under front and back illumination are very similar, suggesting there are other limitations than the charge transport for this material.

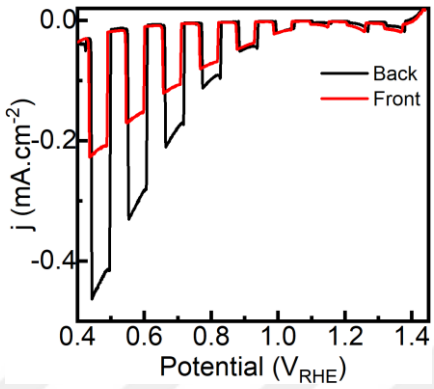

Figure 4.6. LSV measurements for $CuBi_2O_4$ under front and back illumination in 0.1 M NaOH solution (pH=12.8) with O_2 purging.

Figure 4.7. shows the Mott-Schottky analysis for $CuBi_2O_4$. The negative slope of the linear fit line confirms the p-type character. The flat-band potential can be determined from the intercept of the potential axis, which is 1.3 V_{RHE}, that is consistent with the previous reports[6,56].

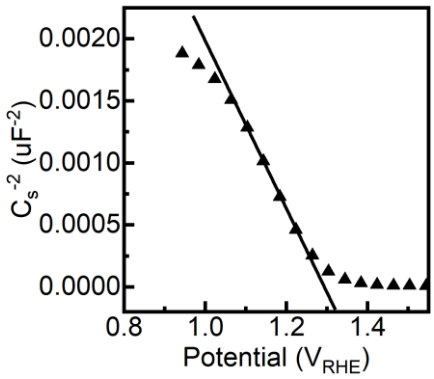

Figure 4.7. Mott-Schottky measurement for $CuBi_2O_4$ done in 0.1 M NaOH (pH=12.8) without illumination.

To assess the stability of the $CuBi_2O_4$ photocathodes, CA measurements were carried out as shown in Figure 4.8. In the N_2-purged electrolyte where there is no electron scavenger, the photocurrent decays rapidly, which goes from -0.15 $mA.cm^{-2}$ to -0.02 $mA.cm^{-2}$ in only 10 minutes. This indicates severe photocorrosion and deactivation for this material. In the

presence of O_2 in the electrolyte however, the photocurrent is relatively more stable. Since O_2 reduction kinetics is more facile than of HER kinetics, photogenerated electrons can react with less photogenerated electron accumulation and result in less photocorrosion. However, the decay in the photocurrent in the presence of O_2 indicate that there is still photocorrosion, since O_2 can not capture all of the electrons reaching to the surface, which is also evident from the transient spikes in the LSV measurements given in Figure 4.6.

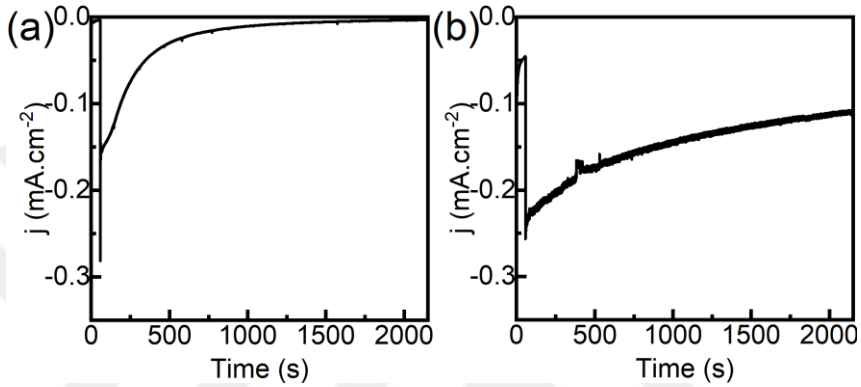

Figure 4.8. Chronoamperometry (CA) measurement under front illumination at 0.5 V_{RHE} in 0.1 M NaOH (pH=12.8) with (a) N_2-purged, and (b) O_2-purged electrolyte.

In order to assess the charge transfer resistance and the capacitive behavior of the $CuBi_2O_4$ photocathodes, EIS analysis was performed under illumination. An equivalent circuit with 2 RC elements were used to fit the Nyquist plots, which is a commonly used circuit to model PEC systems when surface-states are present[120,144,145]. The equivalent circuit is given as an inset in Figure 4.9.(a). R_{series} correspond to the resistance due to the electrolyte, and the external connections in the electrochemical cell. R_{bulk} and C_{bulk} are the resistance and the capacitance associated with the bulk of the semiconductor. $R_{surface\text{-}state}$ and $C_{surface\text{-}state}$ are are the resistance and the capacitance associated with charge carrier trapping at the surface-states. The Nyquist plot is given in the Appendix B. The $R_{surface\text{-}state}$ as shown in Figure 4.9.(a) increases from 1.4 V_{RHE} to 1.2 V_{RHE}, and then starts to decrease with increasing cathodic potential. The resistance is lower after 1.0 V_{RHE}, where it steadily decreases with increasing cathodic potential. This result is consistent with the LSV measurement given in Figure 4.6. as in the potential region of 1.4 V_{RHE}-1.0 V_{RHE} there is no significant photocurrent. Only after 1.0 V_{RHE} the photocurrent shows a take-off. The $C_{surface\text{-}state}$ also shows a peaking type of behavior in the 1.4 V_{RHE}-1.0 V_{RHE} region, going through a minimum at 1.0 V_{RHE}. After

this potential it increases steadily. This result suggests that there is significant amount of surface-states which are near the flat-band potential of $CuBi_2O_4$.

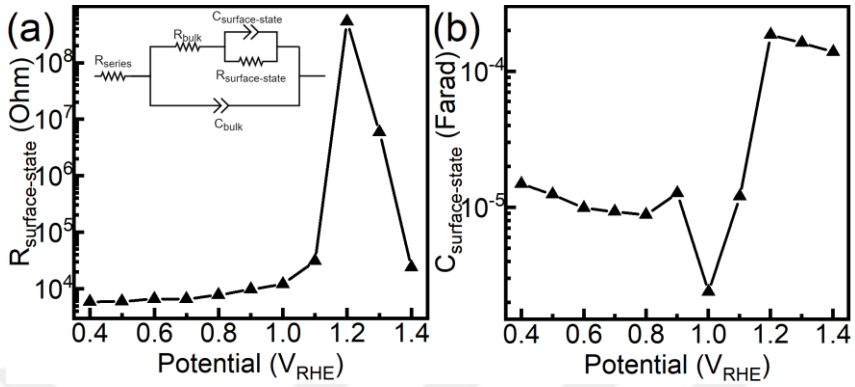

Figure 4.9. Electrochemical impedance spectroscopy (EIS) fitting results of $CuBi_2O_4$ for (a) Resistance due to the surface-states ($R_{surface-state}$), and (b) Capacitance due to the surface-states ($C_{surface-state}$)

TPC measurements using short LED pulses were also carried out, as shown in Figure 4.10.(a) below. The pulse width was set as 500.0 ms to record the full photocurrent response of $CuBi_2O_4$. When the light is turned on at t=0.0 ms, the photogenerated electrons migrate to the surface, resulting in an increase in cathodic current. At the potentials of 1.4 V_{RHE}-1.3 V_{RHE}, we do not observe significant electron accumulation at the surface, as there are no sharp transient spikes. In fact, the response of the photocathode is slow, such that the time to reach the maximum photocurrent in these potentials are ~120 ms. Such behavior is an indication of Fermi level pinning. As the potential drop across the space charge layer is limited in this condition, charges cannot be separated effectively, and the photocurrent in the light-on moment does not reach to higher values. The slow response is an indication of photogenerated electron trapping at a state which is close to the valence band. At higher potentials of 1.2 V_{RHE}-0.9 V_{RHE} the charges separate more efficiently, as we observe a cathodic spike as a result of photogenerated electron accumulation. However, even after 500.0 ms, the photocurrent does not decay to a steady-state value, which suggests there is extensive electron accumulation at the $CuBi_2O_4$ surface. We note that the Mott-Schottky results given in Figure 4.7. is consistent with these result, as at 1.4 V_{RHE}-1.3 V_{RHE} C_s^{-2} does not change much, however at 1.2 V_{RHE}-0.9 V_{RHE} C_s^{-2} linearly increases, indicating band bending. At higher cathodic potentials, we do not observe transient spikes, which indicates

that all of the photogenerated electrons that reach to the surface take place in oxygen reduction reaction.

When the light is turned off at t=500.0 ms the photogenerated electrons recombine with the valence band holes. Interestingly, we do not observe an anodic overshoot, which is expected as a result of electron accumulation at the $CuBi_2O_4$ surface. Instead, the photocurrent decays slowly to zero. The rate of the decay can be informative in regard to charge carrier dynamics, particularly on the trapping and/or detrapping processes. The slow decay of photocurrent can be associated with charge carrier detrapping as a result of localization[146]. The transients are fitted with a bi-exponential decay function, given below as Equation 4.1.

$$j\,(t) = j_0 + e^{-\frac{t}{\tau_1}} + e^{-\frac{t}{\tau_2}} \qquad \text{Equation 4.1}$$

Where j(t) is the recorded current after the light is turned off, j_0 is the background current, τ_1 and τ_2 are the time constants. The fittings are given in Figure 4.10.(b), and the extracted time constant values are given in Figure 4.10.(c). Interestingly, τ_1 does not change much across the whole potential range, whereas τ_2 shows a different trend. Thus, τ_1 is attributed to the recombination of the photogenerated electrons that are delocalized in the conduction band in the surface region, which recombines faster. The value of this time constant is around ~2.0 ms, which is denoted as $\tau_{\text{conduction band}}$. The other time constant, τ_2 is ~58.0 ms at 1.4 V_{RHE}, and it decreases steadily until 1.0 V_{RHE}-0.9 V_{RHE} where it shows a minima of 24 ms. This behavior coincides with the EIS measurements given in Figure 4.9. as $CuBi_2O_4$ shows high surface-state capacitance and resistance in this potential regime as well. These surface-states can act as electron traps at the surface, in which the trapped electron is unable to be transferred to the electrolyte, which may also lead to photocorrosion. However, the surface-states can be also reaction intermediates, in which their build-up at the surface facilitates the reaction[89]. As shown in the LSV measurement, the photocurrent starts to increase below 1.0 V_{RHE}. The $C_{\text{surface-state}}$ and the time constant for the TPC decays go through a minima right at this potential. For the surface intermediates for the reaction products, the decrease in the capacitance should coincide with the photocurrent take-off, which would indicate intermediate species reacting further to turn into products[147]. However, since the capacitance goes through a minima before the photocurrent take-off, we assign this as a recombination state which acts as an electron trap in the surface.

At more cathodic potentials than 0.9 V_{RHE}, the photocurrent increases as shown in the LSV measurement, as well as the $C_{surface\text{-}state}$, and the recombination time constant, shown in Figure 4.10.(c). It was suggested that $CuBi_2O_4$ suffers from photocorrosion, as shown in Figure 4.8. under reaction conditions where there is photocurrent. Therefore, we attribute this behavior to photogenerated electron trapping at the surface Cu^{2+} species, which in turn reduces to Cu^{+} and/or Cu^{0}. We also note that trapping (or photocorrosion) is more significant with increasing potential, which severely affects the stability of $CuBi_2O_4$ photocathodes.

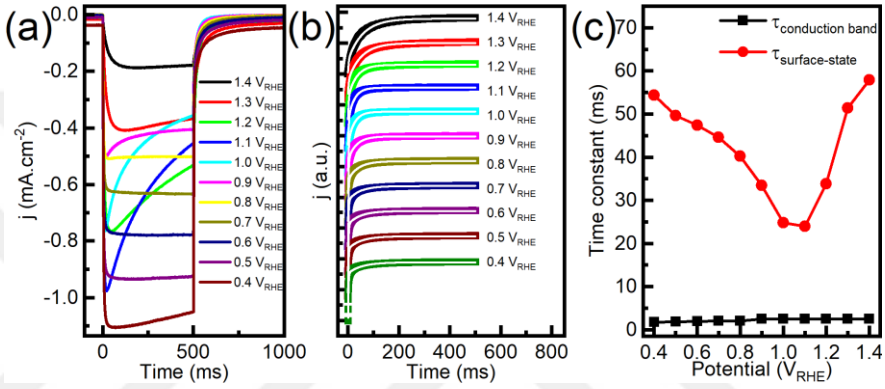

Figure 4.10. (a) TPC measurement done in O_2-purged 0.1 M NaOH (pH=12.8) with 500.0 ms white LED pulse under front illumination (b) normalized photocurrent decay (symbols), and fittings with bi-exponential decay function (white lines), which were offset for clarity, and (c) the calculated time constants for the exponential decays.

Our results indicate that the photogenerated electron trapping process has two detrimental effects, which are (i) leading to late photocurrent onset potential, and (ii) facilitating photocorrosion. In order to remove these limiting factors for the $CuBi_2O_4$ activity, we have modified the $CuBi_2O_4$ with various thicknesses of TiO_2 overlayer. In the previous Chapter we have shown that TiO_2 overlayer can passivate photogenerated electron trapping process at surface-states, to enhance the water oxidation activity of $BiVO_4$[148] which indicates that a similar strategy may work for $CuBi_2O_4$ as well. Also TiO_2 is widely utilized for various photocathodes such as p-Si, Cu_2O, and $CuBi_2O_4$ to inhibit photocorrosion and enhance their stability[149–151]. However, as shown in Figure 4.11. below, various TiO_2 overlayer thicknesses significantly decrease the photocurrent of $CuBi_2O_4$. The photocurrent decreases with increasing thickness of TiO_2. Even with the modification of 2 cycles of TiO_2, which is very low coverage, the photocurrent decreases from -0.27 $mA.cm^{-2}$ to -0.01 $mA.cm^{-2}$. Such effect of TiO_2 overlayer on bare $CuBi_2O_4$ was also reported previously in the

literature[63]. This result may be due to the improper interface formation between the $CuBi_2O_4$ and TiO_2 layers, which can increase the charge recombination. The XPS spectra for Bi 4f, Cu 2p, O 1s, and Ti 2p shows the growth of TiO_2 overlayer, which is given in the Appendix section.

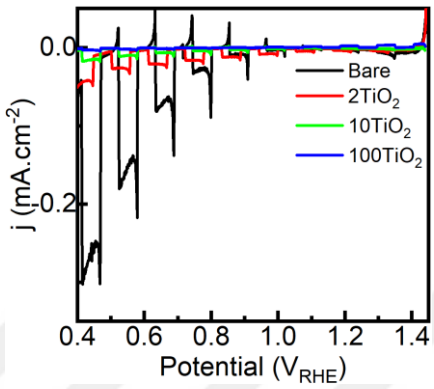

Figure 4.11. LSV measurement for $CuBi_2O_4$ and the effect of TiO_2 overlayer with various cycle numbers, under back illumination in 0.1 M NaOH solution (pH=12.8) with N_2 purging.

4.4.Conclusions

In this Chapter, we have synthesized $CuBi_2O_4$ photocathodes via electrodeposition method, and characterized the $CuBi_2O_4$ films using XPS, FESEM, XRD, UV-vis-NIR absorption, and Raman spectroscopy. The stability measurements indicate severe photocorrosion occurs, in which the photogenerated electrons reduce Cu^{2+} to Cu^{+} and/or Cu^{0}. Furthermore, the roles of the surface-states of $CuBi_2O_4$ were examined. We found that surface states near the flat-band potential act as photogenerated electron traps, which delays the photocurrent onset to 0.9 V_{RHE} -1.0 V_{RHE} even though photocurrent is observed as early as 1.4 V_{RHE}. The $CuBi_2O_4$ surface was modified with ALD grown TiO_2 with different thicknesses to passivate the electron trapping process. However, even with low coverage of TiO_2, $CuBi_2O_4$ activity significantly decreased. These results suggest that interfacial dynamics are important for the $CuBi_2O_4$ photocathode activity and stability. Thus, the surface charge carrier dynamics need to be tuned to passivate the electron trapping process to improve the performance of $CuBi_2O_4$.

Chapter 5. Summary and Conclusions

In the first part of this study, the effect of TiO_2 overlayer on $BiVO_4$ photoanodes for OER was investigated. We show that the water oxidation activity of $BiVO_4$ photoanode is significantly boosted by the TiO_2 overlayer prepared by ALD, with an optimized thickness. We attribute this enhancement to improved charge separation and suppression of surface recombination due to surface state passivation. We show with TPC measurements that TiO_2 overlayer can modulate the extent of the photogenerated electron-trapping process at the $BiVO_4$ surface. Even though the electron trapping process is eliminated completely at higher TiO_2 overlayer thicknesses, the charge transfer resistance across the interface also increases significantly, resulting in a diminished photocurrent.

In the second part, the roles of the surface-states were evaluated for the $CuBi_2O_4$ photocathode for HER. Using EIS and TPC measurements, we have identified the presence of surface-states, and photogenerated electron trapping process at these states. We show that surface-states near the flat-band potential act as photogenerated electron traps, which results in a delay in the photocurrent onset potential. The TiO_2 overlayer was grown on $CuBi_2O_4$ surface via ALD to tune the charge carrier dynamics at the surface and inhibit the electron trapping process with a similar strategy with $BiVO_4$ photoanodes. However, even with low coverage of TiO_2 overlayer, $CuBi_2O_4$ activity significantly decreased. Furthermore, we have identified significant photocorrosion, which is detrimental for the stability of the photocathode. These results suggest that interfacial dynamics are important for the $CuBi_2O_4$ photocathode activity and stability. Thus, the surface charge carrier dynamics need to be tuned by other materials than TiO_2 to passivate the electron trapping process to improve the performance of $CuBi_2O_4$.

Investigations done in this study shed light on the roles of the surface states in $BiVO_4$ and $CuBi_2O_4$ for PEC water splitting. As future works, the effect of the surface Cu composition will be investigated on the activity and the concentration of surface-states in $CuBi_2O_4$ photocathode. Furthermore, additional experiment can be designed to evidence charge carrier trapping for both $BiVO_4$ and $CuBi_2O_4$. LSV and TPC measurements can be done using a laser with sub-bandgap energy as the incident light, rather than an LED or a Xe lamp. Differential electrochemical mass spectrometry (DEMS) can be utilized to assess the effect of surface charge carrier dynamics on the reaction products, by coupling it with TPC

measurements. A tandem cell can be constructed using $BiVO_4/TiO_2$ photoanodes and $CuBi_2O_4$ photocathodes, and STH efficiency of the device can be assessed, by measuring H_2 and O_2 amounts with gas chromatography.

Chapter 6. References

(1) Hisatomi, T.; Kubota, J.; Domen, K. Recent Advances in Semiconductors for Photocatalytic and Photoelectrochemical Water Splitting. *Chem. Soc. Rev.* **2014**, *43* (22), 7520–7535. https://doi.org/10.1039/C3CS60378D.

(2) *Photoelectrochemical Hydrogen Production*; van de Krol, R., Grätzel, M., Eds.; Electronic Materials: Science & Technology; Springer US: Boston, MA, 2012; Vol. 102. https://doi.org/10.1007/978-1-4614-1380-6.

(3) Chen, Z.; Jaramillo, T. F.; Deutsch, T. G.; Kleiman-Shwarsctein, A.; Forman, A. J.; Gaillard, N.; Garland, R.; Takanabe, K.; Heske, C.; Sunkara, M.; McFarland, E. W.; Domen, K.; Miller, E. L.; Turner, J. A.; Dinh, H. N. Accelerating Materials Development for Photoelectrochemical Hydrogen Production: Standards for Methods, Definitions, and Reporting Protocols. *J. Mater. Res.* **2010**, *25* (1), 3–16. https://doi.org/10.1557/JMR.2010.0020.

(4) Chu, S.; Li, W.; Yan, Y.; Hamann, T.; Shih, I.; Wang, D.; Mi, Z. Roadmap on Solar Water Splitting: Current Status and Future Prospects. *Nano Futures* **2017**, *1* (2), 022001. https://doi.org/10.1088/2399-1984/aa88a1.

(5) Zhao, Z.; Li, Z.; Zou, Z. Electronic Structure and Optical Properties of Monoclinic Clinobisvanite BiVO4. *Phys. Chem. Chem. Phys.* **2011**, *13* (10), 4746. https://doi.org/10.1039/c0cp01871f.

(6) Berglund, S. P.; Abdi, F. F.; Bogdanoff, P.; Chemseddine, A.; Friedrich, D.; van de Krol, R. Comprehensive Evaluation of $CuBi_2O_4$ as a Photocathode Material for Photoelectrochemical Water Splitting. *Chem. Mater.* **2016**, *28* (12), 4231–4242. https://doi.org/10.1021/acs.chemmater.6b00830.

(7) Hu, H.; Dong, B.; Hu, H.; Chen, F.; Kong, M.; Zhang, Q.; Luo, T.; Zhao, L.; Guo, Z.; Li, J.; Xu, Z.; Wang, S.; Eder, D.; Wan, L. Atomic Layer Deposition of TiO2 for a High-Efficiency Hole-Blocking Layer in Hole-Conductor-Free Perovskite Solar Cells Processed in Ambient Air. *ACS Appl. Mater. Interfaces* **2016**, *8* (28), 17999–18007. https://doi.org/10.1021/acsami.6b02701.

(8) Seah, M. P.; Dench, W. A. Quantitative Electron Spectroscopy of Surfaces: A Standard Data Base for Electron Inelastic Mean Free Paths in Solids. *Surface and Interface Analysis* **1979**, *1* (1), 2–11. https://doi.org/10.1002/sia.740010103.

(9) X-Ray Photoelectron Spectroscopy. 262.

(10) Höök, M.; Tang, X. Depletion of Fossil Fuels and Anthropogenic Climate Change—A Review. *Energy Policy* **2013**, *52*, 797–809. https://doi.org/10.1016/j.enpol.2012.10.046.

(11) Chu, S.; Majumdar, A. Opportunities and Challenges for a Sustainable Energy Future. *Nature* **2012**, *488* (7411), 294–303. https://doi.org/10.1038/nature11475.

(12) Armor, J. N. The Multiple Roles for Catalysis in the Production of H2. *Applied Catalysis A: General* **1999**, *176* (2), 159–176. https://doi.org/10.1016/S0926-860X(98)00244-0.

(13) Kannan, N.; Vakeesan, D. Solar Energy for Future World: - A Review. *Renewable and Sustainable Energy Reviews* **2016**, *62*, 1092–1105. https://doi.org/10.1016/j.rser.2016.05.022.

(14) Qi, J.; Zhang, W.; Cao, R. Solar-to-Hydrogen Energy Conversion Based on Water Splitting. *Adv. Energy Mater.* **2018**, *8* (5), 1701620. https://doi.org/10.1002/aenm.201701620.

(15) Pregger, T.; Graf, D.; Krewitt, W.; Sattler, C.; Roeb, M.; Möller, S. Prospects of Solar Thermal Hydrogen Production Processes. *International Journal of Hydrogen Energy* **2009**, *34* (10), 4256–4267. https://doi.org/10.1016/j.ijhydene.2009.03.025.

(16) Cheng, W.-H.; de la Calle, A.; Atwater, H. A.; Stechel, E. B.; Xiang, C. Hydrogen from Sunlight and Water: A Side-by-Side Comparison between Photoelectrochemical and Solar Thermochemical Water-Splitting. *ACS Energy Lett.* **2021**, *6* (9), 3096–3113. https://doi.org/10.1021/acsenergylett.1c00758.

(17) Hisatomi, T.; Domen, K. Reaction Systems for Solar Hydrogen Production via Water Splitting with Particulate Semiconductor Photocatalysts. *Nat Catal* **2019**, *2* (5), 387–399. https://doi.org/10.1038/s41929-019-0242-6.

(18) Fujishima, A.; Honda, K. Electrochemical Photolysis of Water at a Semiconductor Electrode. *Nature* **1972**, *238* (5358), 37–38. https://doi.org/10.1038/238037a0.

(19) Walter, M. G.; Warren, E. L.; McKone, J. R.; Boettcher, S. W.; Mi, Q.; Santori, E. A.; Lewis, N. S. Solar Water Splitting Cells. *Chem. Rev.* **2010**, *110* (11), 6446–6473. https://doi.org/10.1021/cr1002326.

(20) Park, Y.; McDonald, K. J.; Choi, K.-S. Progress in Bismuth Vanadate Photoanodes for Use in Solar Water Oxidation. *Chem. Soc. Rev.* **2013**, *42* (6), 2321–2337. https://doi.org/10.1039/C2CS35260E.

(21) Parmar, K. P. S.; Kang, H. J.; Bist, A.; Dua, P.; Jang, J. S.; Lee, J. S. Photocatalytic and Photoelectrochemical Water Oxidation over Metal-Doped Monoclinic BiVO4 Photoanodes. *ChemSusChem* **2012**, *5* (10), 1926–1934. https://doi.org/10.1002/cssc.201200254.

(22) Liu, T.; Zhou, X.; Dupuis, M.; Li, C. The Nature of Photogenerated Charge Separation among Different Crystal Facets of BiVO4 Studied by Density Functional Theory. *Phys. Chem. Chem. Phys.* **2015**, *17* (36), 23503–23510. https://doi.org/10.1039/C5CP04299B.

(23) Yin, W.-J.; Wei, S.-H.; Al-Jassim, M. M.; Turner, J.; Yan, Y. Doping Properties of Monoclinic BiVO 4 Studied by First-Principles Density-Functional Theory. *Phys. Rev. B* **2011**, *83* (15), 155102. https://doi.org/10.1103/PhysRevB.83.155102.

(24) Seo, H.; Ping, Y.; Galli, G. Role of Point Defects in Enhancing the Conductivity of BiVO4. *Chem. Mater.* **2018**, *30* (21), 7793–7802. https://doi.org/10.1021/acs.chemmater.8b03201.

(25) Cooper, J. K.; Gul, S.; Toma, F. M.; Chen, L.; Glans, P.-A.; Guo, J.; Ager, J. W.; Yano, J.; Sharp, I. D. Electronic Structure of Monoclinic $BiVO_4$. *Chem. Mater.* **2014**, *26* (18), 5365–5373. https://doi.org/10.1021/cm5025074.

(26) Qin, D.-D.; Wang, T.; Song, Y.-M.; Tao, C.-L. Reduced Monoclinic BiVO 4 for Improved Photoelectrochemical Oxidation of Water under Visible Light. *Dalton Transactions* **2014**, *43* (21), 7691–7694. https://doi.org/10.1039/C3DT53575D.

(27) Chen, L.; Toma, F. M.; Cooper, J. K.; Lyon, A.; Lin, Y.; Sharp, I. D.; Ager, J. W. Mo-Doped BiVO4 Photoanodes Synthesized by Reactive Sputtering. *ChemSusChem* **2015**, *8* (6), 1066–1071. https://doi.org/10.1002/cssc.201402984.

(28) Abdi, F. F.; Firet, N.; van de Krol, R. Efficient BiVO4 Thin Film Photoanodes Modified with Cobalt Phosphate Catalyst and W-Doping. *ChemCatChem* **2013**, *5* (2), 490–496. https://doi.org/10.1002/cctc.201200472.

(29) Wang, G.; Ling, Y.; Lu, X.; Qian, F.; Tong, Y.; Zhang, J. Z.; Lordi, V.; Rocha Leao, C.; Li, Y. Computational and Photoelectrochemical Study of Hydrogenated Bismuth Vanadate. *J. Phys. Chem. C* **2013**, *117* (21), 10957–10964. https://doi.org/10.1021/jp401972h.

(30) Berglund, S. P.; Rettie, A. J. E.; Hoang, S.; Mullins, C. B. Incorporation of Mo and W into Nanostructured BiVO4 Films for Efficient Photoelectrochemical Water Oxidation. *Phys. Chem. Chem. Phys.* **2012**, *14* (19), 7065–7075. https://doi.org/10.1039/C2CP40807D.

(31) Kim, J. H.; Jang, J. W.; Kang, H. J.; Magesh, G.; Kim, J. Y.; Kim, J. H.; Lee, J.; Lee, J. S. Palladium Oxide as a Novel Oxygen Evolution Catalyst on BiVO4 Photoanode for Photoelectrochemical Water Splitting. *Journal of Catalysis* **2014**, *317*, 126–134. https://doi.org/10.1016/j.jcat.2014.06.015.

(32) Higashi, T.; Kaneko, H.; Minegishi, T.; Kobayashi, H.; Zhong, M.; Kuang, Y.; Hisatomi, T.; Katayama, M.; Takata, T.; Nishiyama, H.; Yamada, T.; Domen, K. Overall Water Splitting by Photoelectrochemical Cells Consisting of (ZnSe)0.85(CuIn0.7Ga0.3Se2)0.15 Photocathodes and BiVO4 Photoanodes. *Chem. Commun.* **2017**, *53* (85), 11674–11677. https://doi.org/10.1039/C7CC06637F.

(33) Zhu, Y.; Ren, J.; Yang, X.; Chang, G.; Bu, Y.; Wei, G.; Han, W.; Yang, D. Interface Engineering of 3D BiVO4/Fe-Based Layered Double Hydroxide Core/Shell Nanostructures for Boosting Photoelectrochemical Water Oxidation. *J. Mater. Chem. A* **2017**, *5* (20), 9952–9959. https://doi.org/10.1039/C7TA02179H.

(34) Kuang, Y.; Jia, Q.; Ma, G.; Hisatomi, T.; Minegishi, T.; Nishiyama, H.; Nakabayashi, M.; Shibata, N.; Yamada, T.; Kudo, A.; Domen, K. Ultrastable Low-Bias Water Splitting Photoanodes via Photocorrosion Inhibition and in Situ Catalyst Regeneration. *Nat Energy* **2016**, *2* (1), 1–9. https://doi.org/10.1038/nenergy.2016.191.

(35) Seabold, J. A.; Choi, K.-S. Efficient and Stable Photo-Oxidation of Water by a Bismuth Vanadate Photoanode Coupled with an Iron Oxyhydroxide Oxygen

Evolution Catalyst. *J. Am. Chem. Soc.* **2012**, *134* (4), 2186–2192. https://doi.org/10.1021/ja209001d.

(36) Abdi, F. F.; Han, L.; Smets, A. H. M.; Zeman, M.; Dam, B.; van de Krol, R. Efficient Solar Water Splitting by Enhanced Charge Separation in a Bismuth Vanadate-Silicon Tandem Photoelectrode. *Nat Commun* **2013**, *4* (1), 2195. https://doi.org/10.1038/ncomms3195.

(37) Kim, T. W.; Choi, K.-S. Nanoporous BiVO4 Photoanodes with Dual-Layer Oxygen Evolution Catalysts for Solar Water Splitting. *Science* **2014**, *343* (6174), 990–994. https://doi.org/10.1126/science.1246913.

(38) Lee, D.; Kvit, A.; Choi, K.-S. Enabling Solar Water Oxidation by $BiVO_4$ Photoanodes in Basic Media. *Chem. Mater.* **2018**, *30* (14), 4704–4712. https://doi.org/10.1021/acs.chemmater.8b01405.

(39) Kim, T. W.; Choi, K.-S. Improving Stability and Photoelectrochemical Performance of BiVO4 Photoanodes in Basic Media by Adding a ZnFe2O4 Layer. *J. Phys. Chem. Lett.* **2016**, *7* (3), 447–451. https://doi.org/10.1021/acs.jpclett.5b02774.

(40) Kafizas, A.; Xing, X.; Selim, S.; Mesa, C. A.; Ma, Y.; Burgess, C.; McLachlan, M. A.; Durrant, J. R. Ultra-Thin Al2O3 Coatings on BiVO4 Photoanodes: Impact on Performance and Charge Carrier Dynamics. *Catalysis Today* **2019**, *321–322*, 59–66. https://doi.org/10.1016/j.cattod.2017.11.014.

(41) Kishore Pilli, S.; G. Deutsch, T.; E. Furtak, T.; D. Brown, L.; A. Turner, J.; M. Herring, A. BiVO 4 /CuWO 4 Heterojunction Photoanodes for Efficient Solar Driven Water Oxidation. *Physical Chemistry Chemical Physics* **2013**, *15* (9), 3273–3278. https://doi.org/10.1039/C2CP44577H.

(42) Byun, S.; Kim, B.; Jeon, S.; Shin, B. Effects of a SnO 2 Hole Blocking Layer in a BiVO 4 -Based Photoanode on Photoelectrocatalytic Water Oxidation. *Journal of Materials Chemistry A* **2017**, *5* (15), 6905–6913. https://doi.org/10.1039/C7TA00806F.

(43) Liang, Y.; Tsubota, T.; Mooij, L. P. A.; van de Krol, R. Highly Improved Quantum Efficiencies for Thin Film BiVO4 Photoanodes. *J. Phys. Chem. C* **2011**, *115* (35), 17594–17598. https://doi.org/10.1021/jp203004v.

(44) Rao, P. M.; Cai, L.; Liu, C.; Cho, I. S.; Lee, C. H.; Weisse, J. M.; Yang, P.; Zheng, X. Simultaneously Efficient Light Absorption and Charge Separation in WO3/BiVO4 Core/Shell Nanowire Photoanode for Photoelectrochemical Water Oxidation. *Nano Lett.* **2014**, *14* (2), 1099–1105. https://doi.org/10.1021/nl500022z.

(45) Zhang, L.; Reisner, E.; J. Baumberg, J. Al-Doped ZnO Inverse Opal Networks as Efficient Electron Collectors in BiVO 4 Photoanodes for Solar Water Oxidation. *Energy & Environmental Science* **2014**, *7* (4), 1402–1408. https://doi.org/10.1039/C3EE44031A.

(46) Arai, T.; Konishi, Y.; Iwasaki, Y.; Sugihara, H.; Sayama, K. High-Throughput Screening Using Porous Photoelectrode for the Development of Visible-Light-Responsive Semiconductors. *J. Comb. Chem.* **2007**, *9* (4), 574–581. https://doi.org/10.1021/cc0700142.

(47) Patil, R.; Kelkar, S.; Naphade, R.; Ogale, S. Low Temperature Grown $CuBi_2O_4$ with Flower Morphology and Its Composite with CuO Nanosheets for Photoelectrochemical Water Splitting. *J. Mater. Chem. A* **2014**, *2* (10), 3661–3668. https://doi.org/10.1039/C3TA14906D.

(48) Hahn, N. T.; Holmberg, V. C.; Korgel, B. A.; Mullins, C. B. Electrochemical Synthesis and Characterization of P-$CuBi_2O_4$ Thin Film Photocathodes. *J. Phys. Chem. C* **2012**, *116* (10), 6459–6466. https://doi.org/10.1021/jp210130v.

(49) Sharma, G.; Zhao, Z.; Sarker, P.; Nail, B. A.; Wang, J.; Huda, M. N.; Osterloh, F. E. Electronic Structure, Photovoltage, and Photocatalytic Hydrogen Evolution with p-$CuBi_2O_4$ Nanocrystals. *J. Mater. Chem. A* **2016**, *4* (8), 2936–2942. https://doi.org/10.1039/C5TA07040F.

(50) Nakabayashi, Y.; Nishikawa, M.; Nosaka, Y. Fabrication of CuBi2O4 Photocathode through Novel Anodic Electrodeposition for Solar Hydrogen Production. *Electrochimica Acta* **2014**, *125*, 191–198. https://doi.org/10.1016/j.electacta.2014.01.088.

(51) Park, H. S.; Lee, C.-Y.; Reisner, E. Photoelectrochemical Reduction of Aqueous Protons with a CuO|$CuBi_2O_4$ Heterojunction under Visible Light Irradiation. *Phys. Chem. Chem. Phys.* **2014**, *16* (41), 22462–22465. https://doi.org/10.1039/C4CP03883E.

(52) Ong, E. W.; Kwei, G. H.; Robinson, R. A.; Ramakrishna, B. L.; Von Dreele, R. B. Long-Range Antiferromagnetic Ordering in Bi 2 CuO 4. *Phys. Rev. B* **1990**, *42* (7), 4255–4262. https://doi.org/10.1103/PhysRevB.42.4255.

(53) Sharma, G.; Zhao, Z.; Sarker, P.; Nail, B. A.; Wang, J.; Huda, M. N.; Osterloh, F. E. Electronic Structure, Photovoltage, and Photocatalytic Hydrogen Evolution with p-CuBi $_2$ O $_4$ Nanocrystals. *J. Mater. Chem. A* **2016**, *4* (8), 2936–2942. https://doi.org/10.1039/C5TA07040F.

(54) Oropeza, F. E.; Dzade, N. Y.; Pons-Martí, A.; Yang, Z.; Zhang, K. H. L.; de Leeuw, N. H.; Hensen, E. J. M.; Hofmann, J. P. Electronic Structure and Interface Energetics of CuBi $_2$ O $_4$ Photoelectrodes. *J. Phys. Chem. C* **2020**, *124* (41), 22416–22425. https://doi.org/10.1021/acs.jpcc.0c08455.

(55) Cooper, J. K.; Zhang, Z.; Roychoudhury, S.; Jiang, C.-M.; Gul, S.; Liu, Y.-S.; Dhall, R.; Ceballos, A.; Yano, J.; Prendergast, D.; Reyes-Lillo, S. E. CuBi $_2$ O $_4$: Electronic Structure, Optical Properties, and Photoelectrochemical Performance Limitations of the Photocathode. *Chem. Mater.* **2021**, *33* (3), 934–945. https://doi.org/10.1021/acs.chemmater.0c03930.

(56) Kang, D.; Hill, J. C.; Park, Y.; Choi, K.-S. Photoelectrochemical Properties and Photostabilities of High Surface Area CuBi $_2$ O $_4$ and Ag-Doped CuBi $_2$ O $_4$ Photocathodes. *Chem. Mater.* **2016**, *28* (12), 4331–4340. https://doi.org/10.1021/acs.chemmater.6b01294.

(57) Wang, F.; Septina, W.; Chemseddine, A.; Abdi, F. F.; Friedrich, D.; Bogdanoff, P.; van de Krol, R.; Tilley, S. D.; Berglund, S. P. Gradient Self-Doped CuBi $_2$ O $_4$ with Highly Improved Charge Separation Efficiency. *J. Am. Chem. Soc.* **2017**, *139* (42), 15094–15103. https://doi.org/10.1021/jacs.7b07847.

(58) Gopannagari, M.; Reddy, D. A.; Hong, D. H.; Joshi Reddy, K. A.; Kumar, D. P.; Ahn, H. S.; Kim, T. K. Augmented Photoelectrochemical Water Reduction: Influence of Copper Vacancies and Hole-Transport Layer on CuBi $_2$ O $_4$ Photocathode. *J. Mater. Chem. A* **2022**, 10.1039.D1TA09956F. https://doi.org/10.1039/D1TA09956F.

(59) Qu, L.; Tan, R.; Sivanantham, A.; Kang, M. J.; Jeong, Y. J.; Seo, D. H.; Kim, S.; Cho, I. S. Point-Defect Engineering of Nanoporous CuBi2O4 Photocathode via

Rapid Thermal Processing for Enhanced Photoelectrochemical Activity. *Journal of Energy Chemistry* **2022**, 9.

(60) Mary, A. S.; Murugan, C.; Pandikumar, A. Uplifting the Charge Carrier Separation and Migration in Co-Doped CuBi2O4/TiO2 p-n Heterojunction Photocathode for Enhanced Photoelectrocatalytic Water Splitting. *Journal of Colloid and Interface Science* **2022**, *608*, 2482–2492. https://doi.org/10.1016/j.jcis.2021.10.172.

(61) Yuan, X.; Liu, Y.; Yuan, H.; Liu, B.; Guo, T.; Zhou, H.; Li, X. An Electrospun Porous CuBi2O4 Nanofiber Photocathode for Efficient Solar Water Splitting. *Polymers* **2021**, *13* (19), 3341. https://doi.org/10.3390/polym13193341.

(62) Varunkumar, K.; Sellappan, R. Photoelectrochemical Behaviour of CuBi2O4@MoS2 Photocathode for Solar Water Splitting. *Materials Chemistry and Physics* **2021**, *261*, 124245. https://doi.org/10.1016/j.matchemphys.2021.124245.

(63) Song, A.; Levine, I.; Krol, R. van de; Dittrich, T.; Berglund, S. P. Revealing the Relationship between Photoelectrochemical Performance and Interface Hole Trapping in CuBi2O4 Heterojunction Photoelectrodes. *Chem. Sci.* **2020**, *11* (41), 11195–11204. https://doi.org/10.1039/D0SC03030A.

(64) Song, A.; Plate, P.; Chemseddine, A.; Wang, F.; F. Abdi, F.; Wollgarten, M.; Krol, R. van de; P. Berglund, S. Cu:NiO as a Hole-Selective Back Contact to Improve the Photoelectrochemical Performance of CuBi 2 O 4 Thin Film Photocathodes. *Journal of Materials Chemistry A* **2019**, *7* (15), 9183–9194. https://doi.org/10.1039/C9TA01489F.

(65) Corby, S.; Rao, R. R.; Steier, L.; Durrant, J. R. The Kinetics of Metal Oxide Photoanodes from Charge Generation to Catalysis. *Nat Rev Mater* **2021**. https://doi.org/10.1038/s41578-021-00343-7.

(66) Emin, D. Optical Properties of Large and Small Polarons and Bipolarons. *Phys. Rev. B* **1993**, *48* (18), 13691–13702. https://doi.org/10.1103/PhysRevB.48.13691.

(67) Ziwritsch, M.; Müller, S.; Hempel, H.; Unold, T.; Abdi, F. F.; van de Krol, R.; Friedrich, D.; Eichberger, R. Direct Time-Resolved Observation of Carrier Trapping and Polaron Conductivity in BiVO4. *ACS Energy Lett.* **2016**, *1* (5), 888–894. https://doi.org/10.1021/acsenergylett.6b00423.

(68) Tang, J.; Cowan, A. J.; Durrant, J. R.; Klug, D. R. Mechanism of O2 Production from Water Splitting: Nature of Charge Carriers in Nitrogen Doped Nanocrystalline TiO2 Films and Factors Limiting O2 Production. *J. Phys. Chem. C* **2011**, *115* (7), 3143–3150. https://doi.org/10.1021/jp1080093.

(69) Liu, R.; Zheng, Z.; Spurgeon, J.; Yang, X. Enhanced Photoelectrochemical Water-Splitting Performance of Semiconductors by Surface Passivation Layers. *Energy Environ. Sci.* **2014**, *7* (8), 2504–2517. https://doi.org/10.1039/C4EE00450G.

(70) Zandi, O.; Hamann, T. W. Enhanced Water Splitting Efficiency Through Selective Surface State Removal. *J. Phys. Chem. Lett.* **2014**, *5* (9), 1522–1526. https://doi.org/10.1021/jz500535a.

(71) Tang, J.; Durrant, J. R.; Klug, D. R. Mechanism of Photocatalytic Water Splitting in TiO2. Reaction of Water with Photoholes, Importance of Charge Carrier Dynamics, and Evidence for Four-Hole Chemistry. *J. Am. Chem. Soc.* **2008**, *130* (42), 13885–13891. https://doi.org/10.1021/ja8034637.

(72) Therese, G. H. A.; Kamath, P. V. Electrochemical Synthesis of Metal Oxides and Hydroxides. *Chem. Mater.* **2000**, *12* (5), 1195–1204. https://doi.org/10.1021/cm990447a.

(73) Choi, K.-S.; Jang, H. S.; McShane, C. M.; Read, C. G.; Seabold, J. A. Electrochemical Synthesis of Inorganic Polycrystalline Electrodes with Controlled Architectures. *MRS Bull.* **2010**, *35* (10), 753–760. https://doi.org/10.1557/mrs2010.504.

(74) Kang, D.; Kim, T. W.; Kubota, S. R.; Cardiel, A. C.; Cha, H. G.; Choi, K.-S. Electrochemical Synthesis of Photoelectrodes and Catalysts for Use in Solar Water Splitting. *Chem. Rev.* **2015**, *115* (23), 12839–12887. https://doi.org/10.1021/acs.chemrev.5b00498.

(75) Barzgar Vishlaghi, M.; Kahraman, A.; Kaya, S. Increasing Charge Separation Property and Water Oxidation Activity of $BiVO_4$ Photoanodes via a Postsynthetic Treatment. *J. Phys. Chem. C* **2020**, *124* (2), 1337–1345. https://doi.org/10.1021/acs.jpcc.9b08099.

(76) Johnson, R. W.; Hultqvist, A.; Bent, S. F. A Brief Review of Atomic Layer Deposition: From Fundamentals to Applications. *Materials Today* **2014**, *17* (5), 236–246. https://doi.org/10.1016/j.mattod.2014.04.026.

(77) Ponraj, J. S.; Attolini, G.; Bosi, M. Review on Atomic Layer Deposition and Applications of Oxide Thin Films. *Critical Reviews in Solid State and Materials Sciences* **2013**, *38* (3), 203–233. https://doi.org/10.1080/10408436.2012.736886.

(78) Bard, A. J.; Faulkner, L. R. *Electrochemical Methods: Fundamentals and Applications*, 2nd ed.; Wiley: New York, 2001.

(79) Le Formal et al. - 2012 - The Transient Photocurrent and Photovoltage Behavi.Pdf.

(80) Bredar, A. R. C.; Chown, A. L.; Burton, A. R.; Farnum, B. H. Electrochemical Impedance Spectroscopy of Metal Oxide Electrodes for Energy Applications. *ACS Appl. Energy Mater.* **2020**, *3* (1), 66–98. https://doi.org/10.1021/acsaem.9b01965.

(81) Chen, Z.; Dinh, H.; Miller, E. *Photoelectrochemical Water Splitting: Standards, Experimental Methods, and Protocols*; SpringerBriefs in Energy; Springer-Verlag: New York, 2013. https://doi.org/10.1007/978-1-4614-8298-7.

(82) Connor, P.; Schuch, J.; Kaiser, B.; Jaegermann, W. The Determination of Electrochemical Active Surface Area and Specific Capacity Revisited for the System MnO_x as an Oxygen Evolution Catalyst. *Zeitschrift für Physikalische Chemie* **2020**, *234* (5), 979–994. https://doi.org/10.1515/zpch-2019-1514.

(83) Ewen Smith, Geoffrey Dent - Modern Raman Spectroscopy_ A Practical Approach-Wiley (2005).Pdf.

(84) Ameh, E. S. A Review of Basic Crystallography and X-Ray Diffraction Applications. *Int J Adv Manuf Technol* **2019**, *105* (7–8), 3289–3302. https://doi.org/10.1007/s00170-019-04508-1.

(85) Stenzel, O. *The Physics of Thin Film Optical Spectra: An Introduction*; Springer series in surface sciences; Springer: Berlin ; New York, 2005.

(86) Goldstein, J. I.; Newbury, D. E.; Michael, J. R.; Ritchie, N. W. M.; Scott, J. H. J.; Joy, D. C. *Scanning Electron Microscopy and X-Ray Microanalysis*; Springer New York: New York, NY, 2018. https://doi.org/10.1007/978-1-4939-6676-9.

(87) Abdi, F. F.; Savenije, T. J.; May, M. M.; Dam, B.; van de Krol, R. The Origin of Slow Carrier Transport in $BiVO_4$ Thin Film Photoanodes: A Time-Resolved

Microwave Conductivity Study. *J. Phys. Chem. Lett.* **2013**, *4* (16), 2752–2757. https://doi.org/10.1021/jz4013257.

(88) Selim, S.; Francàs, L.; García-Tecedor, M.; Corby, S.; Blackman, C.; Gimenez, S.; Durrant, J. R.; Kafizas, A. WO_3/$BiVO_4$: Impact of Charge Separation at the Timescale of Water Oxidation. *Chem. Sci.* **2019**, *10* (9), 2643–2652. https://doi.org/10.1039/C8SC04679D.

(89) George, K.; Khachatrjan, T.; van Berkel, M.; Sinha, V.; Bieberle-Hütter, A. Understanding the Impact of Different Types of Surface States on Photoelectrochemical Water Oxidation: A Microkinetic Modeling Approach. *ACS Catal.* **2020**, *10* (24), 14649–14660. https://doi.org/10.1021/acscatal.0c03987.

(90) Zhong, D. K.; Choi, S.; Gamelin, D. R. Near-Complete Suppression of Surface Recombination in Solar Photoelectrolysis by "Co-Pi" Catalyst-Modified W:$BiVO_4$. *J. Am. Chem. Soc.* **2011**, *133* (45), 18370–18377. https://doi.org/10.1021/ja207348x.

(91) Liang, Y.; Messinger, J. Improving BiVO4 Photoanodes for Solar Water Splitting through Surface Passivation. *Phys. Chem. Chem. Phys.* **2014**, *16* (24), 12014. https://doi.org/10.1039/c4cp00674g.

(92) Liu, R.; Zheng, Z.; Spurgeon, J.; Yang, X. Enhanced Photoelectrochemical Water-Splitting Performance of Semiconductors by Surface Passivation Layers. *Energy Environ. Sci.* **2014**, *7* (8), 2504–2517. https://doi.org/10.1039/C4EE00450G.

(93) Zachäus, C.; Abdi, F. F.; Peter, L. M.; van de Krol, R. Photocurrent of $BiVO_4$ Is Limited by Surface Recombination, Not Surface Catalysis. *Chem. Sci.* **2017**, *8* (5), 3712–3719. https://doi.org/10.1039/C7SC00363C.

(94) Feng, F.; Li, C.; Jian, J.; Qiao, X.; Wang, H.; Jia, L. Boosting Hematite Photoelectrochemical Water Splitting by Decoration of TiO2 at the Grain Boundaries. *Chemical Engineering Journal* **2019**, *368*, 959–967. https://doi.org/10.1016/j.cej.2019.03.005.

(95) Ahmed, M. G.; Kretschmer, I. E.; Kandiel, T. A.; Ahmed, A. Y.; Rashwan, F. A.; Bahnemann, D. W. A Facile Surface Passivation of Hematite Photoanodes with TiO_2 Overlayers for Efficient Solar Water Splitting. *ACS Appl. Mater. Interfaces* **2015**, *7* (43), 24053–24062. https://doi.org/10.1021/acsami.5b07065.

(96) Kim, M.-W.; Kim, K.; Ohm, T. Y.; Yoon, H.; Joshi, B.; Samuel, E.; Swihart, M. T.; Choi, S. K.; Park, H.; Yoon, S. S. Electrosprayed BiVO4 Nanopillars Coated with Atomic-Layer-Deposited ZnO/TiO2 as Highly Efficient Photoanodes for Solar Water Splitting. *Chemical Engineering Journal* **2018**, *333*, 721–729. https://doi.org/10.1016/j.cej.2017.09.130.

(97) McDowell, M. T.; Lichterman, M. F.; Spurgeon, J. M.; Hu, S.; Sharp, I. D.; Brunschwig, B. S.; Lewis, N. S. Improved Stability of Polycrystalline Bismuth Vanadate Photoanodes by Use of Dual-Layer Thin TiO_2 /Ni Coatings. *J. Phys. Chem. C* **2014**, *118* (34), 19618–19624. https://doi.org/10.1021/jp506133y.

(98) Hwang, S. W.; Kim, J. U.; Baek, J. H.; Kalanur, S. S.; Jung, H. S.; Seo, H.; Cho, I. S. Solution-Processed TiO2/BiVO4/SnO2 Triple-Layer Photoanode with Enhanced Photoelectrochemical Performance. *Journal of Alloys and Compounds* **2019**, *785*, 1245–1252. https://doi.org/10.1016/j.jallcom.2019.01.251.

(99) Tian, Z.; Zhang, P.; Qin, P.; Sun, D.; Zhang, S.; Guo, X.; Zhao, W.; Zhao, D.; Huang, F. Novel Black BiVO4/TiO2−x Photoanode with Enhanced Photon Absorption and Charge Separation for Efficient and Stable Solar Water Splitting. *Advanced Energy Materials* **2019**, *9* (27), 1901287. https://doi.org/10.1002/aenm.201901287.

(100) Singh, A. P.; Kodan, N.; Mehta, B. R.; Held, A.; Mayrhofer, L.; Moseler, M. Band Edge Engineering in $BiVO_4$ /TiO_2 Heterostructure: Enhanced Photoelectrochemical Performance through Improved Charge Transfer. *ACS Catal.* **2016**, *6* (8), 5311–5318. https://doi.org/10.1021/acscatal.6b00956.

(101) Monfort, O.; Raptis, D.; Satrapinskyy, L.; Roch, T.; Plesch, G.; Lianos, P. Production of Hydrogen by Water Splitting in a Photoelectrochemical Cell Using a BiVO4/TiO2 Layered Photoanode. *Electrochimica Acta* **2017**, *251*, 244–249. https://doi.org/10.1016/j.electacta.2017.08.125.

(102) Eisenberg, D.; Ahn, H. S.; Bard, A. J. Enhanced Photoelectrochemical Water Oxidation on Bismuth Vanadate by Electrodeposition of Amorphous Titanium Dioxide. *J. Am. Chem. Soc.* **2014**, *136* (40), 14011–14014. https://doi.org/10.1021/ja5082475.

(103) Chen, H.; Li, J.; Yang, W.; Balaghi, S. E.; Triana, C. A.; Mavrokefalos, C. K.; Patzke, G. R. The Role of Surface States on Reduced TiO_2 @$BiVO_4$ Photoanodes:

Enhanced Water Oxidation Performance through Improved Charge Transfer. *ACS Catal.* **2021**, *11* (13), 7637–7646. https://doi.org/10.1021/acscatal.1c00686.

(104) Yoon, J.-H.; Jung, S.-C.; Kim, J.-S. Photocatalytic Effects for the TiO2-Coated Phosphor Materials. *Materials Chemistry and Physics* **2011**, *125* (3), 342–346. https://doi.org/10.1016/j.matchemphys.2010.11.004.

(105) Lee, S. Y.; Jeon, C.; Kim, S. H.; Kim, Y.; Jung, W.; An, K.-S.; Park, C.-Y. *In-Situ* X-Ray Photoemission Spectroscopy Study of Atomic Layer Deposition of TiO$_{2}$ on Silicon Substrate. *Jpn. J. Appl. Phys.* **2012**, *51*, 031102. https://doi.org/10.1143/JJAP.51.031102.

(106) King, D. M.; Liang, X.; Zhou, Y.; Carney, C. S.; Hakim, L. F.; Li, P.; Weimer, A. W. Atomic Layer Deposition of TiO2 Films on Particles in a Fluidized Bed Reactor. *Powder Technology* **2008**, *183* (3), 356–363. https://doi.org/10.1016/j.powtec.2008.01.025.

(107) Frost, R. L.; Henry, D. A.; Weier, M. L.; Martens, W. Raman Spectroscopy of Three Polymorphs of BiVO4: Clinobisvanite, Dreyerite and Pucherite, with Comparisons to (VO4)3-Bearing Minerals: Namibite, Pottsite and Schumacherite. *Journal of Raman Spectroscopy* **2006**, *37* (7), 722–732. https://doi.org/10.1002/jrs.1499.

(108) Zhang, W.; Ma, J.; Xiong, L.; Jiang, H.-Y.; Tang, J. Well-Crystallized α-FeOOH Cocatalysts Modified $BiVO_4$ Photoanodes for Efficient and Stable Photoelectrochemical Water Splitting. *ACS Appl. Energy Mater.* **2020**, *3* (6), 5927–5936. https://doi.org/10.1021/acsaem.0c00834.

(109) Wang, S.; He, T.; Yun, J.-H.; Hu, Y.; Xiao, M.; Du, A.; Wang, L. New Iron-Cobalt Oxide Catalysts Promoting BiVO4 Films for Photoelectrochemical Water Splitting. *Advanced Functional Materials* **2018**, *28* (34), 1802685. https://doi.org/10.1002/adfm.201802685.

(110) Cheng, W.-H.; Richter, M. H.; May, M. M.; Ohlmann, J.; Lackner, D.; Dimroth, F.; Hannappel, T.; Atwater, H. A.; Lewerenz, H.-J. Monolithic Photoelectrochemical Device for Direct Water Splitting with 19% Efficiency. *ACS Energy Lett.* **2018**, *3* (8), 1795–1800. https://doi.org/10.1021/acsenergylett.8b00920.

(111) Luo, H.; Mueller, A. H.; McCleskey, T. M.; Burrell, A. K.; Bauer, E.; Jia, Q. X. Structural and Photoelectrochemical Properties of $BiVO_4$ Thin Films. *J. Phys. Chem. C* **2008**, *112* (15), 6099–6102. https://doi.org/10.1021/jp7113187.

(112) Lamers, M.; Li, W.; Favaro, M.; Starr, D. E.; Friedrich, D.; Lardhi, S.; Cavallo, L.; Harb, M.; van de Krol, R.; Wong, L. H.; Abdi, F. F. Enhanced Carrier Transport and Bandgap Reduction in Sulfur-Modified $BiVO_4$ Photoanodes. *Chem. Mater.* **2018**, *30* (23), 8630–8638. https://doi.org/10.1021/acs.chemmater.8b03859.

(113) Sanchez, C.; Sieber, K. D.; Somorjai, G. A. The Photoelectrochemistry of Niobium Doped α-Fe2O3. *Journal of Electroanalytical Chemistry and Interfacial Electrochemistry* **1988**, *252* (2), 269–290. https://doi.org/10.1016/0022-0728(88)80216-X.

(114) Kahraman, A.; Vishlaghi, M. B.; Baylam, I.; Ogasawara, H.; Sennaroğlu, A.; Kaya, S. The Fast-Track Water Oxidation Channel on $BiVO_4$ Opened by Nitrogen Treatment. *J. Phys. Chem. Lett.* **2020**, *11* (20), 8758–8764. https://doi.org/10.1021/acs.jpclett.0c02190.

(115) Trześniewski, B. J.; Smith, W. A. Photocharged $BiVO_4$ Photoanodes for Improved Solar Water Splitting. *J. Mater. Chem. A* **2016**, *4* (8), 2919–2926. https://doi.org/10.1039/C5TA04716A.

(116) Le Formal, F.; Sivula, K.; Grätzel, M. The Transient Photocurrent and Photovoltage Behavior of a Hematite Photoanode under Working Conditions and the Influence of Surface Treatments. *J. Phys. Chem. C* **2012**, *116* (51), 26707–26720. https://doi.org/10.1021/jp308591k.

(117) Seabold, J. A.; Zhu, K.; Neale, N. R. Efficient Solar Photoelectrolysis by Nanoporous Mo:$BiVO_4$ through Controlled Electron Transport. *Phys. Chem. Chem. Phys.* **2014**, *16* (3), 1121–1131. https://doi.org/10.1039/C3CP54356K.

(118) Liang, Y.; Tsubota, T.; Mooij, L. P. A.; van de Krol, R. Highly Improved Quantum Efficiencies for Thin Film BiVO4 Photoanodes. *J. Phys. Chem. C* **2011**, *115* (35), 17594–17598. https://doi.org/10.1021/jp203004v.

(119) Meekins, B. H.; Kamat, P. V. Got TiO_2 Nanotubes? Lithium Ion Intercalation Can Boost Their Photoelectrochemical Performance. *ACS Nano* **2009**, *3* (11), 3437–3446. https://doi.org/10.1021/nn900897r.

(120) Shi, Q.; Murcia-López, S.; Tang, P.; Flox, C.; Morante, J. R.; Bian, Z.; Wang, H.; Andreu, T. Role of Tungsten Doping on the Surface States in BiVO $_4$ Photoanodes for Water Oxidation: Tuning the Electron Trapping Process. *ACS Catal.* **2018**, *8* (4), 3331–3342. https://doi.org/10.1021/acscatal.7b04277.

(121) Lewis, N. S. A Quantitative Investigation of the Open-Circuit Photovoltage at the Semiconductor/Liquid Interface. *J. Electrochem. Soc.* **1984**, *131* (11), 2496. https://doi.org/10.1149/1.2115347.

(122) Du, C.; Zhang, M.; Jang, J.-W.; Liu, Y.; Liu, G.-Y.; Wang, D. Observation and Alteration of Surface States of Hematite Photoelectrodes. *J. Phys. Chem. C* **2014**, *118* (30), 17054–17059. https://doi.org/10.1021/jp5006346.

(123) Kuang, Y.; Yamada, T.; Domen, K. Surface and Interface Engineering for Photoelectrochemical Water Oxidation. *Joule* **2017**, *1* (2), 290–305. https://doi.org/10.1016/j.joule.2017.08.004.

(124) *Photoelectrochemical Water Splitting - Standards, Experimental Methods, and Protocols | Zhebo Chen | Springer*. https://www.springer.com/gp/book/9781461482970 (accessed 2021-08-12).

(125) Park, Y.; Kang, D.; Choi, K.-S. Marked Enhancement in Electron–Hole Separation Achieved in the Low Bias Region Using Electrochemically Prepared Mo-Doped BiVO 4 Photoanodes. *Physical Chemistry Chemical Physics* **2014**, *16* (3), 1238–1246. https://doi.org/10.1039/C3CP53649A.

(126) Parmar, K. P. S.; Kang, H. J.; Bist, A.; Dua, P.; Jang, J. S.; Lee, J. S. Photocatalytic and Photoelectrochemical Water Oxidation over Metal-Doped Monoclinic BiVO4 Photoanodes. *ChemSusChem* **2012**, *5* (10), 1926–1934. https://doi.org/10.1002/cssc.201200254.

(127) Hankin, A.; E. Bedoya-Lora, F.; C. Alexander, J.; Regoutz, A.; H. Kelsall, G. Flat Band Potential Determination: Avoiding the Pitfalls. *Journal of Materials Chemistry A* **2019**, *7* (45), 26162–26176. https://doi.org/10.1039/C9TA09569A.

(128) Elaborately Modified BiVO4 Photoanodes for Solar Water Splitting[8583].Pdf.

(129) Lumley, M. A.; Radmilovic, A.; Jang, Y. J.; Lindberg, A. E.; Choi, K.-S. Perspectives on the Development of Oxide-Based Photocathodes for Solar Fuel

Production. *J. Am. Chem. Soc.* **2019**, *141* (46), 18358–18369. https://doi.org/10.1021/jacs.9b07976.

(130) Gerischer, H. ON THE STABILITY OF SEMICONDUCTOR ELECTRODES AGAINST PHOTODECOMPOSITION. 11.

(131) Chen, S.; Wang, L.-W. Thermodynamic Oxidation and Reduction Potentials of Photocatalytic Semiconductors in Aqueous Solution. *Chem. Mater.* **2012**, *24* (18), 3659–3666. https://doi.org/10.1021/cm302533s.

(132) Lamers, M.; Sahre, M.; Müller, M. J.; Abou-Ras, D.; van de Krol, R.; Abdi, F. F. Influence of Post-Deposition Annealing on the Photoelectrochemical Performance of $CuBi_2O_4$ Thin Films. *APL Materials* **2020**, *8* (6), 061101. https://doi.org/10.1063/5.0003005.

(133) Oropeza, F. E.; Feleki, B. T.; Zhang, K. H. L.; Hensen, E. J. M.; Hofmann, J. P. Influence of Reduced Cu Surface States on the Photoelectrochemical Properties of CuBi2O4. *ACS Appl. Energy Mater.* **2019**, *2* (9), 6866–6874. https://doi.org/10.1021/acsaem.9b01333.

(134) Zhang, Z.; Zhu, B.; Guan, X. Operational Spectroelectrochemical Investigation on the Interfacial Charge Dynamics of Copper Bismuth Oxide Based Photocathode. *J. Phys. Chem. Lett.* **2022**, 2356–2364. https://doi.org/10.1021/acs.jpclett.2c00140.

(135) Biesinger, M. C.; Lau, L. W. M.; Gerson, A. R.; Smart, R. St. C. Resolving Surface Chemical States in XPS Analysis of First Row Transition Metals, Oxides and Hydroxides: Sc, Ti, V, Cu and Zn. *Applied Surface Science* **2010**, *257* (3), 887–898. https://doi.org/10.1016/j.apsusc.2010.07.086.

(136) Wang, F.; Yang, H.; Zhang, H.; Jiang, J. Growth Process and Enhanced Photocatalytic Performance of CuBi2O4 Hierarchical Microcuboids Decorated with AuAg Alloy Nanoparticles. *J Mater Sci: Mater Electron* **2018**, *29* (2), 1304–1316. https://doi.org/10.1007/s10854-017-8036-6.

(137) Shaaban, E.; Li, G. Probing Active Sites for Carbon Oxides Hydrogenation on Cu/TiO2 Using Infrared Spectroscopy. *Commun Chem* **2022**, *5* (1), 1–9. https://doi.org/10.1038/s42004-022-00650-2.

(138) Poulston, S.; Parlett, P. M.; Stone, P.; Bowker, M. Surface Oxidation and Reduction of CuO and Cu2O Studied Using XPS and XAES. *Surface and Interface Analysis*

1996, *24* (12), 811–820. https://doi.org/10.1002/(SICI)1096-9918(199611)24:12<811::AID-SIA191>3.0.CO;2-Z.

(139) Zhang, F. X.; Saxena, S. K. Raman Studies of Bi2CuO4 at High Pressures. *Appl. Phys. Lett.* **2006**, *88* (14), 141926. https://doi.org/10.1063/1.2189450.

(140) Djaballah, A. M.; Bagtache, R.; Tartaya, S.; Trari, M. Synthesis and Characterization of the Semiconductor CuBi2O4 for Optical and Dielectric Studies. Application to Methyl Violet Degradation under Visible Light. *Reac Kinet Mech Cat* **2021**, *134* (2), 1055–1067. https://doi.org/10.1007/s11144-021-02115-4.

(141) Patil, R.; Kelkar, S.; Naphade, R.; Ogale, S. Low Temperature Grown CuBi2O4 with Flower Morphology and Its Composite with CuO Nanosheets for Photoelectrochemical Water Splitting. *J. Mater. Chem. A* **2014**, *2* (10), 3661–3668. https://doi.org/10.1039/C3TA14906D.

(142) Xu, C.; Chen, Y.; Xie, X.; Yan, K.; Si, Y.; Zhang, M.; Yan, Q. Construction of Ag SPR-Promoted Z-scheme Ag2MoO4/CuBi2O4 Composites with Enhanced Photocatalytic Performance. *J Mater Sci: Mater Electron* **2020**, *31* (11), 8151–8164. https://doi.org/10.1007/s10854-020-03271-4.

(143) Bera, S.; Lee, S. A.; Lee, W.-J.; Kim, J.-H.; Kim, C.; Kim, H. G.; Khan, H.; Jana, S.; Jang, H. W.; Kwon, S.-H. Hierarchical Nanoporous BiVO4 Photoanodes with High Charge Separation and Transport Efficiency for Water Oxidation. *ACS Appl. Mater. Interfaces* **2021**, *13* (12), 14291–14301. https://doi.org/10.1021/acsami.1c00958.

(144) Gao, Y.; Hamann, T. W. Elucidation of CuWO4 Surface States During Photoelectrochemical Water Oxidation. *J. Phys. Chem. Lett.* **2017**, *8* (12), 2700–2704. https://doi.org/10.1021/acs.jpclett.7b00664.

(145) Klahr, B.; Gimenez, S.; Fabregat-Santiago, F.; Bisquert, J.; Hamann, T. W. Photoelectrochemical and Impedance Spectroscopic Investigation of Water Oxidation with "Co–Pi"-Coated Hematite Electrodes. *J. Am. Chem. Soc.* **2012**, *134* (40), 16693–16700. https://doi.org/10.1021/ja306427f.

(146) McNeill, C. R.; Hwang, I.; Greenham, N. C. Photocurrent Transients in All-Polymer Solar Cells: Trapping and Detrapping Effects. *Journal of Applied Physics* **2009**, *106* (2), 024507. https://doi.org/10.1063/1.3177337.

(147) Klahr, B.; Gimenez, S.; Fabregat-Santiago, F.; Hamann, T.; Bisquert, J. Water Oxidation at Hematite Photoelectrodes: The Role of Surface States. *J. Am. Chem. Soc.* **2012**, *134* (9), 4294–4302. https://doi.org/10.1021/ja210755h.

(148) Usman, E.; Barzgar Vishlaghi, M.; Kahraman, A.; Solati, N.; Kaya, S. Modifying the Electron-Trapping Process at the $BiVO_4$ Surface States via the TiO_2 Overlayer for Enhanced Water Oxidation. *ACS Appl. Mater. Interfaces* **2021**, acsami.1c16847. https://doi.org/10.1021/acsami.1c16847.

(149) Choi, J.; Song, J. T.; Jang, H. S.; Choi, M.-J.; Sim, D. M.; Yim, S.; Lim, H.; Jung, Y. S.; Oh, J. Interfacial Band-Edge Engineered TiO2 Protection Layer on Cu2O Photocathodes for Efficient Water Reduction Reaction. *Electron. Mater. Lett.* **2017**, *13* (1), 57–65. https://doi.org/10.1007/s13391-017-6316-1.

(150) Zheng, J.; Lyu, Y.; Wang, R.; Xie, C.; Zhou, H.; Jiang, S. P.; Wang, S. Crystalline TiO2 Protective Layer with Graded Oxygen Defects for Efficient and Stable Silicon-Based Photocathode. *Nat Commun* **2018**, *9* (1), 3572. https://doi.org/10.1038/s41467-018-05580-z.

(151) Zhang, Q.; Zhai, B.; Lin, Z.; Zhao, X.; Diao, P. Dendritic CuBi2O4 Array Photocathode Coated with Conformal TiO2 Protection Layer for Efficient and Stable Photoelectrochemical Hydrogen Evolution Reaction. *J. Phys. Chem. C* **2021**, *125* (3), 1890–1901. https://doi.org/10.1021/acs.jpcc.0c10421.

(152) *Reference Air Mass 1.5 Spectra*. https://www.nrel.gov/grid/solar-resource/spectra-am1.5.html (accessed 2022-05-29).

(153) Hashimoto, S.; Tanaka, A. Alteration of Ti 2p XPS Spectrum for Titanium Oxide by Low-Energy Ar Ion Bombardment. *Surface and Interface Analysis* **2002**, *34* (1), 262–265. https://doi.org/10.1002/sia.1296.

(154) Godfroid, T.; Gouttebaron, R.; Dauchot, J. P.; Leclère, P.; Lazzaroni, R.; Hecq, M. Growth of Ultrathin Ti Films Deposited on SnO2 by Magnetron Sputtering. *Thin Solid Films* **2003**, *437* (1), 57–62. https://doi.org/10.1016/S0040-6090(03)00605-9.

(155) Haber, J. A.; Lewis, N. S. Infrared and X-Ray Photoelectron Spectroscopic Studies of the Reactions of Hydrogen-Terminated Crystalline Si(111) and Si(100) Surfaces with Br_2, I_2, and Ferrocenium in Alcohol Solvents. *J. Phys. Chem. B* **2002**, *106* (14), 3639–3656. https://doi.org/10.1021/jp0102872.

(156) Shi, X.; Cai, L.; Ma, M.; Zheng, X.; Park, J. H. General Characterization Methods for Photoelectrochemical Cells for Solar Water Splitting. *ChemSusChem* **2015**, *8* (19), 3192–3203. https://doi.org/10.1002/cssc.201500075.

(157) Bredar, A. R. C.; Chown, A. L.; Burton, A. R.; Farnum, B. H. Electrochemical Impedance Spectroscopy of Metal Oxide Electrodes for Energy Applications. *ACS Appl. Energy Mater.* **2020**, *3* (1), 66–98. https://doi.org/10.1021/acsaem.9b01965.

(158) Hirschorn, B.; Orazem, M. E.; Tribollet, B.; Vivier, V.; Frateur, I.; Musiani, M. Determination of Effective Capacitance and Film Thickness from Constant-Phase-Element Parameters. *Electrochimica Acta* **2010**, *55* (21), 6218–6227. https://doi.org/10.1016/j.electacta.2009.10.065.

Chapter 7. Appendix

7.1.Appendix A: Supporting Information for $BiVO_4$

Calculation of j_{abs} for $BiVO_4$

First, the solar spectrum of 1.5AM G was taken from the literature[152]. The light harvesting efficiency was calculated from the formula given below:

$$LHE = 1 - 10^{-A(\lambda)} \qquad \text{Equation A1.1}$$

Then, the solar spectra ($W.m^{-2}.nm^{-1}$) was multiplied by the calculated LHE, at energies higher than the band gap of $BiVO_4$, which is 2.55 eV. The result was converted to number of photons, and the resulting number was converted to current density, assuming that all of the absorbed photons are resulted in electron-hole pairs. The jabs for $BiVO_4$ was calculated as 4.41 $mA.cm^{-2}$.

XPS analysis

As shown in Figure A1.1, Bi 4f and V 2p XPS signal intensities drop, as the Ti 2p signal intensities increase with the increasing thickness of the TiO_2 overlayer.

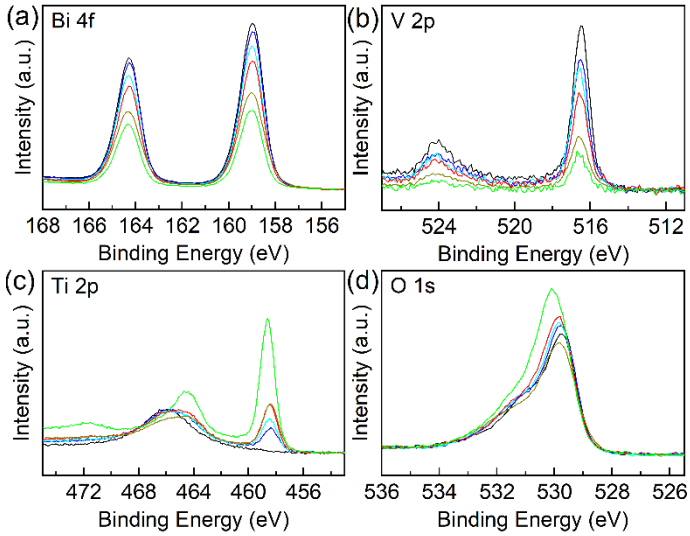

Figure A1.1. (a) Bi 4f, (b) V 2p, (c) Ti 2p, and (d) O 1s XPS spectra of $BiVO_4$ with increasing TiO_2 layer thickness.

Ti 2p peaks were deconvoluted to account for the Bi $4d_{3/2}$ signal. The fittings are presented in Figure A1.2. Shirley type of background was utilized, and the Gaussian-

Lorentzian function was used to fit the peaks. The Ti $2p_{1/2}$ and Ti $2p_{3/2}$ peaks are located at 464.2 eV and 458.5 eV, respectively. The peak positions suggest that Ti^{4+} phase for the overlayer according to prior XPS studies on TiO_2[135,153,154].

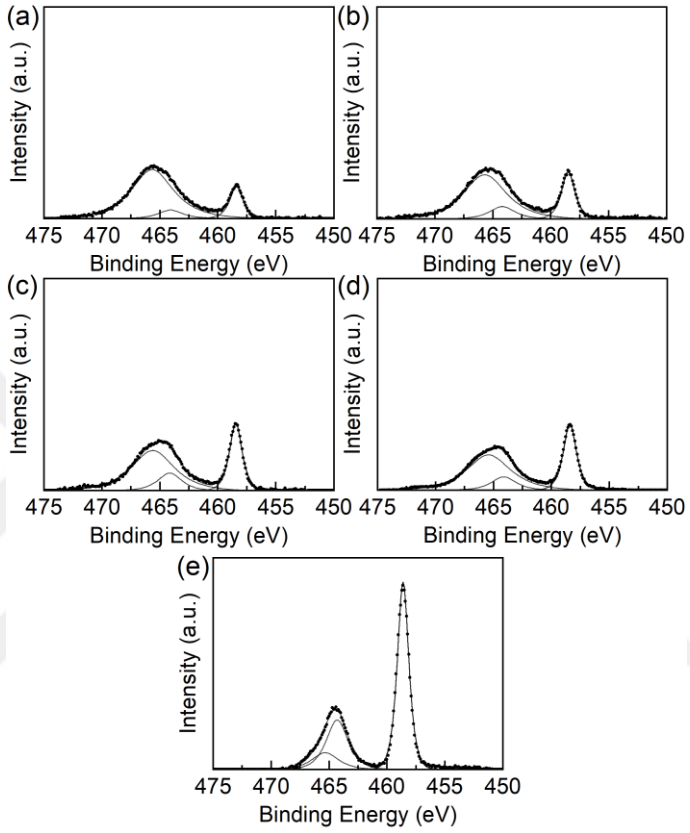

Figure A1.2. Deconvoluted Ti 2p XPS spectra for (a) $BiVO_4$/0.6 nm TiO_2, (b) $BiVO_4$/0.9 nm TiO_2, (c) $BiVO_4$/1.3 nm TiO_2, (d) $BiVO_4$/1.4 nm TiO_2, and (e) $BiVO_4$/5.8 nm TiO_2.

For the quantification of the TiO_2 overlayer thickness, which was assumed uniform over $BiVO_4$, the photoelectron mean free path was calculated using Equation S1 given below[8]:

$$\lambda = 0.096 \times \sqrt{E} \qquad \text{Equation A1.2}$$

where E is the kinetic energy (in eV), λ is the mean free path (in nm) of the photoelectron.

The overlayer thickness was calculated using Equation S2[155]:

$$d = \lambda \times \ln[\frac{I_{overlayer}}{I_{substrate}} \times \frac{SF_{substrate}}{SF_{overlayer}} \times \frac{\rho_{substrate}}{\rho_{overlayer}} + 1] \qquad \text{Equation A1.3}$$

where d is the calculated thickness, $I_{overlayer}$ and $I_{substrate}$ are the elemental peak intensities of the overlayer and the substrate, respectively. SF refers to the elemental sensitivity factors and ρ is the density of the atoms.

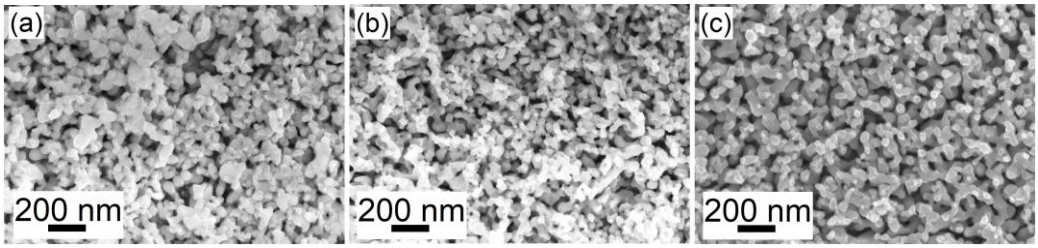

Figure A1.3. FESEM images of (a) bare $BiVO_4$, (b) $BiVO_4$/1.3 nm TiO_2, and (c) $BiVO_4$/5.8 nm TiO_2.

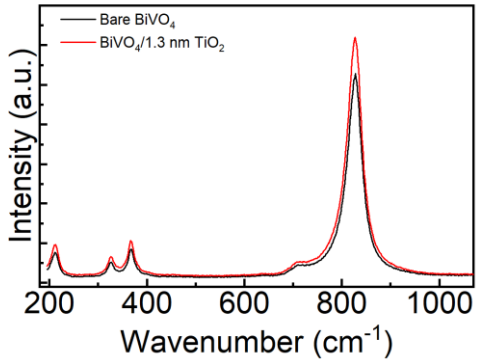

Figure A1.4. Raman spectra for bare $BiVO_4$ and $BiVO_4$/1.3 nm TiO_2.

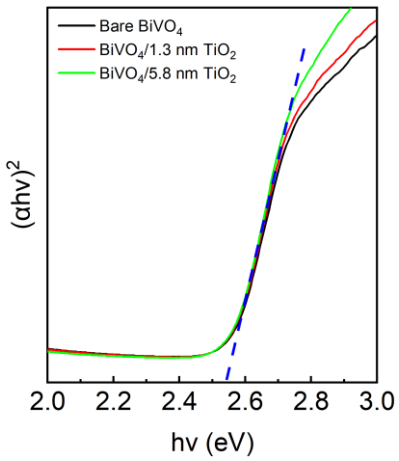

Figure A1.5. Tauc plots for bare $BiVO_4$, $BiVO_4$/1.3 nm TiO_2, and $BiVO_4$/5.8 nm TiO_2.

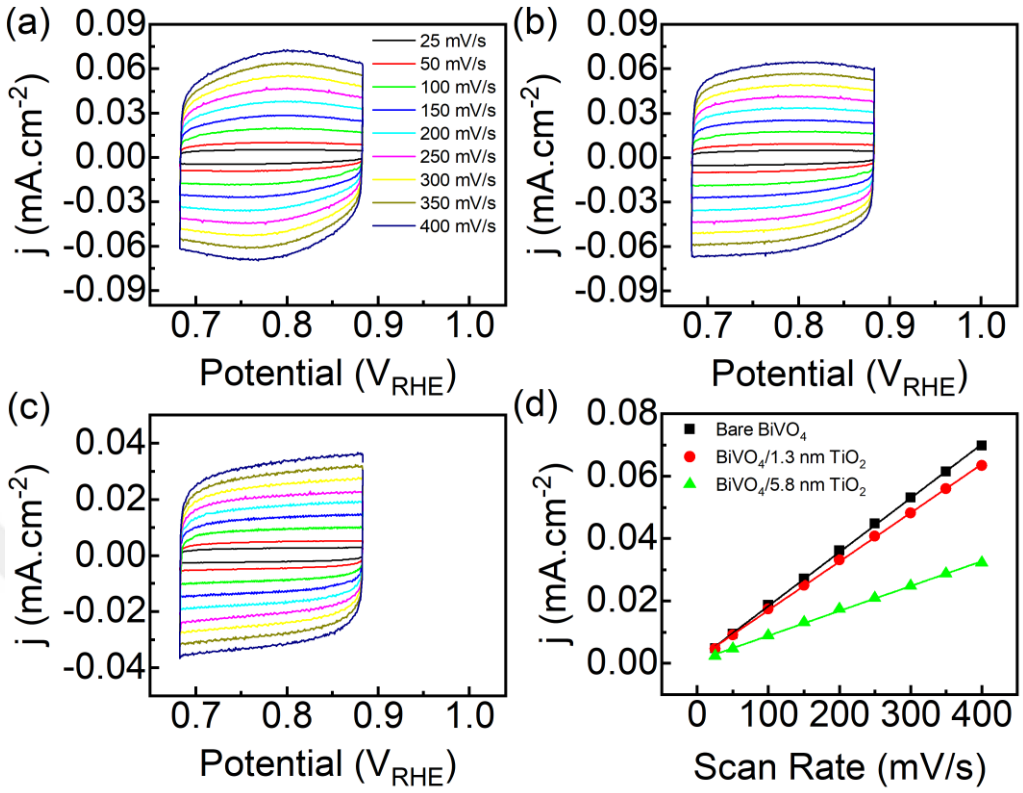

Figure A1.6. Electrochemically active surface area (ECSA) calculation done via CV measurement in dark at various scan rates for (a) bare $BiVO_4$, (b) $BiVO_4$/1.3 nm TiO_2, and (c) $BiVO_4$/5.8 nm TiO_2. (d) Measured capacitive current density with respect to the scan rate for the photoanodes.

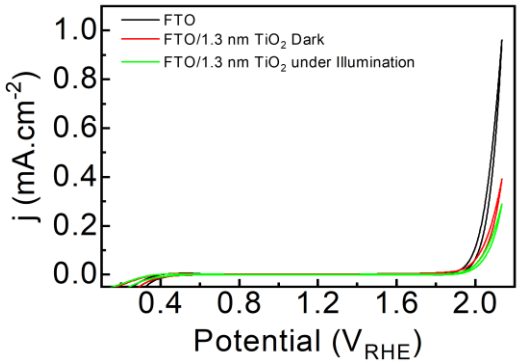

Figure A1.7. CV measurement of bare FTO, FTO/1.3 nm TiO_2 in dark and under illumination in 0.1 M KPi buffer with pH=7.4.

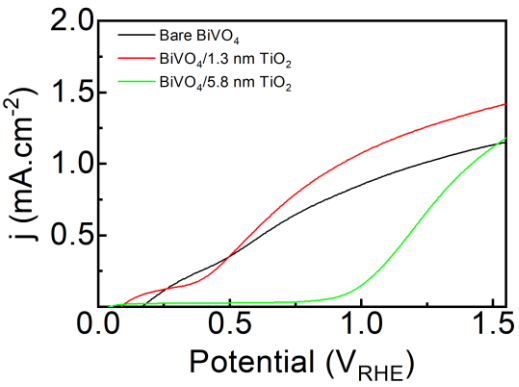

Figure A1.8. LSV measurements under back illumination in 0.1 M KPi buffer with pH=7.4.

As shown in Figure S8, when the light is turned on we observe an anodic spike, corresponding to hole accumulation at the space-charge region[113]. The anodic spike is larger for $BiVO_4$/1.3 nm TiO_2 which is in accordance with the TPC measurements presented in the main text, is attributed to enhanced charge separation. However, at higher thickness, the steady-state photocurrent drops, which is in agreement with the LSV and the EIS results.

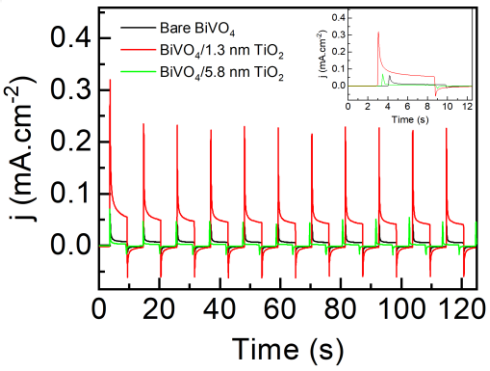

Figure A1.9. TPC measurements at 0.6 V_{RHE} under AM1.5G illumination in 0.1 M KPi buffer with pH=7.4.

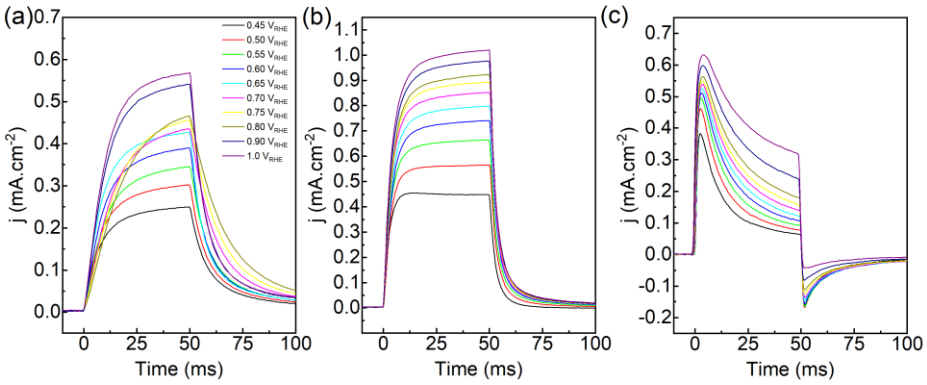

Figure A1.10. Transient Photocurrent (TPC) measurements done with 50.0 ms white light LED pulse in 0.1 M KPi buffer with 0.5 M Na_2SO_3 solution for (a) bare $BiVO_4$, (b) $BiVO_4$/1.3 nm TiO_2, and (c) $BiVO_4$/5.8 nm TiO_2

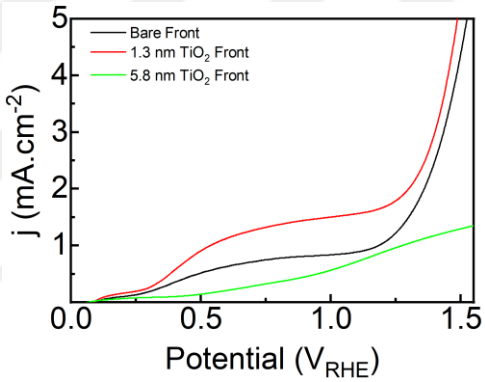

Figure A1.11. LSV measurement under front illumination in 0.1 M KPi buffer with 0.5 M Na_2SO_3 with pH=7.8.

For the charge injection efficiency (η_{inj}) and charge separation efficiency (η_{sep}) calculations, the formulas given below were used[156]:

$$\eta_{sep} = \frac{j_{sca}}{j_{abs}} \qquad \text{Equation A1.3}$$

$$\eta_{inj} = \frac{j_{buff}}{j_{sca}} \qquad \text{Equation A1.4}$$

where j_{sca} is the photocurrent density in scavenger solution, where η_{inj} is 100%, j_{abs} is the photon absorption rate in the units of current density, and j_{buff} is the photocurrent density in buffer solution. j_{abs} was calculated as 4.4 mA.cm^{-2}, where the details of the calculation can be found elsewhere[37].

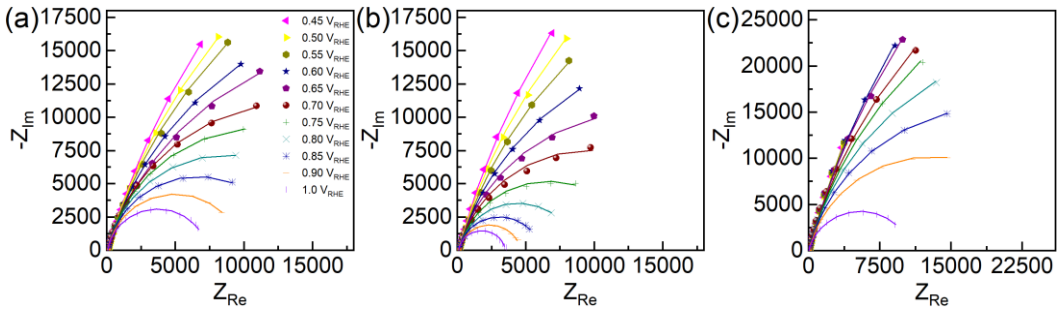

Figure A1.12. Fittings for the Nyquist plots in 0.1 M KPi buffer pH=7.4 under illumination between 0.45-1.0 V_{RHE} for (a) bare $BiVO_4$, (b) $BiVO_4$/1.3 nm TiO_2, and (c) $BiVO_4$/5.8 nm TiO_2.

The Nyquist plot fittings were done using Randle's model with a constant phase element (CPE) as shown in Figure 1b inset. CPE is commonly used instead of capacitors for the metal oxide electrodes to model the capacitive behavior at the interface since the surface of the electrode contains heterogeneities resulting from roughness, the porosity of the electrode surface, and the complexity of the double-layer structure[157]. The capacitance (C) associated with the CPE is given by equation S3[158]:

$$C = Q^{\frac{1}{\alpha}} \times R^{\frac{1}{\alpha}-1} \qquad \text{Equation A1.5}$$

where C is the capacitance, Q is the constant phase element, R is the resistance, and α is an empirical factor between 0 and 1.

Long-term activities of the photoanodes were also tested by performing consecutive LSV scans under chopped light illumination. Both bare $BiVO_4$ and $BiVO_4$/1.3 nm TiO_2 maintained their activities and 1.3 nm TiO_2 layer outperforms the activity of bare $BiVO_4$.

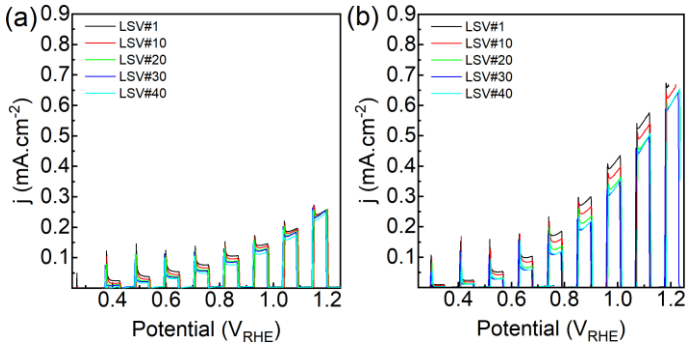

Figure A1.13. 40 consecutive LSV scans performed by using (a) bare $BiVO_4$ and (b) $BiVO_4$/1.3 nm TiO_2. The measurements were performed in 0.1 M KPi buffer with pH=7.4 under chopped-light illumination.

7.2.Appendix B: Supporting information for $CuBi_2O_4$

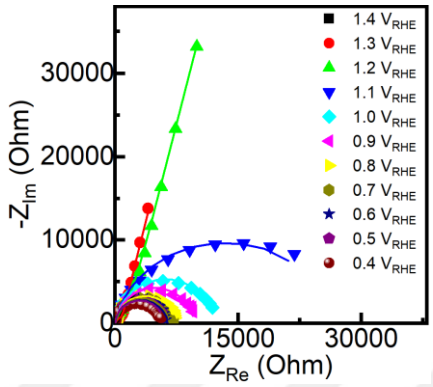

Figure B1.1. Fittings for the Nyquist plots for measured in O_2-purged 0.1 M NaOH under front illumination between 1.4 V_{RHE}-0.4 V_{RHE}.

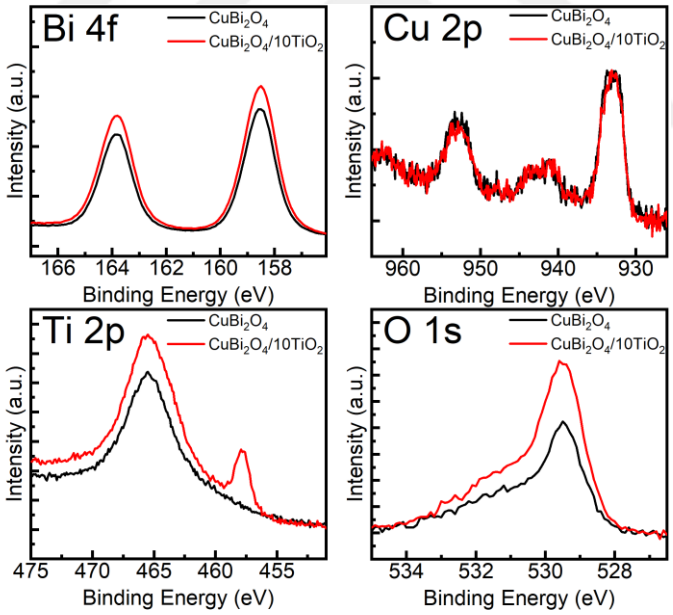

Figure B1.2. (a) Bi 4f, (b) Cu 2p, (c) Ti 2p, and (d) O 1s XPS spectra for $CuBi_2O_4$ and $CuBi_2O_4/10TiO_2$.